To my lovely parents, Ali & Hassina.

You are the light that brightens my way.

Acknowledgement

The work reported in this thesis was done under the roof of the UMR 6614 – CORIA lab of the University of Rouen. I hereby thank the director of the lab, Pr. Armelle Cessou, for hosting me through the duration of my PhD.

This thesis was financed by the Normandy region. Therefore, I express my gratitude for being given this life changing opportunity.

I would like to thank Dr. Vincent COUDERC, Pr. Serge BIELAWSKI. Dr. Bertrand KIBLER and Dr. Emmanuel HUGONNOT for accepting to review my work as well as for their pertinent remarks.

I would like to thank my supervisors, Dr. Thomas Godin, Pr. Ammar Hideur and Pr. Claude Rozé for giving me the honor of being a part of their team. In addition, I would like to thank them for their trust, guidance, support and patience during my three years of PhD.

Moreover, I would like to thank Pr. Denis Lebrun, the director of the doctoral school ED-PSIME, for his fruitful contributions to the accomplished work.

I would like to thank Dr. Rezki Becheker and Dr. Said Idlahcen for being my mentors in the experiment room. It was a pleasure doing experiments with them.

I would like to thank my colleagues in the laser team and in the Coria lab in general, especially Dr. Mohamed Talbi and Dr. Anas Ayoub. You were my second family during my PhD.

I would like to thank all my primary, middle and high school teachers in my home-town Ain Abessa. My teachers at the institute of electrical and electronics engineering in Boumerdes as well as my teachers in LETI- Saint Petersburg. Each of them has contributed to the forming of my personality and to my thirst for knowledge.

Finally, I would like to thank my family from brothers and sisters to uncles, aunts and friends for their presence in my life, for their love and support. Your prayers are the fuel that keeps pushing me forward.

Contents

List of Figures

CHAPTER 1

Introduction

FOR CENTURIES, humanity never stopped the quest towards the understanding of the surrounding physical world, starting from the tiniest particles and moving up in scale to planets and galaxies with an oriented attention to their natures, behaviors and interactions. Such incredible efforts resulted in the creation of an evolving fundamental knowledge and led to great technological advances that positively affect every aspect of the human life. Among the many remarkable technological developments achieved in physics in the last century, light-based technologies stand out as they play an essential role in our daily life, and not only through the vital process of photosynthesis. The study of light has for instance brought high-speed internet, numerous life-saving advances in medical sciences, and shaped our understanding of matter as well as of the universe. For centuries, photonics has then influenced society through both fundamental and applied sciences and it is then not surprising that around 40 Nobel Prizes have been awarded to light-related topics [1] and that the United Nations have declared 2015 the International Year of Light [2] and the 16^{th} of May the International Day of Light [3].

From Ibn Al-Haytham's pionneering *Book of Optics* [4] in the 11^{th} century to Einstein's work in the 20^{th} century and to nowadays optics, photonics has then fueled the emergence of technologies with great societal impacts. Among them, the discovery of the laser more than 60 years ago is the most striking one as it enabled many breakthroughs in myriad scientific areas, and this manuscript would not be sufficient to list them all. In particular, the laser is a powerful tool for a wide range of measurement and diagnostics techniques, including imaging and spectroscopy. In the field of metrology in general, tremendous efforts have thereby been dedicated to push back the resolution limits of laser-based techniques both in the spatial and temporal domains in order to access previously unreachable phenomena. Beyond such applications, the light sources themselves focus the attention of the scientific community for decades due to their intriguing

dynamics. Photonics-based research is then a constantly evolving field which is extremely active both from the fundamental physics as well as from the applied sciences point of view, and pushing the above-mentioned spatial and temporal limits even further is still needed for understanding many complex phenomena.

This PhD thesis actually perfectly fits in this frame as it concerns both fundamental and applied researches and deals both with the specific dynamics of pulsed light sources and the development of new diagnostic tools with record-high resolutions for ultrafast science. This is due to the particular context in which it took place, at the CORIA laboratory [5] within the Optics and Lasers department. Indeed, the CORIA's research activities are, on the one hand, oriented towards real-life applications in the fields of fluid mechanics or reactive flows but, in the other hand, fueled by fundamental innovations in optical metrology such as fiber laser sources or original imaging techniques. Specifically, this PhD thesis has been supported by several research projects (regional platform RENADIAG, regional projects RIN TOFU and SPIDER, and national ANR project RIFT) at the boundary between real-world applications and basic research and has then multiple objectives at different levels. The primary goal of the present work is the development of innovative tools for capturing the ultrafast dynamics of the processes encountered in laser ablation or two-phase flows. The second goal is the development of efficient sources for the spectroscopy of reactive flows in a specific spectral range in the near infrared. In parallel of this two "applied" objectives, a strong attention is also given to the underlying ultrafast dynamics occurring in the systems concerned, as the control of such transient phenomena is today a major concern in laser physics. As a consequence, this PhD thesis then spans several interrelated areas of photonics within the Optics and Lasers department as it bring together the fields of fiber laser, nonlinear optics, ultrafast imaging and even holography. This manuscript is then organized as follows.

The **first chapter** aims at introducing the bases in linear and nonlinear optics that will be necessary to understand the studies presented in the following chapters. A special attention will be given to the effect of four-wave mixing, which is the cornerstone of the fiber optical parametric oscillators (FOPO) developed in this thesis and that are now widespread wavelength-agile sources. The nonlinear Shrödinger equation, that governs pulse propagation in optical fibers, will also be detailed as it is used to validate various experimental cases throughout the manuscript.

The **second chapter** is devoted to the design, simulation and experimental implementation of a new concept of parametric oscillator allowing to generate high-energy, tunable, and synchronized picosecond pulses in a specific wavelength range. This source, termed fiber optical parametric chirped-pulse oscillator (FOPCPO), is based on combination of standard FOPO based on degenerate four wave mixing with the principle of chirped-pulse amplification. This chapter then reports the working principle and the performances accessible to the system we developed, but also explore the energy scaling possibilities of such a concept through numerical simulations, with the ambition to use it for coherent Raman spectrocopy in reactive flows at the CORIA.

The **third chapter** is focused on the specific dynamics of FOPOs rather than on the energy scaling. Specifically, we use the dispersive Fourier transform (DFT) technique to track the energy transfers between the parametric waves through their shot-to-shot spectra. We then show that particular statistical tools, such as mutual information analysis, are actually extremely relevant to exploit large ensemble of date acquired via DFT and enable the full understanding of the FOPO's dynamic behavior. As wavelength correlations have not been explored within FOPOs to date, we eventually highlight the parameters allowing to shape them in those systems, as such a feature could prove relevant in the frame of several quantum optics applications.

The **fourth chapter** is dedicated to the development of a versatile ultrafast imaging technique with the aim of bringing such methods out of a fully-controlled laboratory environment, such as in the CORIA laboratory. Ultrafast imaging, and more precisely single-shot imaging, motivates for more than a decade now the intensive researches of many research group around the world, with an actual race for the highest frame rates and largest sequence depths. Strikingly, frame rates as high as hundreds of trillion-frames-per-second are now accessible to the best techniques, and a comprehensive summary of the most relevant techniques is presented in this chapter. However, such techniques still suffer from a lack a flexibility or from complex reconstruction schemes. The main objective of this chapter is then to demonstrate an original and user-friendly technique combining an active imaging method known as sequentially timed all-optical mapping photography (STAMP) with an amplitude and phase shaper based on acousto-optics interactions. This work also takes advantage of the presence of experts in holography within the CORIA's Optics and Lasers Department to simplify even further our novel imaging system using digital in-line holography. Its virtues and limitations as well as the potential improvements that can be foreseen as prospects of this PhD thesis are eventually critically discussed.

CHAPTER 2

Theoretical background

In this first Chapter, we introduce the main physical concepts and optical phenomena that will be used throughout the experimental work reported in this thesis. Understanding the linear and nonlinear mechanisms involved in laser pulse propagation in optical fibers is indeed fundamental for the comprehension of Chapter 2 and 3, mainly dealing with fiber oscillators, but also of Chapter 4, in which the notions of amplitude and phase shaping of ultrashort pulses are extensively used. Therefore, we first briefly recall the basics of optical fibers, their guiding mechanisms as well as their different types depending on the geometrical structure, refractive index profile and transverse modes. We then introduce the different linear and nonlinear effects influencing the behavior of ultrashort pulses in optical fibers and detail the main equation governing their propagation (nonlinear Schrödinger equation) and used to numerically simulate it. Here, the description of the nonlinear effects is limited to the processes that will be encountered in the following experimental realizations. A reader willing to have an extensive description of all the processes affecting pulse propagation can opt for the reading of the reference textbooks on this subject (e.g. [6,7]).

2.1 Optical fibers

Optical fibers are a vital cornerstone in the field of telecommunications due to their capacity of transmitting over large distances with high bit rates. They also play a major technological role in several fields. Optical fibers have proven to be essential in sensing with, for instance, temperature, pressure or strain measurements, among many other physical parameters [8]. They are also the key element of various technologies such fiber endoscopes or fiber optics gyroscopes.

When doped with rare-earth materials (mainly Erbium, Ytterbium or Thulium) optical fibers can be used as gain media for laser oscillators or amplifiers [9, 10]. In contrast with conventional solid-state lasers, the ability of an optical fiber to guide light within its limited-size core allows to maintain high intensities along its length, thereby considerably extending the effective pumping length. This makes fiber lasers compact and relatively low-cost laser sources producing laser beams with high stability and excellent beam quality. Moreover, the exploitation of the strong nonlinearity in optical fibers provides strong grounds for the design and implementation of wavelength-agile laser sources [11] such as supercontinuum sources and optical parametric oscillators and amplifiers (FOPO/FOPA). The latter allow the parametric generation and/or amplification of laser wavelengths which are inaccessible to conventional lasers. Due to their importance for many applications, these sources and their dynamics are of great importance to the laser community and will be further discussed throughout this manuscript.

2.1.1 Standard fibers

In general, a typical optical fiber is a multi-layer silica based flexible thin fiber acting as an optical waveguide. Its waveguiding properties stem from the exploitation of the total internal reflection phenomenon (TIR) in order to confine light. This occurs when a transparent medium is surrounded by another one with a lower refractive index. When the angle of incidence of light is superior to the critical angle, the light beam is totally reflected at the boundary between the two transparent media. The conditions for TIR can be satisfied in many ways and this provides considerable flexibility in the design of optical fibers regarding their geometrical structure, refractive index profile, mode number, polarization as well as the dispersive properties among other parameters. Consequently, several types of optical fibers have been developed, and each one having a specific purpose and affecting the propagation of light pulses in a specific manner.
The most common type is the step-index fiber where the transition of the refractive index at the boundary between the core and cladding is abrupt, as shown in Fig.2.1. However, it is possible for the refractive index to be engineered so that it gradually changes between the core and cladding according to a certain predefined profile for the purpose of mitigating dispersive effects. Such an optical fiber is called graded-index fiber. It should be noted that both the core and cladding of an optical fiber are mostly based on silica and their respective respective refractive indices are slightly altered in order to achieve the refractive index difference needed for TIR. This alteration can be obtained through the addition of a doping material to silica in order to adjust the refractive index. For instance, the core of an optical fiber can be doped with phosphorus or germanium in order

increase it or with boron or fluorine to decrease it [6].

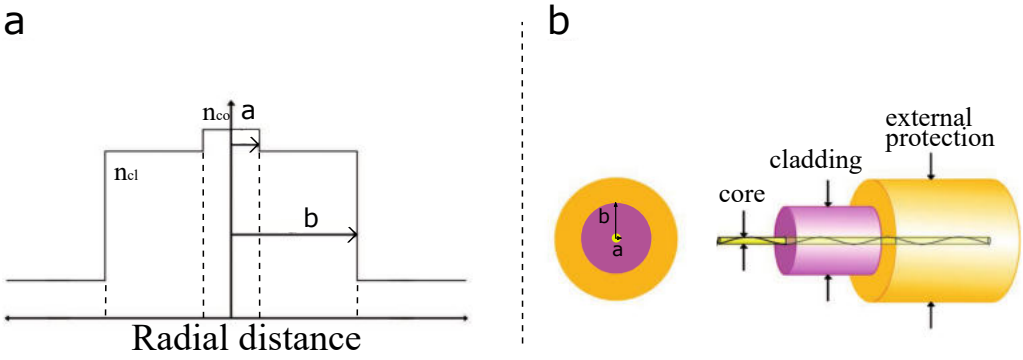

Figure 2.1: **Representation of a cylindrical step index fiber**. a) Refractive index profile. b) Geometrical structure.

In addition to its geometrical structure and refractive index profile, the number of transverse spatial modes that are allowed to propagate within an optical fiber is also a key parameter to control. According to the geometric properties of the fiber, namely the size of its core, one or more transverse modes can be accepted for a given wavelength. A single-mode fiber only allows one fundamental mode to be guided while a multimode fiber will support several modes. The normalized frequency V allows for the determination of whether the propagation is single-mode (V <2.405) or multimode (V >2.405) and is calculated with the following formula:

$$V = \frac{2\pi}{\lambda} a \sqrt{n_{co}^2 - n_{cl}^2} \tag{2.1}$$

where λ is the wavelength, a is the core diameter, n_{co} is the refractive index of the core and n_{cl} is the refractive index of the cladding. Therefore, as the wavelength is decreased, a single-mode fiber turns into multi-mode below a certain cutoff wavelength. This hinders single-mode operation for shorter wavelength without reducing the core diameter a. This limitation rises from the simplistic structure of these optical fibers as their design is rigid with a limited set of parameters to adjust (core diameter and refractive index difference between core and cladding). However, other types of optical fibers, such as photonic crystal fibers (PCF) [12], have been developed and exhibit more flexible designs and unique properties allowing to overcome the limitations of ordinary optical fibers.

2.1.2 Photonic crystal fibers

As it is indicated by its name, a photonic crystal fiber (PCF) mimics the structural properties of photonic crystals in a fiber form. It is basically a set of internal periodic micro-structures that forms an hexagonal lattice on a background material. Typically, pure silica is used as a background material while the micro-structures are air-filled holes with a diameter in the micrometer scale [13, 14], as shown in Fig. 2.2.

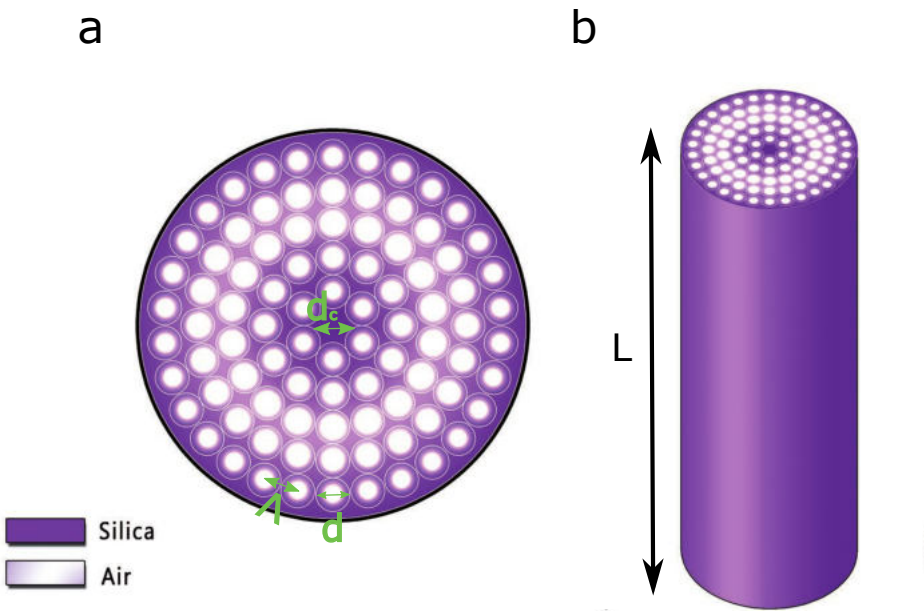

Figure 2.2: **Representation of an air-filled microstructured fiber or PCF.** a) Cross-section view of the PCF where d_c is the core diameter, d is the hole diameter while λ is the pitch. b) 3-D representation of the PCF.

In this type of PCF, light is allowed to propagate within the solid core due to a mechanism similar to TIR called modified total internal reflection (M-TIR). The latter occurs since the lattice structure surrounding the solid silica core provides a lower effective refractive index. This leads to light confinement within the PCF in a manner similar to ordinary optical fibers. However, in the case of PCFs, the effective refractive index provided by the lattice structure is wavelength dependent. Therefore, the proper selection of the PCF's parameters (hole diameter and pitch) can impose a single-mode regime on broad spectral ranges. In fact, the ratio between the hole diameter and hole spacing in the lattice structure determines the refractive index of the photonic cladding in PCFs. If this ratio does not exceed the value of 0.4, the value of the normalized frequency is kept below the threshold for a multi-mode regime for any wavelength as shown in Fig. 2.3. A PCF that possesses this quality is named an endlessly single-mode fiber [15].

In addition to providing a lower refractive index compared to the background material, the periodic structure of the lattice forms a photonic bandgap and has the capacity of blocking the propagation of certain spectral regions [16]. However, if the periodicity of the lattice is broken, it leads to the altering of the lattice optical properties. This can be achieved by defecting the lattice structure either through the removal of one or several holes from the micro-structured arrangement or by having a hole with a different diameter within it. In fact, the defect in the periodic lattice creates a space where light is allowed to propagate and therefore represents the core of the PCF. In this case, the mechanism of light confinement within the PCF is different than the M-TIR as light is guided through a core with a low refractive index due to the photonic bandgap. Fibers that use this mechanism are called photonic bandgap fibers (PBG).

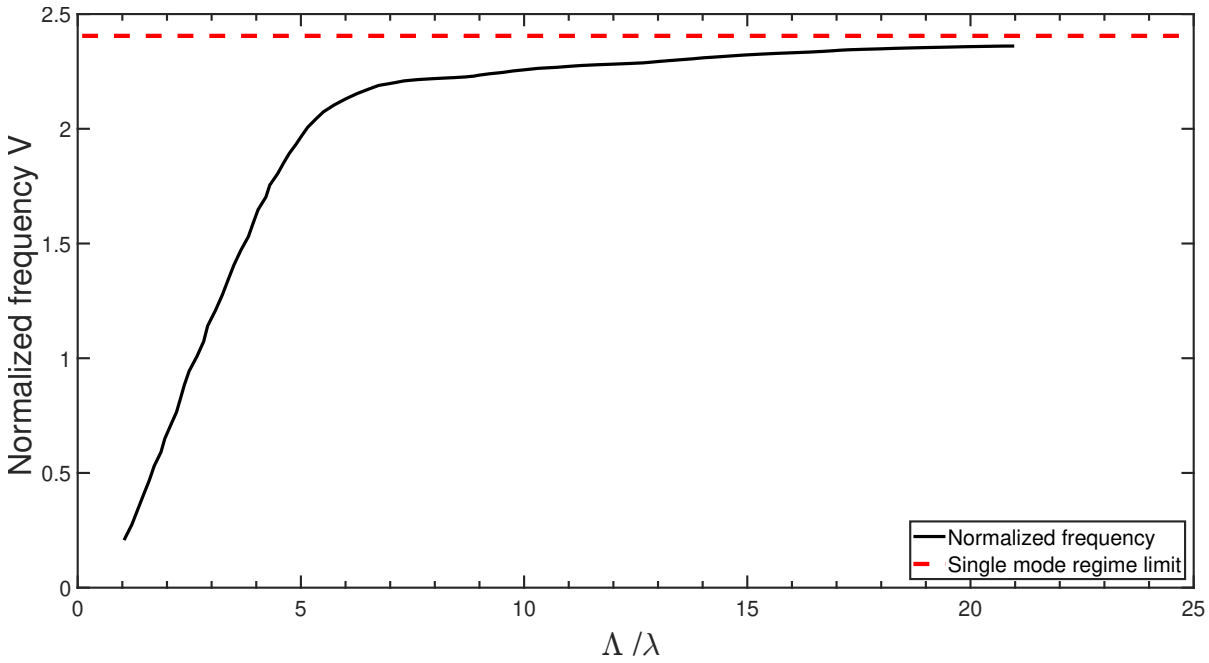

Figure 2.3: **Normalized frequency** for a PCF with a hexagonal lattice and a filling factor of 0.20. single mode propagation is maintained in the PCF along the visible and infrared spectral regions [16].

Although the structure of the PCF presents a high complexity compared to ordinary optical fibers, it provides a more flexible control over its optical properties parameters through the adjustement of the shape and diameter of the holes, the spacing between holes, the lattice type and the refractive indices of the holes and background material. This enables the tailoring of the propagation mode, but more importantly of the dispersion profile and nonlinearity [6,17,18]. PCF have then become a key element in applications requiring enhanced nonlinearities and/or specific dispersion maps: supercontinuum generation [19], telecommunications, fiber lasers and amplifiers, or even quantum optics [20].

2.2 Linear effects in optical fibers

2.2.1 Attenuation

The propagation of a laser pulse through an optical fiber results in the loss of some of its optical power. These losses can either be intrinsic and originate from the fiber material and cannot be avoided, or can be extrinsic and mainly caused by imperfection in the fabrication process [21]. The latter can be avoided by optimizing the fabrication process. One of the causes of the intrinsic losses in silica fibers is the irregular microscopic structure of glass. This structure imposes a fluctuation of density, which results in a variation of the refractive index. The latter causes Rayleigh scattering to occur and light to diffuse in all directions. The intensity of the scattered light due to Rayleigh scattering is wavelength-dependent and makes longer wavelengths less prone to scatter compared

to shorter wavelengths. Another cause of the intrinsic losses in silica is the absorption of light due to electronic transitions and vibrational resonances. As opposed to Rayleigh scattering, these losses are largely significant at longer wavelengths and are referred to as IR absorption. The impact of the Rayleigh scattering and IR absorption can be combined to represent the overall intrinsic losses as:

$$\alpha_{int} = \alpha_R + \alpha_{IR} = R/\lambda^4 + \alpha_{IR} \tag{2.2}$$

Where α_{int} represents the intrinsic losses and is the summation of losses due to Rayleigh scattering α_R and IR absorption α_{ir} with R being the Rayleigh scattering coefficient. In general, Rayleigh scattering dominates the intrinsic losses for wavelengths shorter than 1.5 μm while the infrared absorption becomes dominant above 1.6 μm, leaving the window between 1.5 and 1.6 μm with minimal losses around 0.2 dB/km.

As mentioned previously, the refractive index of silica-based optical fibers can be controlled through the addition of dopants to pure silica. Although the dopant has a minimal effect on the infrared losses, its effect on the Rayleigh scattering is considerable as it can increase the scattering intensity or decrease it through the change of the coefficient R. At 1.55 μm, the losses for pure silica are around 0.115 dB/km while it increases to 0.13 dB/km if silica is doped with GeO_2 and decreases to 0.095 dB/km for P_2O_5-doped silica. Fig. 2.4 compares the intrinsic losses in a silica-based fiber with or without doping.

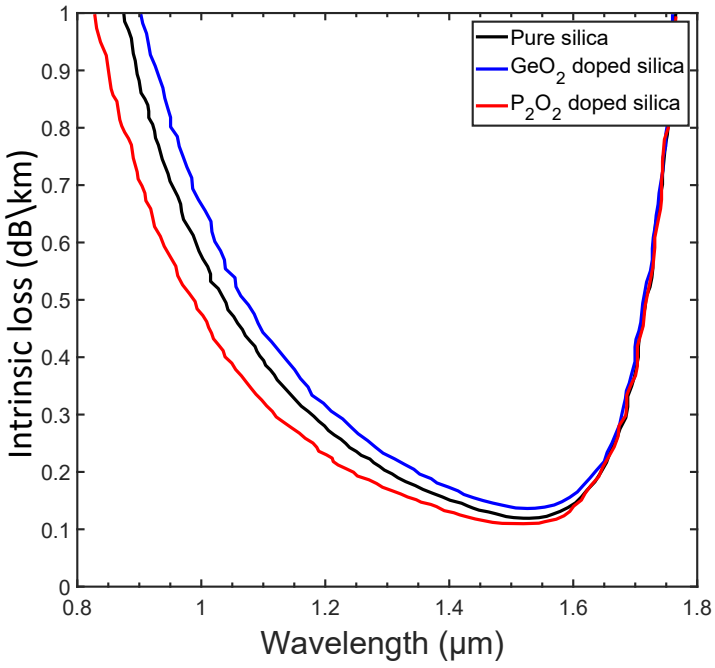

Figure 2.4: **Intrinsic losses** in pure silica (black), GeO_2-doped silica (blue) and P_2O_5-doped silica (red) [22].

As for the extrinsic losses, they are mainly caused by the imperfections in the fabrication process.

The latter can result in a deformed optical fiber with micro-bends and variations in the core diameter. Moreover, the existence of hydroxyl ions in the fiber material results in the creation of loss peaks around 1.4 μm. This wavelength represents an harmonic to the fundamental absorption line of hydroxyl ions at 2.73 μm [23]. As a result, if high purity raw materials are used in the fabrication of optical fibers and if the fabrication process is controlled as well, the extrinsic losses will be significantly minimized to a level where they can be ignored with respect to the intrinsic losses. In practice, the total losses in an optical fiber are expressed using the standard formula:

$$\alpha_{dB} = -\frac{10}{L}\log\left(\frac{P_T}{P_0}\right) = 4.343\alpha_L \tag{2.3}$$

where α_L represents the propagation losses (m^{-1}), α_{dB} the propagation loss in dB, P_T is the pulse power at the end-face of the optical fiber while P_0 is the initial power of the laser pulse.

2.2.2 Dispersion

When a laser pulse propagates through a given medium, its spectral components may travel with slightly different velocities due to the dependency of the refractive index on the wavelength [6,7]. In this case, the refractive index n is represented as:

$$n = n(\lambda) = c/v(\lambda) \tag{2.4}$$

The dependency of the refractive index on the wavelength is mainly related to the material properties of the dielectric medium. This dependency originates from the fact that the response of the medium to the interaction of its bond electrons with an electromagnetic wave is frequency-dependent. The real part of the frequency-dependent response can relate to an integral of its corresponding imaginary part and vice-versa according to the Krammer-Kronig relations. Physically, the real part of the response corresponds to the refractive index while the imaginary part relates to the gain or absorption coefficient. According to the principle of causality, the wavelength dependency of the refractive index is the result of absorption. In fact, if a laser pulse propagates in a dielectric medium, it experiences absorption when its carrier frequency matches one of the resonance frequencies of the medium. Far from these frequencies, the refractive index becomes frequency dependent and can be approximated by the Sellmeier equation [6]:

$$n^2(\omega) = 1 + \sum_{j=1}^{m} \frac{B_j\omega_j^2}{\omega_j^2 - \omega^2} \tag{2.5}$$

where B_j represents the absorption line strength while ω_j defines its frequency. An example of the frequency-dependent refractive index in fused silica is shown in Fig.2.5a along with the group refractive index n_g (ratio of the vacuum velocity of light to the group velocity, see below). For a laser pulse with a central frequency ω_0, the refractive index relates to the propagation constant β

according to the following expression:

$$\beta(\omega) = n(\omega)\frac{\omega}{c} \tag{2.6}$$

The expansion of the frequency-dependent propagation constant $\beta(w)$ around the central frequency w_0 using Taylor series allows for the separation of the terms responsible for the different dispersive effects that the laser pulse experiences as it propagates [6]:

$$\beta(\omega) = \sum_{m=0}^{\infty} \frac{1}{m!}\frac{d^m\beta}{d\omega^m}(\omega - \omega_0)^m \tag{2.7}$$

$$\beta(\omega) = n(\omega)\frac{\omega}{c} = \beta_0 + \beta_1(\omega - \omega_0) + \frac{1}{2}\beta_2(\omega - \omega_0)^2 + \dots \tag{2.8}$$

Each of the orders of the propagation constant has its unique impact on light propagation. The first order β_1 represents the inverse of the group velocity vg, the velocity at which the envelope of the propagating pulse travels. β_1 is given by [24]:

$$\beta_1 = \frac{1}{v_g} = \frac{n_g}{c} = \frac{1}{c}(n + \omega\frac{\partial n}{\partial \omega}) \tag{2.9}$$

The second term β_2 represents the dispersion of the group velocity (GVD) [6]. It causes the different spectral components of the propagating pulse to travel with different velocities, then resulting in either the stretching or compression of the optical pulse. The sign of β_2 determines the impact on the optical pulse as it defines which wavelengths travel faster. A positive GVD corresponds to the normal dispersion regime where the higher is the frequency, the slower is the velocity of propagation, whereas a negative GVD corresponds to the anomalous dispersion regime. The value for which the dispersion is null is termed the zero-dispersion wavelength (ZDW). β_2 is given by:

$$\beta_2 = \frac{\partial \beta_1}{\partial \omega} = \frac{1}{c}(2\frac{\partial n}{\partial \omega} + \omega\frac{\partial^2 n}{\partial \omega^2}) \tag{2.10}$$

The evolution of β_2 as a function of wavelength for fused silica is shown in Fig.2.5b. In the telecommunication domain, dispersion is usually expressed with respect to wavelength by introducing the dispersion parameter D, defined as:

$$D = \frac{\partial \beta_1}{\partial \lambda} = -\frac{2\pi c}{\lambda^2}\beta_2 \tag{2.11}$$

The dispersion parameter D and β_2 have inverse signs and when the propagation distance z is known, one can obtain a straightforward link between wavelength and time using the accumulated dispersion $D_{acc} = D \cdot z$ (in ps/nm).

Even if in most practical cases, the contribution of β_2 dominates, it can be necessary to introduce the third-order dispersion (TOD) β_3 when the central wavelength is close to the ZDW or when the pulse is ultra-short (< 1 ps) [6]. Contrary to β_2 that linearly broadens or compresses the pulse

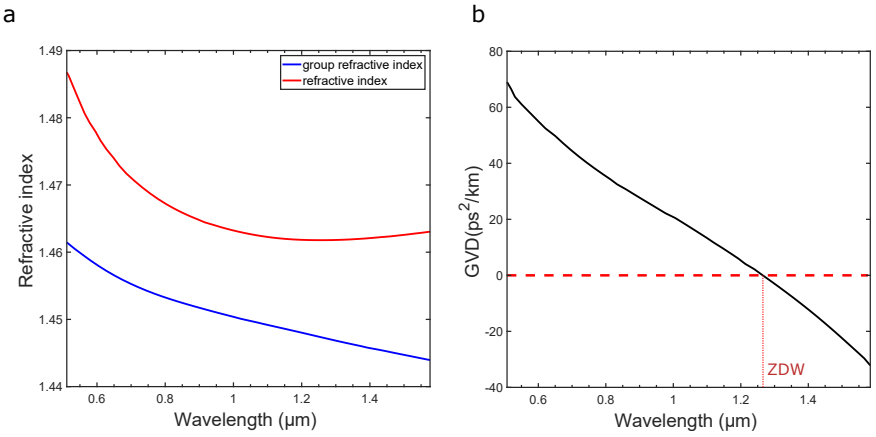

Figure 2.5: **Wavelength dependency of the refractive index and its impact on the GVD.** a) refractive index evolution as a function of wavelength: refractive index (red), group refractive index (blue). b) group velocity dispersion evolution with respect to wavelength [6].

duration, the TOD asymmetrically distorts the pulse in the time domain and is given by:

$$\beta_3 = \frac{\partial \beta_2}{\partial \omega}|_{\omega=\omega_0} = \frac{1}{c}(3\frac{d^2n}{d\omega^2} + \omega\frac{d^3n}{d\omega^3}) \tag{2.12}$$

The isolated effect of the material properties on the refractive index can be quantified on bulk samples of silica. However, the structure of the optical fiber can also have a significant impact on the refractive index. The governing equation for the propagation of a laser pulse in an optical fiber (see next sections) is derived from Maxwell's equations [6,25] with specific boundary conditions. These boundary conditions are fixed by the fiber structure, the wavelength of the laser pulse as well as the refractive index difference between the core and cladding. Those boundary conditions impose that, although most of the propagating light must be confined within the core, an exponentially decaying field propagates in the cladding. Consequently, the traveling wave does not only experience the refractive index of the core, but also that of the cladding. This leads to a total refractive index that is frequency-dependent and slightly lower than that of the core, called the effective refractive index n_{eff}. For a given transverse mode, longer wavelengths are prone to penetrate the cladding farther than shorter wavelengths. Thus, this leads longer wavelengths to have a higher exposure to the cladding refractive index and their corresponding effective refractive index would be then lower than that of shorter wavelengths. It should be noted that the effective refractive index comprises the contributions of both the material and waveguide. In this case, the propagation constant is given by:

$$\beta(\omega) = n_{eff}(\omega)\frac{\omega}{c} \tag{2.13}$$

Unlike ordinary fibers, the waveguide effect on the refractive index in a PCF can be intense. For this reason, the structure of the PCF can greatly influence its dispersive properties and can be designed to tailor the dispersion over extremely wide spectral ranges, and for instance to achieve anomalous dispersion at wavelengths that are shorter than 1 μm [16].

2.3 Nonlinear effects in optical fibers

In the core of an optical fiber, as any other dielectric material, the propagation of an oscillating electromagnetic wave stimulates the medium to behave as a set of oscillating dipoles due to the Lorentz force. The number of dipoles induced per unit of volume represents the induced polarization of the medium. Under the influence of a relatively weak oscillating electromagnetic wave, the induced polarization and the incident electric field are linked by the following expression:

$$\mathbf{P}(t) = \epsilon_0 \chi^{(1)} \cdot \mathbf{E}(t) \tag{2.14}$$

where ϵ_0 is the vacuum permittivity and $\chi^{(1)}$ is the first order electric susceptibility and is considered as only contribution to the induced polarization vector. However, when an intense electromagnetic wave propagates through the medium, it induces an anharmonic response of the bound electrons. Consequently, the optical properties become dependent on the propagating wave, and its response becomes nonlinear. In this case, the induced polarization vector is represented as follows:

$$\mathbf{P} = \epsilon_0 \left(\chi^{(1)} \cdot \mathbf{E} + \chi^{(2)} : \mathbf{EE} + \chi^{(3)} : \mathbf{EEE} + \ldots \right) \tag{2.15}$$

where $\chi^{(i)}$ is the i^{th}order of the susceptibility. On the one hand, Eq. 2.15 shows that the medium responds linearly to the electric field through the first order susceptibility, which represents the dominant contribution to the polarization vector. On the other hand, the higher order susceptibilities are responsible for the nonlinear response of the medium. For this response to be significant, the electric field is required to be sufficiently intense since the higher order susceptibilities have a considerably smaller values compared to the first order. The induced polarization vector is usually represented in the following manner:

$$\mathbf{P}(r,t) = \mathbf{P}_L(r,t) + \mathbf{P}_{NL}(r,t) \tag{2.16}$$

Where P_L represents the linear part of the induced polarization vector while P_{NL} represents the nonlinear part. The susceptibilities with even orders vanish when the medium of propagation is centrosymmetric, such as in silica. In optical fibers, the second ordrer nonlinearities (linked to $\chi^{(2)}$) can then be neglected and the nonlinear effects stem from the third order susceptibility $\chi^{(3)}$. The latter is a tensor of the fourth rank and generally has 81 elements. However, for silica and other isotropic materials, $\chi^{(3)}$ has three independent elements that can be used as a basis to represent it in the following manner [6]:

$$\chi^{(3)}_{ijkl} = \chi^{(3)}_{xxyy}\delta_{ij}\delta_{kl} + \chi^{(3)}_{xyxy}\delta_{ik}\delta_{jl} + \chi^{(3)}_{xyyx}\delta_{il}\delta_{jk} \tag{2.17}$$

with δ_{ij} has a value of one only when $i = j$. In silica, the three independent elements $\chi^{(3)}_{xxyy}$,$\chi^{(3)}_{xyxy}$ and $\chi^{(3)}_{xyyx}$ have almost the same contribution to $\chi^{(3)}$ and define their relative magnitudes. For a linearly polarized electromagnetic wave along the x-axis, $\chi^{(3)}_{xxxx}$ is the only element of the tensor that contributes to $\chi^{(3)}$. This allows for a scalar representation of the induced nonlinear polarization

of the medium. $\chi^{(3)}_{xxxx}$ is given by:

$$\chi^{(3)}_{xxxx} = \chi^{(3)}_{xxyy} + \chi^{(3)}_{xyxy} + \chi^{(3)}_{xyyx} \tag{2.18}$$

$\chi^{(3)}$ can also be represented as a complex entity with a real and imaginary parts:

$$\chi^{(3)} = \chi'^{(3)} + i\chi''^{(3)} \tag{2.19}$$

On the one hand, the real part of the third order susceptibility is responsible for the nonlinear effects that are said to be elastic, where there is no transfer of energy between the propagating electromagnetic waves and the medium of propagation. This results either in the creation of new waves from the annihilation of the incident wave (third harmonic generation or four-wave mixing) or in the spectral modification of the incident wave without any change in its energy. This phenomenon is known as the optical Kerr effect. In this case, the refractive index becomes dependent on the intensity of the incident wave, as detailed in the next section. This process is naturally efficient as its phase matching conditions are automatically satisfied.

On the other hand, the imaginary part of the third order susceptibility is responsible for the inelastic nonlinear effects. In this case, a transfer of energy occurs between the wave and the medium, via the effects of stimulated Raman scattering (SRS) or stimulated Brillouin scattering (SBS). In the following, we detail the nonlinear effects that will be used or encountered in the experiments presented in the next Chapters, and a full description of the different nonlinear effects can be found in several reference textbooks (e.g. [6,7]).

2.3.1 Self-phase modulation

As mentioned previously, a high optical intensity in a medium causes a change in the refractive index and thereby a nonlinear phase delay to the propagating light. As this phase shift is induced by the optical wave itself, this phenomenon is termed self-phase modulation (SPM). The change in the refractive index due to the nonlinear ($\chi^{(3)}$) contribution is then proportional to the optical intensity I and can be written as follows:

$$\Delta n(\omega, |E|^2) = n_2|E|^2 = n_2 I \tag{2.20}$$

where n_2 (m^2/W) is the nonlinear refractive index. For a linearly polarized (along the principal axis of the fiber) laser pulse, n_2 relates to the third order susceptibility $\chi^{(3)}$ as follow:

$$n_2 = \frac{3}{8n} Re(\chi^{(3)}_{xxxx}) \tag{2.21}$$

The nonlinear phase accumulated over a distance L can also be expressed as:

$$\phi_{NL} = n_2 k_0 L|E|^2 \tag{2.22}$$

where ϕ_{NL} is the nonlinear phase and k_0 the wavevector.
As the intensity of a short laser pulses rapidly changes with time, this results in a fast change of the nonlinear phase it experiences due to SPM and, in turn, to the generation of new spectral components that broaden the original spectrum. The spectral broadening $\Delta\omega$ of the laser pulse thereby depends on the pulse's temporal shape and is given by:

$$\Delta\omega = -\frac{\partial\phi_{NL}}{\partial t} = -n_2 k_0 L \frac{\partial|E(t)|^2}{\partial t} \tag{2.23}$$

2.3.2 Cross-phase modulation

When two electromagnetic waves having different wavelengths propagate through a medium simultaneously, they can be coupled through the third order susceptibility $\chi^{(3)}$ yet without any transfer of energy. This occurs when the change of the refractive index due to the intensity of one beam induces a nonlinear phase on the other. The consequences of this effect, called cross-phase modulation (XPM), on the optical pulse are then similar to SPM, as the pulse spectrum will be broadened. The total electric field of two laser pulses that are polarized to be propagating simultaneously through an optical fiber can be expressed as:

$$\mathbf{E} = \frac{1}{2}\tilde{a}_x \sum_{j=1}^{2} E_j \exp\left[i(\beta_j z - \omega_j)t\right] + c\cdot c \tag{2.24}$$

with $c\cdot c$ being the complex conjugate. The induced nonlinear polarization due to E_1 and E_2 have four terms, while two of them do not involve any transfer of energy:

$$P_{NL}(\omega_1) = \frac{3\epsilon_0}{4}\chi^{(3)}_{\chi\chi\chi\chi}\left(|E_1|^2 + 2|E_2|^2\right)E_1 \tag{2.25}$$

$$P_{NL}(\omega_2) = \frac{3\epsilon_0}{4}\chi^{(3)}_{\chi\chi\chi\chi}\left(|E_2|^2 + 2|E_1|^2\right)E_2 \tag{2.26}$$

The first term of both equations represents the SPM process while the second term represents the XPM process and the resulting nonlinear phase is then given as:

$$\phi_{NL} = n_2 k_0 L\left(|E_1|^2 + 2|E_2|^2\right) \tag{2.27}$$

If we consider that the two interacting electric fields have the same intensity, the contribution of XPM to the nonlinear phase in this case is twice as much the contribution of SPM. This means that one pulse's contribution to the nonlinear phase induced on the second pulse is greater than that caused by itself.

2.3.3 Four-wave mixing

Four-wave mixing (FWM) is a nonlinear parametric process that involves the interaction of at least two different optical frequency components (and up to four waves) but also originates from

the same Kerr nonlinearity ($\chi^{(3)}$) as SPM and XPM. The medium of propagation is not actively involved in the process, but only mediates the interaction of the four waves. Let us consider four linearly polarized electric fields along the principal axis of the optical fiber:

$$\mathbf{E} = \frac{1}{2}\tilde{a}_x \sum_{j=1}^{4} E_j \exp\left[i(\beta_j z - \omega_j)t\right] + c \cdot c \tag{2.28}$$

This allows for the representation of the induced polarization vector in the following manner:

$$\mathbf{P} = \frac{1}{2}\tilde{a}_x \sum_{j=1}^{4} P_j \exp\left[i(\beta_j z - \omega_j)t\right] + c \cdot c \tag{2.29}$$

The nonlinear polarization vector P_{NL} then contains many terms representing several nonlinear effects, among which is the FWM process. However, for an efficient FWM to occur and contrary to SPM, phase matching conditions must satisfied. FWM indeed necessitates the matching of both the frequencies of the four waves and their wave vectors. The former matching ensures the conservation of energy while the later ensures the conservation of momentum, as illustrated in Fig. 2.6.

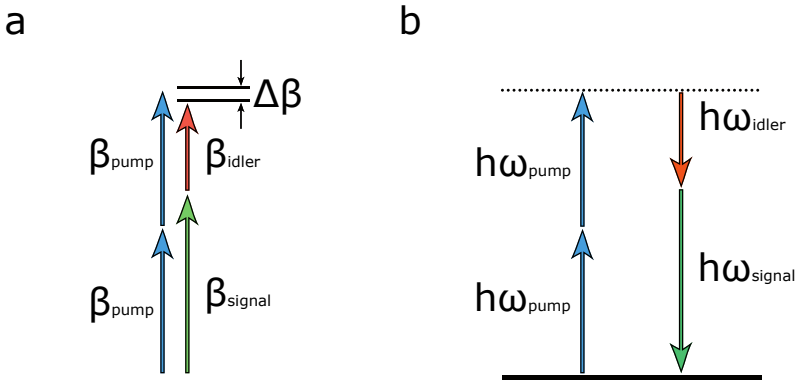

Figure 2.6: **Phase-matching conditions for the FWM process.** a) momentum conservation. b) energy conservation.

In the quantum mechanical sense, the FWM process requires the annihilation of two pump photons from one or several waves and the generation of signal and idler photons. The signal photon has more energy than the idler photon and their combined energy is axiomatically equal to that of the annihilated photons. When the two annihilated photons have the same frequency, the process is called degenerate four wave mixing (DFWM). In this case, only a single pump pulse is needed to generate a signal and idler pulses located symmetrically around the pump in the spectral domain. The conditions for the conservation of energy and momentum are then expressed as [6]:

$$2\omega_{pump} = \omega_{signal} + \omega_{idler} \tag{2.30}$$

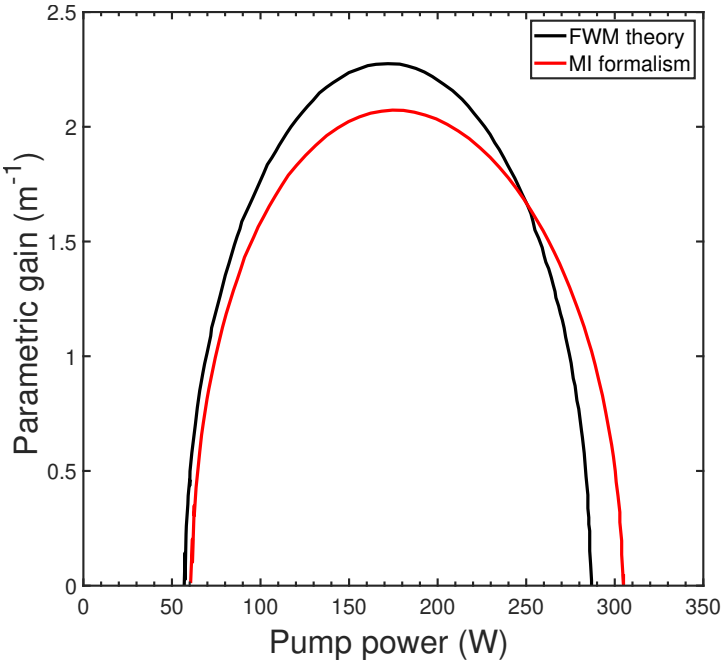

Figure 2.7: **Small signal parametric gain of the FWM process** as a function of pump power simulated based on FWM theory (black) and modulation instability formalism (red) [31]. The parameters are $\beta_2 = 6.6 \times 10^{-26}$ s^{2}m^{-1}, $\lambda_p = 532$ nm and $\gamma = 53.5$ W^{-1}km^{-1}, $\Delta n = 5.5 \times 10^{-4}$, $\lambda_s = 535.7$ nm [32].

$$2\beta_{pump} = \beta_{signal} + \beta_{idler} \tag{2.31}$$

On the one hand, ω_{pump}, ω_{signal} and ω_{idler} represent the frequency of the annihilated photons, the generated signal and idler, respectively. On the other hand, β_{pump}, β_{signal} and β_{idler} represent the wave vectors for the pump, signal and idler, respectively. The idler and signal are created from noise due to the parametric gain of the FWM process [26–30] which is dependent on the pump power and the phase matching conditions as follows [6]:

$$g = \sqrt{(\gamma P_{pump})^2 - (\Delta k/2)^2} \tag{2.32}$$

with

$$\Delta k = \beta_{signal} + \beta_{idler} - 2\beta_{pump} + 2\gamma P_{pump} \tag{2.33}$$

Where P_{pump} is the pump power. However, the maximum of the parametric gain in Eq. 2.32 is not achieved when the wave vectors are matched due to the effects of SPM and XPM on the FWM process, as they also contribute to the phase mismatch. They indeed shift the gain maximum to where the wave vector mismatch cancels their effect on the phase matching ($\beta_{signal} + \beta_{idler} - 2\beta_{pump} = -2\gamma P_{pump}$). As a result, Δk represents the effective phase mismatch. Fig. 2.7 shows an example of the parametric gain as a function of the pump power. The effective phase mismatch can also be seen as the sum of the contributions of material and waveguide dispersion in addition

to the contribution of the nonlinear effects. All of the formerly stated effects can indeed participate in the phase change both in linear and nonlinear manners:

$$\Delta k = \Delta k_M + \Delta k_W + \Delta k_{NL} \tag{2.34}$$

where Δk_M, Δk_W and Δk_{NL} define the phase mismatch due to material dispersion, waveguide dispersion and nonlinearity, respectively. The cancellation of the effective phase mismatch then necessitates at least one of these contributions to be negative. The waveguide contribution to the phase mismatch depends on the structure of the optical fiber and, in single mode fibers, is negligible compared to the contribution of the material dispersion. However, when the pump wavelength is in the vicinity of the zero dispersion wavelength (ZDW) of the fiber, the two contributions become comparable. As a result, if the pump power is kept at a low value, the contribution of the nonlinear effects Δk_{NL} is also reduced and Δk_W can compensate for Δk_M and Δk_{NL}, for idler and signal wavelengths that are not too far from the pump wavelength. On the other hand, if the pump wavelength is far from the ZDW, and by considering the scalar approach where all the involved electric field in the FWM process are linearly polarized (same axis), the phase matching in single mode fiber requires the pump wavelength to be higher than the ZDW in order to obtain a negative Δk_M. Phase matching is then achieved through the adjustment of the pump power that changes the contribution of the nonlinear effects. However, if the four waves have different polarization states, phase matching in the normal dispersion regime is also possible [6].

2.3.3.1 Fiber optic parametric amplifiers and oscillators

As stated before, when the phase matching conditions are satisfied, the parametric gain allows for the creation of signal and idler from noise through parametric generation. However, if a weak signal is set to propagate simultaneously with the pump in the optical gain medium, the parametric gain allows for the amplification of the small signal in a process called optical parametric amplification. In the case where the amplifying medium is an optical fiber, a system based on this process is call a fiber optic parametric amplifier (FOPA). Such FOPAs offer great advantages over other light sources for many of applications due to their particular characteristics. For instance, FOPA exhibit broadband gain reaching hundreds of nanometers [33] and that are not accessible to other amplifications systems such as Raman [34–36] and erbium-doped fiber amplifiers. In addition, the central wavelength of gain window of a FOPA system can be adjusted via the ZDW of the nonlinear fiber. This latter quality permits FOPA systems to amplify optical pulses in spectral regions inaccessible to other amplification systems [37]. Under the assumption that the amplification of the signal does not saturate the amplification gain, the latter can be expressed as [6]:

$$G = 1 + \left(\frac{\gamma P_{Pump}}{g}\right)^2 \sinh^2(gL) \tag{2.35}$$

where G is the signal amplification gain. In addition, since energy must be conserved in DFWM, a complementary idler is simultaneously generated. In the spectral domain, the generated idler and

the amplified signal are symmetrically located with respect the pump. Moreover, the idler's phase is opposite to that of the signal and this feature can be useful in reversing any change in the phase of the signal due to nonlinear effects like XPM [37]. The idler's gain is then given by:

$$G = \left(\frac{\gamma P_{Pump}}{g}\right)^2 \sinh^2(gL) \tag{2.36}$$

A fiber optic parametric amplifier can be turned into a parametric oscillator (FOPO) by providing a feedback to the gain medium in order to form an optical resonator. The feedback can be set in several ways. Most commonly, the pump is externally supplied while either the signal or idler is set to resonate withing the optical cavity. Several parameters such as dispersion, repetition rate of the pump as well as the quality factor of the cavity need to be taken into account in the design of the FOPO cavity, as they strongly influence its output characteristics. For instance, if the signal is set to be resonant within the FOPO cavity, a high quality factor would barely allow the resonating signal to exit. This means that although the signal is the one being amplified, the FOPO main output is the generated idler.

For a pulsed pump, parametric generation occurs with the first pump pulse propagating through the gain medium. This results in the creation of signal and idler photons from noise. The feedback allows to set either of the generated wavelengths to resonate in the cavity in order to synchronise it with the fresh pump pulse for seeding the parametric amplification process. This process and its complex dynamics are thoroughly detailed and investigated in Chapters 2 and 3.

2.4 Pulse propagation in optical fibers

In order to describe and simulate the propagation of light through an optical fiber, it is required to solve Maxwell's equations while considering the fiber structure [6, 25]. This leads to a wave equation that governs the propagation of electromagnetic waves:

$$\Delta \times \Delta \times \mathbf{E} = -\frac{1}{c^2}\frac{\partial^2 \mathbf{E}}{\partial t^2} - \mu_0 \frac{\partial^2 \mathbf{P}}{\partial t^2} \tag{2.37}$$

with E representing the electric field vector, P representing the induce polarization vector, c is the speed of light while μ_0 is vacuum permeability. The right side of the wave equation contains two related terms: the first includes the electric field while the second includes the induced polarization, defined previously in Eq. 2.15.

For an electric field that is not sufficiently intense, we can assume that the nonlinear part of the induced polarization is insignificant compared to the linear part and therefore P_{NL} can be ignored in Eq. 2.16. This assumption allows to obtain the Helmholtz equation by solving the wave equation in the frequency domain. It is given by:

$$\nabla^2 \mathbf{E}(\omega) = n^2 \frac{\omega^2}{c^2} \tilde{E}(r, \omega) \tag{2.38}$$

In order to derive a governing equation for a laser pulse propagating in an optical fiber from Eq. 2.38, the propagating electric field needs to be represented in the transverse axes as well as the longitudinal axis. Throughout this thesis, we will consider ultrashort laser pulses propagating in the core of optical fibers. In the transverse axes, the electric field of the short pulse is distributed according to the mode of propagation. In single mode fibers, the spatial distribution of the electric field can be approximated by a Gaussian distribution. In the longitudinal axis, the electric field of the pulse is described as a carrier oscillation $\exp(i\omega t)$ cased within a pulse envelope $A(z,t)$. The latter is considered to have a much smaller rate of change compared to the carrier oscillation. This consideration allows for the use of the slow varying envelope approximation (SVEA) in order to separate the carrier and envelope termsv [17]. The electric field is then represented as follows [6]:

$$\mathbf{E}(r,t) = \mathbf{A}(z,t)F(x,y)\exp[i\beta(\omega)z]\cdot\tilde{a}_x \tag{2.39}$$

where $F(x,y)$ represents the transverse field distribution function. In single mode fibers, $F(x,y)$ can be expressed as:

$$F(x,y) = \exp\left(\frac{-(x^2+y^2)}{r^2}\right) \tag{2.40}$$

with r being the width of the Gaussian distribution. In order to simplify the derivation of a governing equation for pulse propagation in an optical fiber, we assume that the laser pulse is initially linearly polarized and maintains its polarization as it propagates. This assumption results in a great simplification as it allows to shift from a vector to a scalar approach when dealing with the electric field. Moreover, it results in a considerable physical insight gain regarding the propagation process. As a result, by excluding the Raman effect [38], the resulting simplified equation that describes the pulse propagation writes as follows:

$$\frac{\partial A}{\partial z} + \frac{\alpha}{2}A + i\frac{\beta_2}{2}\frac{\partial^2 A}{\partial T^2} - \frac{\beta_3}{6}\frac{\partial^3 A}{\partial T^3} = i\gamma\left(|A|^2 A\right) \tag{2.41}$$

where α is the absorption coefficient, β_2 and β_3 are the second and third orders dispersion coefficients, respectively, and γ is the nonlinear coefficient. This equation is called the nonlinear Schrödinger equation (NLSE) where each term defines a specific effect on the propagating pulse. The first term on the left side represents the slowly varying envelope of the pulse and it should be noted that a change of variable $T = t - \beta_1 z$ is made in order to set a new frame of reference. The latter moves at the group velocity of the pulse and it further simplifies the governing equation through the elimination of the first-order dispersion term β_1. The second term represents the attenuation effect and the remaining terms on the left side account for the dispersion effects (β_2 and β_3) that influence the pulse temporal shape. Orders above the third order do not have usually a significant effect on the propagating pulse due to their small values with respect to the second order. However, they should be taken into account either when dealing with pulse durations inferior to 5 ps, or when the wavelength of the laser pulse is near the zero dispersion wavelength (ZDW) of the fiber.

The right side of Eq.2.41 corresponds to the influence of the nonlinear effects through the nonlinear coefficient γ defined as:

$$\gamma(\omega) = \frac{n_2 \omega}{c A_{eff}} \tag{2.42}$$

where A_{eff} is the effective mode area of the propagating pulse and n_2 is the frequency-dependent nonlinear refractive index. In optical fibers with small core diameters or specific guiding properties, the nonlinear coefficient can then reach very high values ($\gamma > 10$ (W.km)$^{-1}$), then favouring the triggering of nonlinear effects.

We have seen that the NLSE (Eq. 2.41) allows to study the propagation of short pulses in a relatively simple way since nonlinear effects such as SRS or SBS are not taken into account. Therefore, even though the standard NLSE provides physical insights on propagating pulse behavior, it does not provide a full description of the process. For an accurate modeling of the pulse propagation taking into account the dispersion effects to higher orders and the instantaneous as well as the delayed contributions to the nonlinear effect, the generalized nonlinear Schrödinger equation (GNLSE) has then to be used. It writes as:

$$\frac{\partial A}{\partial z} + \frac{\alpha}{2} A + i \frac{\beta_2}{2} \frac{\partial^2 A}{\partial T^2} = i\gamma (1 + \tau_{shock} \frac{\partial}{\partial T})(A(z,T) \int_{-\infty}^{+\infty} R(T') |A(z, T - T')|^2 dT') \tag{2.43}$$

where τ_{shock} is the optical shock term representing the wavelength-dependent dispersion of the nonlinearity. The integral on the right side includes the instantaneous and delayed nonlinear response, corresponding the Kerr and Raman effects, respectively.

2.5 Summary

This introductory chapter allowed us to briefly recall the main theoretical concepts on which the experimental works reported in this thesis are based. Firstly, optical fibers - standard and PCF - along with the nonlinear effects that can be encountered when propagating short pulses in them represent the backbone of the experimental setups detailed in Chapters 2 and 3, dealing with fiber optical parametric oscillators based on four-wave mixing. Secondly, a significant part of this chapter was devoted to the description of dispersion, a phenomenon that is particularly important to the design of the oscillators developed in the next Chapters but which is also the cornerstone of an ultrafast spectral measurement technique called dispersive Fourier transform (DFT) on which the dynamics study of Chapter 3 is based. Finally, the numerical simulations of pulse propagation presented in the next Chapter have been performed based on the GNLSE, which has been introduced in the previous section.

CHAPTER 3

Fiber optical parametric chirped-pulse oscillation

As a lead-in to the experimental results of this PhD thesis, this chapter aims at introducing and exploring a new method to obtain high-energy tunable pulses in spectral windows where no direct emission source is efficient or available. With this aim in view, we combine the concepts of fiber optic parametric oscillator (FOPO) and chirped pulse amplification (CPA) to design and implement a fiber optical parametric chirped pulse oscillator (FOPCPO). Such a technique would then allow to exploit the broad tunability and favorable noise properties of FOPOs together with the power scaling capabilities of CPA. This chapter is then organized as follows. After recalling the recent advances in ultrafast sources emitting outside of the wavelength windows accessible to rare-earth doped fibers, we first introduce the key elements for building a FOPCPO. We then present numerical simulations allowing, on the one hand, to select the adapted experimental parameters and, on the other hand, to anticipate the potential energy scaling possibilities of such a system. We eventually show the performances of the system developed in the laboratory, and compare them to the state-of-the-art.

3.1 Introduction

Ultrafast fiber lasers are now well-established alternatives to solid-state lasers in many research-oriented and industrial applications due to their robust, compact and alignment-free nature. Standard fiber laser technology however faces two major limitations: *(i)* the detrimental influence of nonlinear effects due the strong spatial confinement of the pulses, thus limiting the energy scaling, and *(ii)* the limited available wavelengths due to rare-earth gain fibers, restricting the tunability of such sources to spectral windows of a few tens of nanometers near 1 (Yb), 1.5 (Er) and 1.9 µm (Tm). Several approaches have been used to get around these restrictions and have been fueled by the increasing demand of high-power wavelength-flexible fiber lasers for widespread applications such as nonlinear imaging [39, 40] or coherent Raman scattering spectroscopy or microscopy [41–43] where ultrashort pulses at specific wavelengths are highly desired to promote deep tissue imaging or to match the spectral response of existing fluorophores [44]. Despite the efforts already undertaken to develop fiber-based lasers exploiting novel transitions in rare earth ions [45–49], the performances achieved in the ultrafast regime remain far from target in terms of pulse energy and laser stability. Nonlinear wavelength conversion therefore constitutes an attractive alternative for the generation of ultrashort pulses at new wavelengths.

The common approaches enabling the spectral shifting of ultrashort pulses mostly rely on the soliton self-frequency shift [50–52] and self-phase modulation [53–55] effects in single-mode fibers. The soliton self-mode conversion reported recently in multimode fibers also appears as an efficient mechanism for frequency shifting [56]. Nevertheless, the need for high peak power dechirped pulses to pump such sources limits their scalability due to intensity-related damages. The best performances are currently reached with solid-state optical parametric systems [57] which are the race horses of several fields of research but their complexity, cost, and alignment sensitivity hinder their use outside the laboratory environment.

The fiber-based counterparts of these systems, which are based on degenerate four-wave mixing (DFWM), are very promising to provide powerful and widely tunable ultrafast light pulses. In particular, pumping in the weakly normal group velocity dispersion (GVD) region enables the generation of signal/idler pulses at frequencies widely separated from the pump [58]. To avoid saturation of the nonlinear conversion process, the concept of fiber optical parametric chirped-pulse amplification (FOPCPA) [59] has been introduced. This concept is an extension of the well-known chirped pulse amplification principle to FWM-based system where a pump pulse is temporally stretched in order to reduce its peak power while maintaining the totality of its energy. Thus, the saturation of the gain medium as well as its damage are avoided. the main difference is that the amplification gain is due to FWM and not spontaneous emission. This paves the way for substantial energy scaling of the converted signal and idler waves [60–63]. Recently, the µJ barrier has been passed through the combination of strongly stretched pump pulses with a Raman-assisted parametric amplifier in an all-solid photonic bandgap fiber [64]. However, the signal/idler frequencies are close to the pump frequency due to the anomalous GVD of the fiber. More recently, the FOPCPA concept has been successfully extended to the normal dispersion

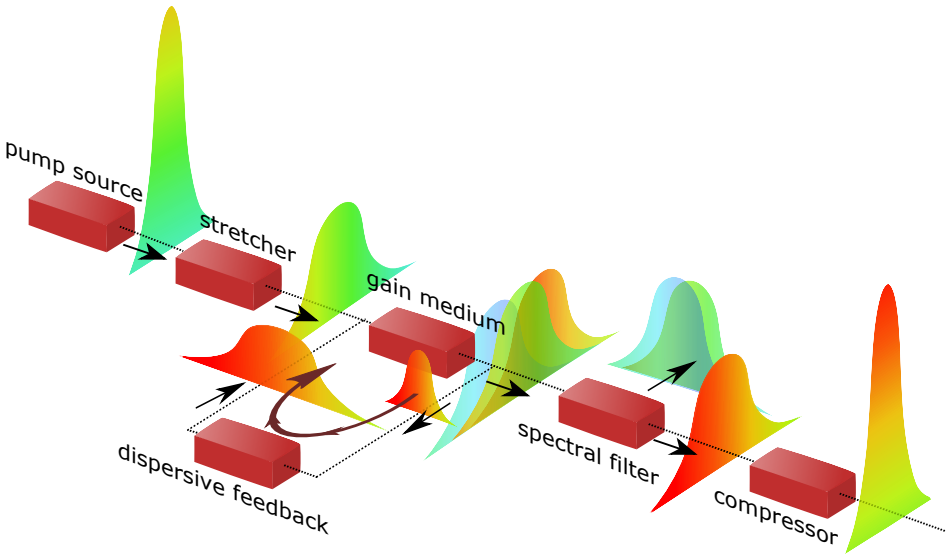

Figure 3.1: **Principle of fiber optic parametric chirped pulse oscillator:** the pump pulse is chirped by means of a stretcher prior to gain medium in order to avoid the saturation and damage of the latter. The propagation of the stretched pulse through the gain medium results in the generation of seed signal and idler from noise through the parametric generation process. The generated seed signal (or idler) is stretched and fed back to the gain medium to be amplified by the new coming pump pulse. the Amplified signal (or idler) is then subsequently compressed to its Fourier limits.

regime, then leading to the generation of high-energy sub-picosecond pulses with a large frequency span [65–68]. Nevertheless, the need for a seed source limits the FOPCPA tunability. A solution to overcome this limitation consists in using a resonant fiber optical parametric oscillator (FOPO) which also exhibits a better signal-to-noise ratio than a single-pass amplifier [41] and allows for new degrees of freedom in the design of parametric sources, notably through the dispersion map of the cavity [69,70]. The principle of fiber optic parametric chirped pulse oscillator (FOPCPO) is shown on Fig3.1. It is indeed well-established that the combination of a normal-dispersion cavity with FWM in a photonic crystal fiber gives rise to linearly chirped signal and idler pulses, thus allowing the access to high energy levels [71] and ultrashort dechirped pulses [72]. To date, the best results in terms of energy are obtained from a FOPO featuring a 6 cm-long microstructured fiber which delivered 250 nJ sub-picosecond pulses [71]. However, the high peak-power of the picosecond narrow-band pump pulses can be a limitation for further energy scaling. The combination of chirped pump pulses with normal dispersion fiber parametric oscillators then appears very attractive for energy scaling. Preliminary numerical simulations of such a fiber optical parametric chirped-pulse oscillator (FOPCPO) have shown that such a concept can enable a better control over the output pulses features [73]. In this chapter, we then report the experimental demonstration of a high-energy FOPCPO system and numerically analyse its operation and discuss its potential for performances improvement.

3.2 Experimental implementation of a FOPCPO

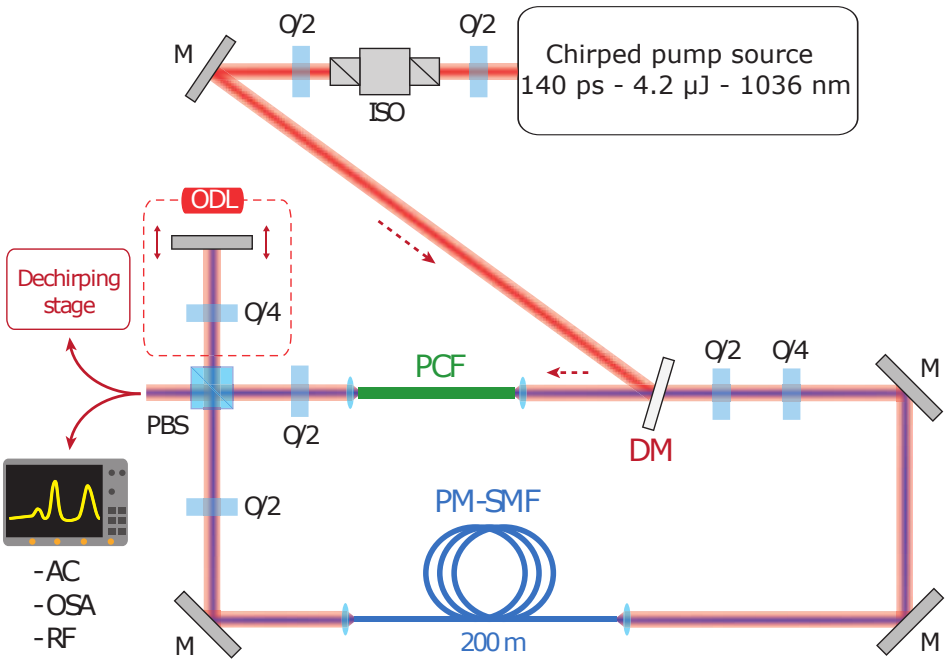

Figure 3.2: **FOPCPO: experimental setup.** PCF: photonic crystal fiber, ODL: optical delay line, PM-SMF: polarization-maintaining single-mode fiber, ISO: isolator, DM: dichroic mirror, M: mirrors, PBS: polarizing beamsplitter.

Our fiber optical parametric chirped-pulse oscillator, schematically depicted in Fig. 3.2, is pumped by highly chirped pulses around 1036 nm and generates chirped signal and idler pulses broadly tunable around 890 and 1250, respectively. Nonlinear frequency conversion is realized in a photonic crystal fiber (PCF) and wavelength tuning is achieved using the time-dispersion tuning technique. The generated idler and signal are subsequently dechirped using a grating compressor. The principles and properties of those building blocks are detailed in the following sections.

3.2.1 Pump source

As it is required by the FOPCPO principle, the gain medium needs to be pumped using a chirped-pulse pump source. In our experiment, we use an ytterbium-doped fiber-based chirped-pulse amplifier system operating at 1036 nm. The different stages involved in the implementation of this laser source are illustrated in Fig.3.3. The system is seeded by a homemade all-fiber oscillator operating in the dispersion-managed soliton regime and delivering a stable pulse train at 18 MHz repetition rate. This SESAM-based mode-locked laser provides a typical parabolic-shaped

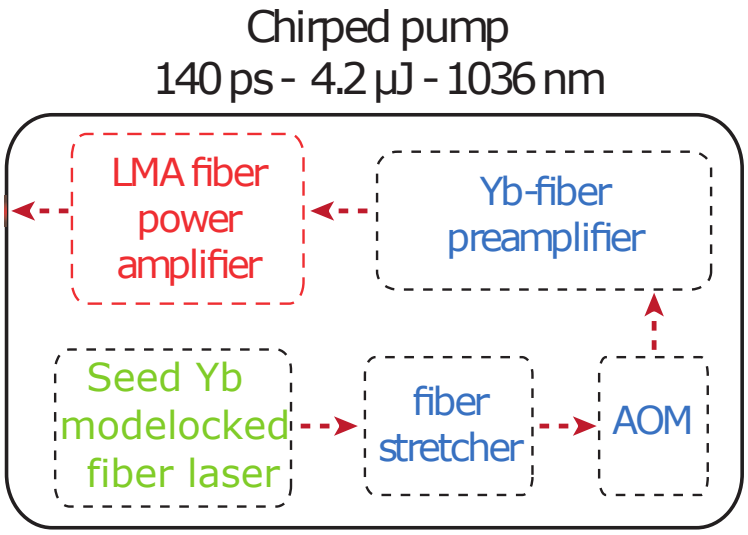

Figure 3.3: **Architecture of the pulsed pump source.** AOM: acousto-optic modulator, LMA: large mode area.

spectrum shown in Fig. 3.4. Moreover, it presents an excellent signal-to-noise ratio (SNR) of more than 75 dB.

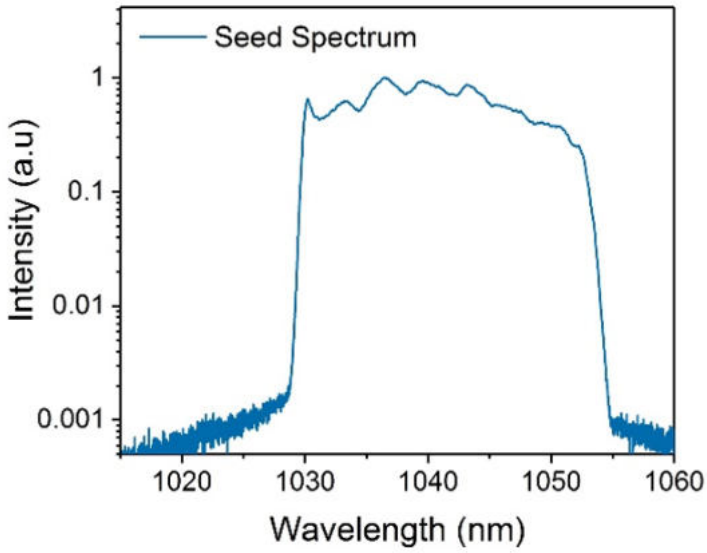

Figure 3.4: **Parabolic-shaped optical spectrum of the seed pulses.**

The seed pulses are further stretched by means of a long passive fiber. To access the high energy regime, a fiber acousto-optical modulator (AOM) is placed prior to the main power amplifier in order to lower the fundamental repetition rate down to 938 kHz. Two core-pumped Yb-doped fiber preamplifiers are then used to compensate for the losses in both the stretcher and the AOM. The power amplifier is based on a cladding-pumped heavily ytterbium-doped polarizing large

mode area microstructured fiber. Prior to injection in the FOPCPO cavity, pump pulses are then linearly chirped up to 140 ps with an energy of 4.2 µJ and a spectrum centered at 1036 nm with ∼7 nm bandwidth as shown in Fig.3.5. An isolator and two half-wave plates (HWP) protect the pump from any feedback and allow for a precise control of the incident power and polarization.

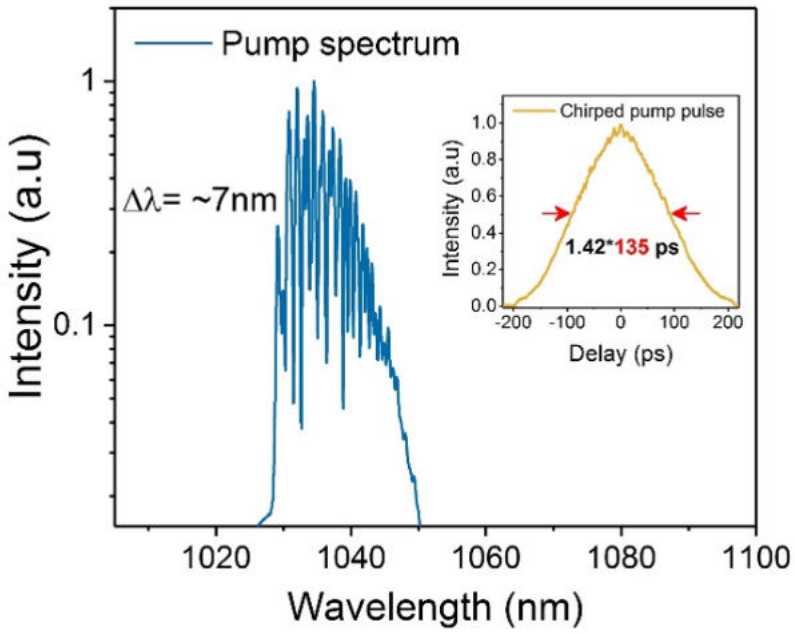

Figure 3.5: **FOPCPO pump spectrum and autocorrelation trace.**

3.2.2 FOPO cavity

In the FOPO cavity, pump pulses are injected into a 11-cm long PCF (NKT SC-5.0-1040) shown in Fig.3.6, featuring a core diameter of 4.8 µm, a mode field diameter 4.2 µm at 1060 nm and a λ_{ZDW}=1040 nm. The injection into the PCF is performed via a dichroic mirror (DM) and a 4 mm focal lens, subsequently generating wideband parametric gain at long (idler) and short (signal) wavelengths through DFWM. Note that the DM causes ∼10 % losses to the pump, so that the incoming energy on the PCF facet reaches 3.8 µJ. The choice of the PCF as a gain medium is fueled by the advantageous features that it offers. For instance, although the background material in this PCF is fused silica, its structural properties lead to the alteration of its dispersive properties through inducing substantial waveguide dispersion especially at longer wavelengths. This results in the shifting of its ZDW to 1040 nm, which is indeed shorter than the ZDW of fused silica. The ZDW is a key parameter for efficient FWM process since it defines whether the pumping of the gain medium falls within the normal or anomalous dispersion regions and consequently determines the wavelengths for maximal parametric gain for the signal and idler.

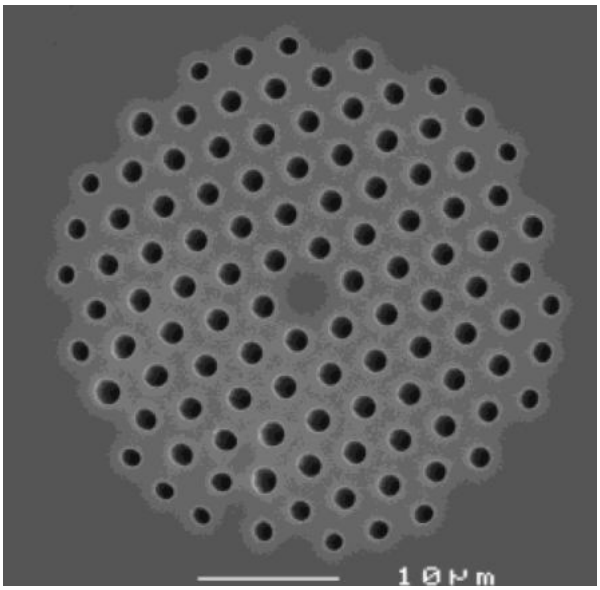

Figure 3.6: **Scanning electron micrograph of the utilized PCF's cross section.** [source: NKT Photonics]

In addition, the PCF possesses a high nonlinear coefficient and maintains single-mode propagation over a large spectral range. Although the importance of the former feature for achieving high conversion efficiencies is obvious, the latter feature is as important due to the fact that it prevents the mode field area from substantially varying with respect to wavelength. Consequently, it leads to the preservation of high mode field overlap through the FWM process. This way, achieving high conversion efficiency does not require relatively long PCF and therefore the walk-off effect can be neglected, especially since the pump pulses are temporally stretched.
When a high conversion efficiency is obtained, the assumption that the pump remains undepleted through the FWM losses its validity as the idler and signal peak powers cannot be ignored. In this case, the effective phase mismatch representation must be changed to include the effect of the idler and signal peak powers. It is then expressed in the following manner:

$$\Delta\beta = \Delta\beta_0 + \gamma(P_{pump} - P_{idler} - P_{signal}) \tag{3.1}$$

This representation of the effective phase mismatch results in the shift of the wavelength of maximal gain towards the pump. This is due to the fact that a smaller $\Delta\beta_0$ is required to obtain effective phase matching [74]. Consequently, the wavelength of maximal gain would change in every round-trip during the build-up process, leading to the change of the resonating wave peak power until it converges to a stable steady state value.
After the PCF, signal, idler and residual pump beams are divided towards output coupling and a feedback arm using a polarizing beam splitter and a half waveplate. The signal pulses are then selected to be resonant and to match with fresh pump pulses by tuning the end-mirror on the free-

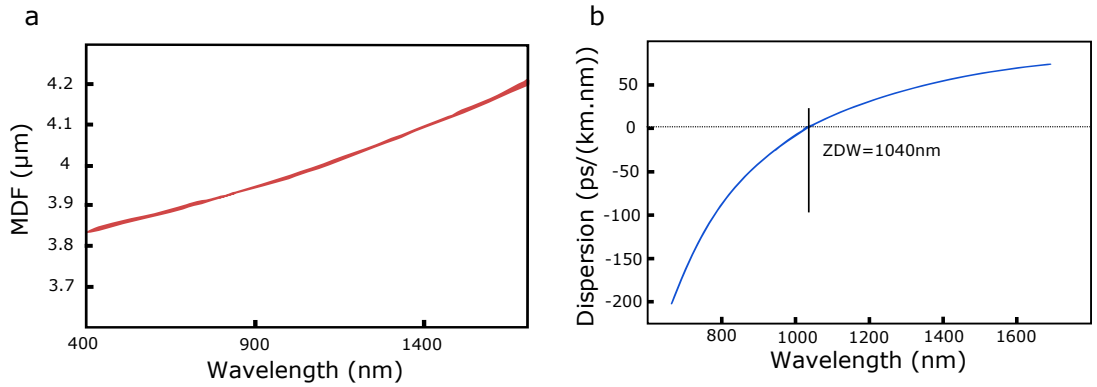

Figure 3.7: **Mode field diameter and GVD curves as a function of wavelength.** a) mode field diameter. b) group velocity dispersion.

space optical delay line (ODL) and using a $\sim$ 200-m long polarization-maintaining single-mode fiber (SMF, HP-780-PM). In addition to synchronize the resonating signal with the new incoming pump pulse in the gain medium, the feedback acts as a dispersive filter since it temporally stretches the resonating signal and consequently limits the overlap with the new coming pump to a specific spectral band stimulating its amplification, and since the seed signal is kept withing the FOPO cavity, it becomes spectrally narrower with every round trip until the effect of dispersion becomes negligible, as it is proportional to the spectral width.
In addition, when we consider the high nonlinearity of the parametric gain medium, we must assume that the amplified spectral band of the signal would experience spectral broadening due to SPM. It is then spectrally filtered due to the dispersion of the ODL. This periodic process leads the spectral phase of the signal to be constantly altered along its propagation within the FOPO cavity. A stable output can be obtained when the resonating signal finally restores its initial duration after a roundtrip.
Another major factor influencing the dynamics of the performance of the FOPO is the coupling into the ODL. At the output of the gain medium, we find the amplified signal, generated idler and residual pump. At this stage, most of the energy is coupled out of the FOPO cavity while a small proportion is fed back to the gain medium. With respect to the FOPO cavity, the coupling out of the signal is considered as loss and a steady state stable regime is not reached unless and equilibrium between gain and loss is achieved. Therefore, the feedback ratio is a very important parameter that should be taken into account.
In the setup shown in Fig. 3.2, we can see that a large part of the FOPO cavity is in free space. This feature gives us control over several parameters and facilitates the improvement of the system performances. For instance, the half-wave plate and polarizing beamsplitter at the end face of the PCF allow for the adjustment of the feedback ratio for an optimal efficiency and stability. The system also offers control over the polarization planes of the pump and resonating signal, and their adjustment can lead to the increase of the conversion efficiency as well.
In a round-trip, the resonant signal centered around 900 nm experiences a total second order dispersion of about +7.04 ps^2, mostly due to the SMF. The non-resonant idler around 1230 nm

and pump experience low total second order dispersions of -3.25×10^{-3} ps^2 and +9.4×10^{-5} ps^2, respectively, which are only imposed by the PCF as they are filtered out by the dichroic mirror. The signal beam is eventually combined with the pump beam through the DM, and the pulses are simultaneously coupled back into the PCF.

3.2.3 Dechirping stage

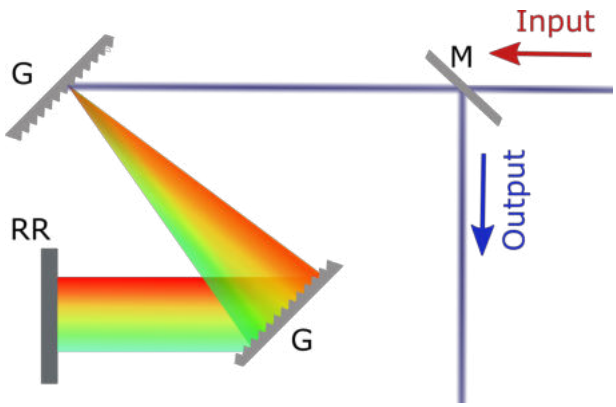

Figure 3.8: **Schematic representation of the dechirping stage** (top view). G: diffraction grating, M: mirror, RR: roof retroreflector mirror.

The dechirping stage is set to compress the chirped pulses to their Fourier limits through reversing the effect of GVD. This is performed through imposing different propagation distances for different optical frequencies in order to compensate for the existing time delay between them. In this context, the dechirping stage can be implemented using several architectures. In our case, we used the compressor system illustrated in Fig.3.8. It is composed of two parallel and identical diffraction gratings where the first disperses the frequencies of the incoming stretched pulse in space while the second collimates the diffracted light in the form of a spectral line. A roof retroreflector mirror is then set to vertically displace the spectral line and sends it back through an optical path parallel to the optical path that light has already crossed. This way, the first grating collects the spatially dispersed optical frequencies in a single beam. This back and forth propagation affects the spectral phase of the stretched pulse by imposing a negative GVD. The latter depends mainly on the grating period as well as the distance between the gratings. Consequently, by adjusting the latter parameter, the compressor system can temporally compress the stretched pulses near their Fourier limits.

3.3 Numerical simulation & potential energy scaling

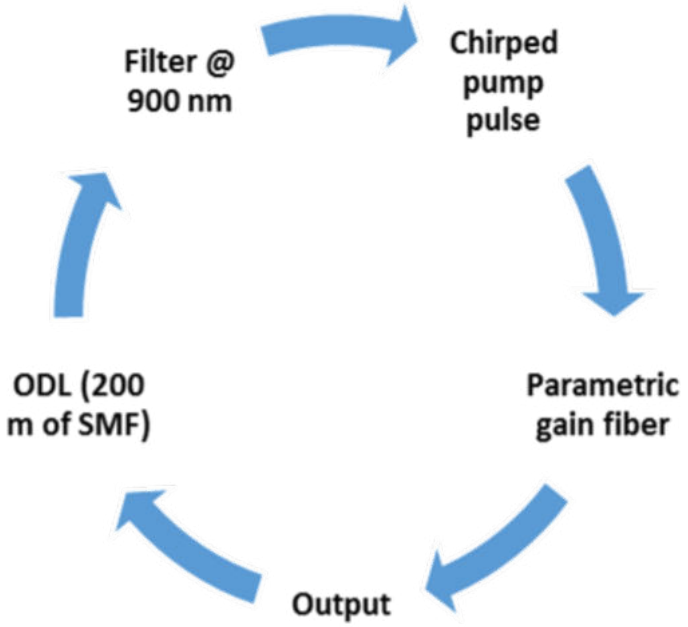

Figure 3.9: **Flowchart depicting the simulation process.** The chirped pump pulse is set to propagate through the parametric gain fiber. The output of the gain fiber is later stretched, filtered and synchronized with the new incoming pulse. The filter ensures that the signal is the only resonating wave within the FOPO cavity.

In this section, we explored the FOPCPO performances through numerical simulations using the above-mentioned cavity parameters according to the process depicted in Fig. 3.9. We use a commercial software (Fiberdesk) to solve the extended nonlinear Schrödinger equation along the FOPO cavity. First of all, a chirped pump pulse with energy of 2 µJ, pulse duration of ∼140 ps and spectral bandwidth of ∼7.9 nm is set to propagate through the parametric gain fiber (PCF). It should be noted that the pulse energy is set inferior to the pulse energy of the pump source in order to account for the injection losses in the PCF. The latter acting as the parametric gain medium is set to have the following parameters: γ = 0.014 $W^{-1}m^{-1}$, β_3 = 6.66×10^{-5} ps^3m^{-1}, and β_4 = -1.31×10^{-7} ps^4m^{-1} which correspond to the parameters of the PCF evaluated at 1036 nm. At the output of the PCF, most of the energy is coupled out of the cavity while a small portion is fed back to the PCF. In here, we assume a feedback ratio of 4×10^{-4}. The PM feedback fiber (HP-780-PM) is modeled as standard single mode fiber with the following parameters γ = 0.01 $W^{-1}m^{-1}$, β_2 = 0.027 ps^2m^{-1}, β_3 = 3×10^{-5} ps^3m^{-1}, and β_4 = -1×10^{-8} ps^4m^{-1} at 1036 nm. This fiber leads to the temporal separation of the fed-back signal, idler and residual pump as well as their stretching. The length of the SMF fiber is set to synchronize the resonating signal with the fresh pump pulse (the FOPO cavity length matches the repetition rate of the laser source). The SMF fiber is followed by a

spectral filter to ensure that only the short wave signal is resonant inside the cavity. This way, a full round trip is completed and the process is to be repeated. In this manner, we can view the progress of the parametric process through small segments of the FOPO cavity starting from the first injected pump pulse till the steady state is reached.
By setting the simulated FOPCPO to be resonant at 900 nm. the simulation shows that the FOPCPO generates a broadband idler around 1228 nm and a narrow-band signal around 900 nm as shown in Fig. 3.10a. On the one hand, the thin spectrum of the signal can be mainly attributed to the filtering effect it is subjected to by the SMF fiber through time dispersion tuning. In this sense, the stretching of the resonating signal leads to limit its overlap with the fresh coming pump pulse to specific spectral region. On the other hand, since the idler does not experience the GVD of the ODL, it is not filtered. However, it is generated as a complementary to the amplification of the filtered signal. Therefore, the common sense dictates that it should be replicating the characteristics of the signal. In fact, this assumption might be true if the spectral phase of the pump is completely disregarded. In our case, we attribute the spectral width of the idler to the chirp of the pump pulses. This assumption is justified by simulations in [75] where they demonstrate the effect of the chirp of Pump and signal on the chirp and bandwidth of the idler.

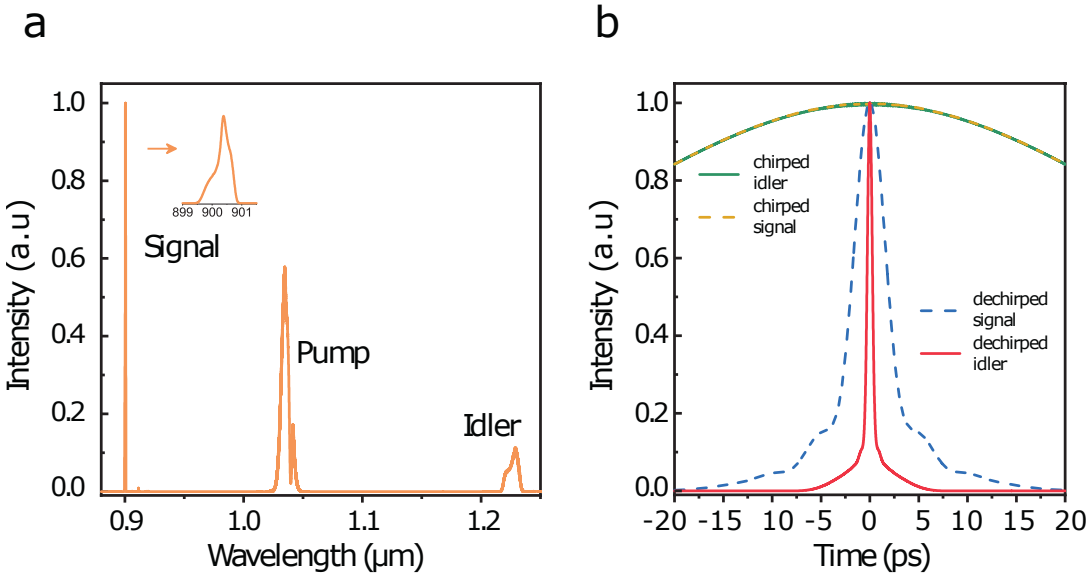

Figure 3.10: **Numerical simulations.** (a) FOPCPO spectrum (*inset: close-up on signal wave*), (b) Autocorrelation traces of signal and idler waves before and after compression.

The energy level predicted for each component is 250 nJ, corresponding to a total conversion efficiency of more than 25 %. Both signal and idler pulses exhibit a linear chirp which can be totally compensated using a grating-based compressor thus allowing them to reach their Fourier limits of 2.8 ps and 300 fs, respectively, as represented in Fig. 3.10b. Although we note a slight pedestal on the idler/signal autocorrelation (AC) traces, the system demonstrates a good intensity stability as shown by the idler's spectral evolution on 100 cavity round trips in Fig. 3.11a, where we can notice that stability is reached after less than 40 round-trips.

The spectrogram in Fig. 3.11b highlights that, for positively chirped pump pulses, the chirp of the idler and signal is positive as well. However the sign is the same, we can clearly see that the signal and idler are not chirped in the same manner. On the one hand, the chirp of the signal is mainly controlled by the SMF as it contributes mostly to its temporal stretching. On the other hand, the idler is supposed to be the phase conjugate of the signal. The spectrogram shows that clearly this is not the case. In fact, the chirp of the pump is transferred to the generated idler due to the spectro-temporal interaction of the pump and signal during the DFWM process.

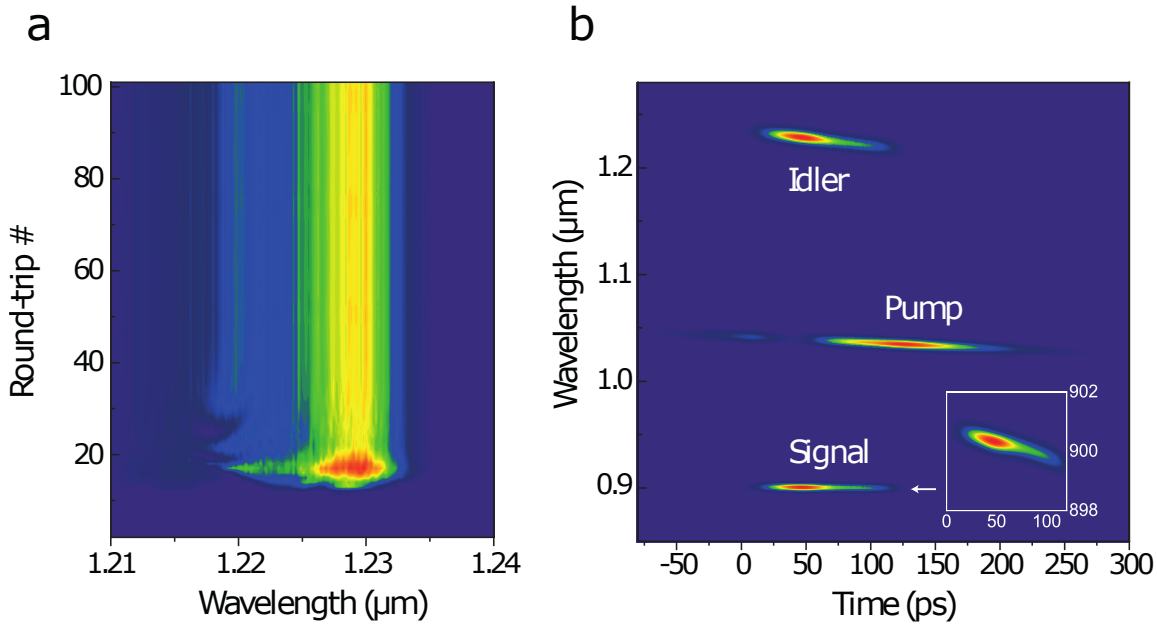

Figure 3.11: **Numerical simulations.** (a) Idler spectral evolution on 100 cavity round-trips. (b) Spectrogram at the PCF output (*inset: close-up on signal wave*).

In addition, our simulations show that the pulse energies extracted from such a system can be significantly improved either by increasing the pump energy while reducing the PCF length (as in Ref. [71]) or, more efficiently by increasing the pump pulse stretching factor, as illustrated in Fig. 3.12. Remarkably, we observe a linear increase of the idler energy when linearly increasing the energy and chirp of pump pulses and optimizing the feedback ratio. The μJ level is eventually reached when using 700 ps and 10 μJ chirped pump pulses in the FOPCPO. The spectral bandwidth remains between 8 nm and 10 nm while the dechirped pulse duration increases linearly from 300 fs to 550 fs when the pump energy is increased from 2 μJ to 10 μJ. This highlights the particular potential of FOPCPOs for energy scaling.

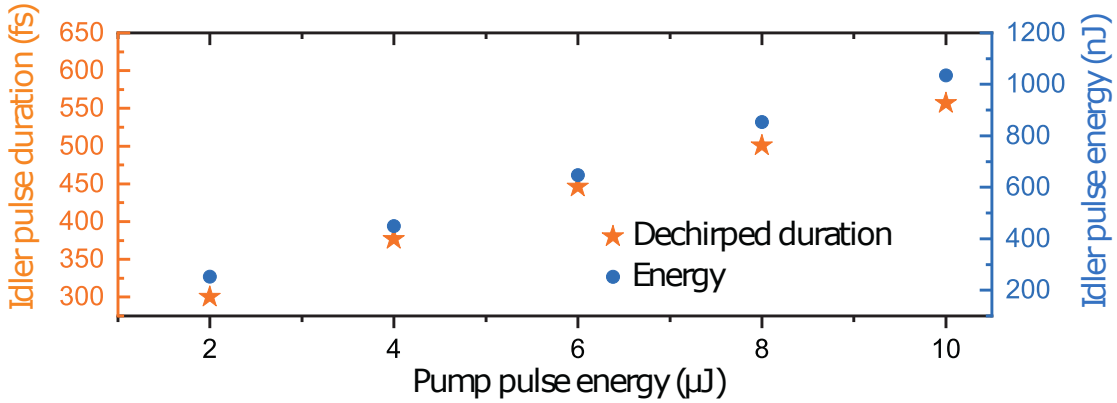

Figure 3.12: **Numerical simulations.** Dechirped idler pulse duration and energy versus pump pulse energy.

3.4 Experimental results

In a second phase and guided by these numerical results, we then implemented experimentally the FOPCPO concept using the setup presented in Fig.3.2. By coupling 2 μJ of pump energy into the PCF while optimizing the feedback within the FOPCPO cavity, our system generates idler and signal pulses with energies up to 250 nJ and 60 nJ, respectively. The difference in the energies between signal and idler is attributed to the difference in the output coupling between the two wavelengths. A typical full-field spectrum including the depleted pump at 1036 nm and the idler and signal waves at 1221 and 900 nm, respectively, is shown in Fig. 3.13a. The bandwidths of idler and signal waves are 9 and 3 nm, respectively. As already discussed in Ref. [71], the large normal dispersion in the cavity causes the resonant signal pulses to have a larger chirp than the incoming pump pulses. Therefore, only a small portion of the spectrum of the fed-back pulses which overlaps with the pump pulses is amplified. As the gain provided by FWM increases with pump power, the amplified signal and idler spectra become broader but this effect is more significant for the idler pulse propagating in the anomalous dispersion regime along the PCF.

The total measured output power from our system is ∼1 W, with 235 mW and 55 mW for the filtered idler and signal, respectively. This corresponds to a total pump depletion of ∼30 %. The AC traces of the chirped pump and idler pulses are shown in Fig. 3.13b, with AC durations of 190 ps and 100 ps, respectively. The output pulses are compressed externally using a pair of reflection gratings with 1250 lines/mm in a double-pass configuration. A typical dechirped AC trace measured for an idler energy of 100 nJ is shown in Fig.3.14a. The corresponding idler spectrum shown in the inset of Fig.3.14a extends over 10 nm from 1225 to 1235 nm. The AC trace inferred by Fourier transformation of the optical spectrum assuming a zero phase relation has a width of 900 fs for a pulse duration of 400 fs, see Fig. 3.14a. The dechirped idler pulse duration is ∼570 fs which is about 30% far from its Fourier limit value. Radio-frequency (RF) spectra were also recorded for idler and signal waves using a fast photodetector (DET08CFC, Thorlabs) and a RF spectrum analyzer (Rohde and Schwarz, 7 GHz bandwidth), as shown in Fig.3.14b, and exhibit

an excellent signal-to-noise ratio exceeding 85 dB. It is worth mentioning that the noise structures appearing at low frequencies (<1KHz, see inset) are inherent to the pump laser.

Using time-dispersion-tuning, i.e. by varying the cavity length via the ODL and thus selecting

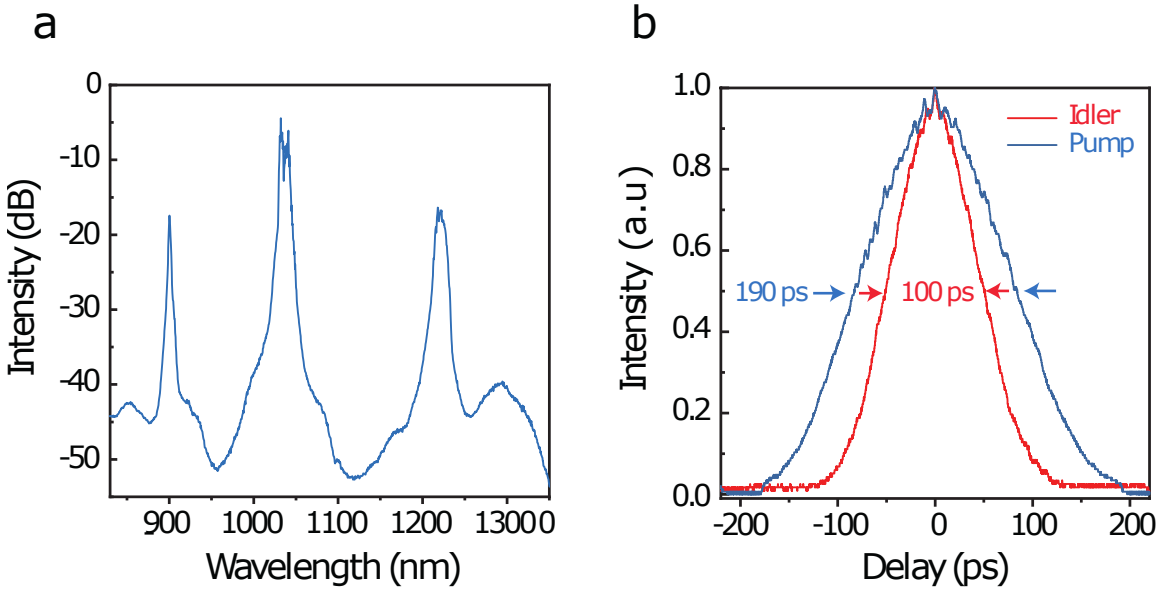

Figure 3.13: **Experiments.** (a) Typical full-field spectrum of the FOPCPO with λ_s = 900 nm and λ_i = 1220 nm. (b) Autocorrelation traces of the chirped pump pump before injection in the PCF (*blue*) and of the chirped idler pulse at the FOCPO output (*red*).

the spectral components that overlap temporally, the FOPCPO output pulses can then be widely tuned over the available parametric gain bandwidth from 850 to 930 nm for the signal and from 1170 to 1325 nm for the idler. Fig.3.15 shows part of this tunability window, where signal and idler waves can be tuned (-3 dB bandwidth) over ∼35 nm from 870 to 905 nm and over ∼60 nm from 1210 to 1270 nm, respectively, by moving the end-mirror in the ODL by ∼20 cm. As summarized in Fig.3.15, high energies ranging from 25 to 50 nJ for the signal and from 125 to more than 250 nJ for the idler are extracted from this system. We can also see that the signal spectral bandwidth remains around 3 nm when generated between 880 and 906 nm but is narrowed to less than 1 nm for shorter wavelengths.

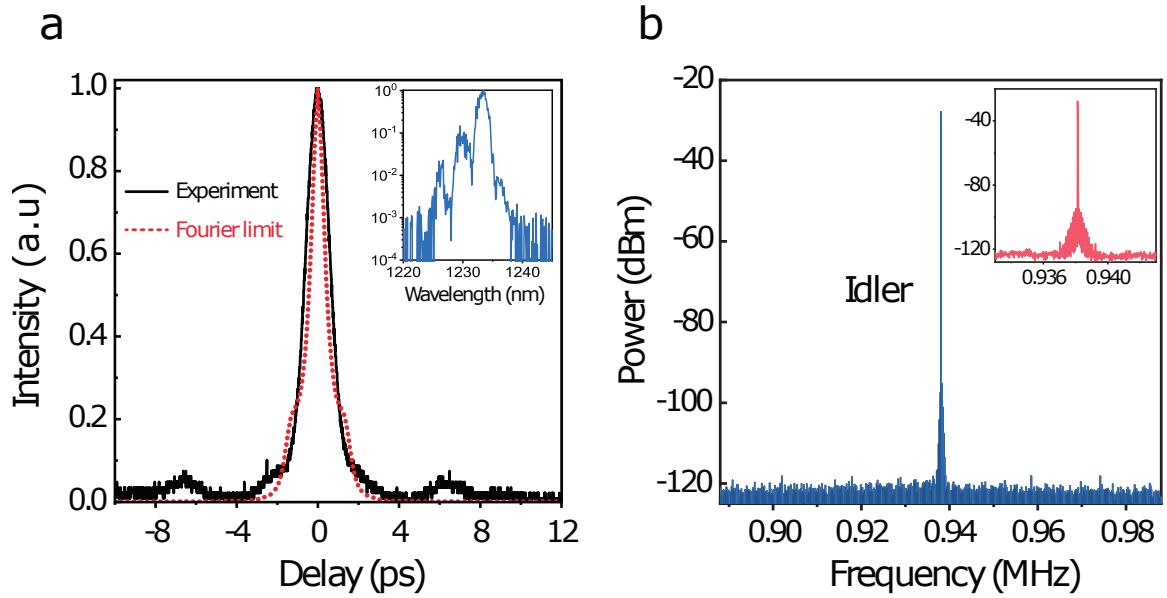

Figure 3.14: **Experiments.** (a) Compressed idler pulse (*black*) and comparison with its Fourier limit (*red*) derived from the corresponding idler spectrum (*inset*). (b) Idler RF spectrum on a 100 kHz span, with 1 Hz resolution (*Inset: 10 kHz span*).

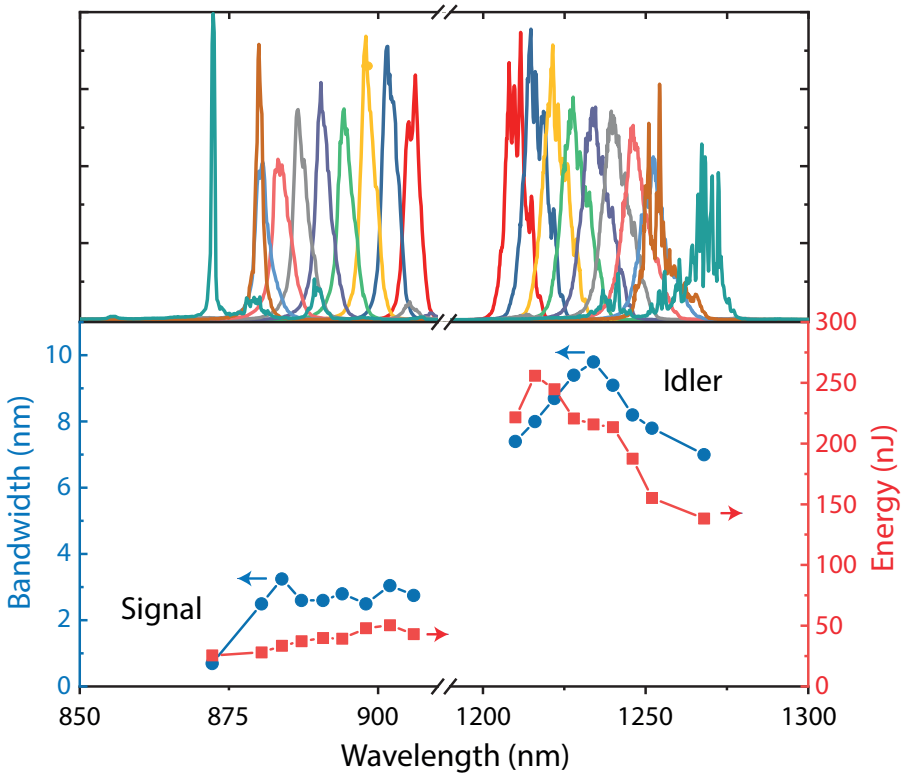

Figure 3.15: **FOPCPO tunability.** *Bottom*: Energy (*red*) and spectral bandwidth (*blue*) of signal and idler pulses at the FOPCPO output. *Top*: Corresponding optical spectra.

3.5 Conclusion

In summary, we have demonstrated the first fiber optical parametric chirped-pulse oscillator (FOPCPO) pumped in the normal dispersion regime, delivering picosecond chirped idler pulses with an energy as high as 250 nJ and a spectral bandwidth of 9 nm centered at 1220 nm along with chirped signal pulses with 50 nJ energy and a spectral bandwidth of 3 nm centered at 900 nm. Signal and idler waves can be tuned over 35 nm from 870 to 905 nm and over 60 nm from 1210 to 1270 nm, respectively. Output pulses showed excellent noise properties with a SNR exceeding 85 dB. These performances then pave the way for the use of such FOPCPO as wavelength-agile fiber sources for applications in biophotonics or spectroscopy. Considerable room is still available for improving the performances of our system, in particular increasing the chirp of the pump pulses opens the way for energy scaling beyond the microjoule barrier. Moreover, optimization of the parametric gain fiber could lead to higher efficiency.

CHAPTER 4

Spectral correlations in a fiber optical parametric oscillator

The previous Chapter was mainly focused on the upscaling of FOPOs performances through the use of an original pumping architecture based on highly-chirped pump pulses. Numerical simulations were performed to anticipate the power scaling possibilities in such a system but also revealed that rich dynamics could emerge in the parametric process generation. In this Chapter, we then choose to investigate the ultrafast shot-to-shot dynamics of a FOPO rather than to concentrate on its performances. Such a study is enabled via the use of a simple yet powerful real-time spectroscopy technique known as dispersive Fourier transform (DFT) or photonic time-stretch. The latter is based on the use of highly-dispersive optical fibers to switch the spectrum measurement in the time domain and, as such component are easily available in the C band telecom wavelength window, we built and studied the dynamics of a FOPO pumped around 1.55 μm. This Chapter is then organized as follows. We first detail the working principles of DFT and present its experimental implementation for the study of the FOPO dynamics. As DFT enables the recording of large ensembles of shot-to-shot spectra, we then introduce and compare the statistical metrics allowing to exploit such data, namely Pearson correlations and mutual information analysis. Those tools are eventually applied to the study of the spectro-temporal dynamics and correlations in our FOPO, with the aim to efficiently track energy transfers between pump and parametric waves. With potential quantum optics applications in mind, a specific attention will also be paid to the experimental parameters allowing to shape the frequency correlations in such systems.

4.1 Introduction

The complex dynamics of optical systems attracts scientists for decades and the emergence of real-time temporal and spectral measurement techniques has recently opened new opportunities by enabling in-depth characterization of ultrafast or non-repetitive events. In the temporal domain, the development of time lenses has for instance allowed the full-field characterization of partially coherent waves [76] or soliton dynamics in mode-locked lasers [77] and provided new insights in their transient dynamics. In the spectral domain, dispersive Fourier transformation (DFT) is a powerful tool for the continuous acquisition of real-time spectra on long time scales [78,79]. It indeed enabled the real-time spectral characterization of ultrafast laser systems, from unveiling their build-up dynamics [80] to probing soliton bound states [81,82]. This ability to record large ensembles of spectra then allows to use statistical metrics to describe the dynamical behaviors of light sources. Higher-order moments and Pearson correlations have for instance been used for understanding the complex processes involved in supercontinuum generation [83,84]. Spectral correlation indeed revealed the intrinsic dynamics of particular phenomena in optical systems such as modulation instability, four-wave mixing (FWM), random lasing [85–87] and can also be useful when designing FWM-based amplifiers [88]. In fiber-based sources, it has been demonstrated experimentally that spectral correlations resulting from modulation instability and FWM could be shaped through the control of the dispersion maps of liquid- or gas-filled optical fibers [89–91]. This "on-demand" tailoring of frequency correlations could be a valuable tool for building specific sources in quantum optics applications, such as biphoton, twin beams sources [90] or ultrafast frequency combs [92]. These studies however concerned "single-pass" sources and an actual shaping of frequency correlations within parametric oscillators has not been reported yet, and may prove relevant due to the wavelength flexibility of such systems, as higlighted in the previous chapter.

In this chapter, we thereby characterize the dynamics of a fiber optical parametric oscillator (FOPO) using DFT in order to identify the experimental parameters driving its spectro-temporal properties and correlations. Such dynamics of parametric sources have already attracted the attention of several research groups in the last years. On the one hand, spectro-temporal dynamics and pulse-to-pulse instabilities have been studied in bulk $\chi^{(2)}$-based OPOs, which are well-known sources of highly quantum-correlated beams [93], demonstrating that chirp rate, pump power and cavity detuning, among other parameters, strongly influence the output dynamics [94,95]. For instance, particular dynamics have then been recorded with chaotic or periodic spectro-temporal evolutions. In such $\chi^{(2)}$-based singly-resonant cavities, it has also been shown numerically that an extremely rich variety of self-organized structures can be found [96]. On the other hand, FOPOs based on degenerate four-wave mixing (DFWM) have reached enough maturity for many applications, particularly in coherent anti-Stokes Raman scattering microscopy [97,98] due to their broad tuning range, their ability to generate synchronized pulses with widely spaced frequency bands and their favorable noise properties [99]. A recent study described the build-up dynamics of

a FOPO using DFT [100], but wavelengths correlations and the parameters governing their shape have never been investigated to date. In this chapter, we then aim at unveiling the spectro-temporal dynamics and particular spectral correlations in a synchronously-pumped FOPO using an original combination of different statistical tools. This chapter is structured as follows. We first present our experimental setup comprising a FOPO and a DFT systems for recording the its dynamics. Secondly, we present the combination of statistical tools used to exploit the large ensembles of data and then use these tools to highlight specific correlation patterns but also to evidence the influence of pump intensity fluctuations on the output dynamics. In this frame, we will compare standard Pearson correlation and mutual information (MI) analysis [87, 101] for revealing the system dynamics. In addition, we will investigate the spectro-temporal booting dynamics of the system and its convergence toward a steady-state. Finally, we will highlight the specific influence of the cavity detuning on the correlation patterns, but more importantly we will demonstrate how the combination of simple statistical tools can be used to extract insightful data from large ensembles of shot-to-shot spectra. Some perspectives to this work are eventually presented in the frame of the full engineering of spectral correlations in fiber OPOs.

4.2 FOPO synchronously-pumped in the C-band: a test-bed for dynamics characterization

4.2.1 Experimental setup

The experimental setup used for tracking the real-time dynamics of a FOPO is shown in Fig. 4.1 and is based on the system developed in Ref. [102] for efficient parametric oscillation around 1.7 μm. It can be separated in three main blocks: a mode-locked fiber laser as a pump source, a fiber cavity comprising the nonlinear medium for parametric oscillation and an optical delay line (ODL) for pulses synchronization, and eventually a DFT measurement system composed of dispersive fibers, fast photodiodes and a digitizer (fast oscilloscope). Similar to the experimental setup described in the previous chapter, the working principles of those three building blocks are detailed in the next sections. An Erbium-doped fiber amplifier is used to increase the pulses peak power prior to the injection in the FOPO cavity allowing to operate the mode-locked laser at a low average power, thus ensuring its long-term stability.

4.2.2 Pump source

The laser source shown in Fig. 4.1 is a homemade passively mode-locked Erbium-doped fiber laser featuring large normal dispersion and produces highly chirped pulses [103]. This system is detailed in Fig. 4.2. The Fabry-Perot cavity is composed of a heavily Erbium-doped single mode fiber with a numerical aperture of 0.29 and a mode field diameter of the core of 4.3 µm at 1550 nm. The cavity also includes a dispersion compensation fiber with an optimised length to obtain a highly normal dispersion. The mode-locking is achieved due to the high modulation depth provided by the combination of the nonlinear polarization rotation (NPR) mechanism with

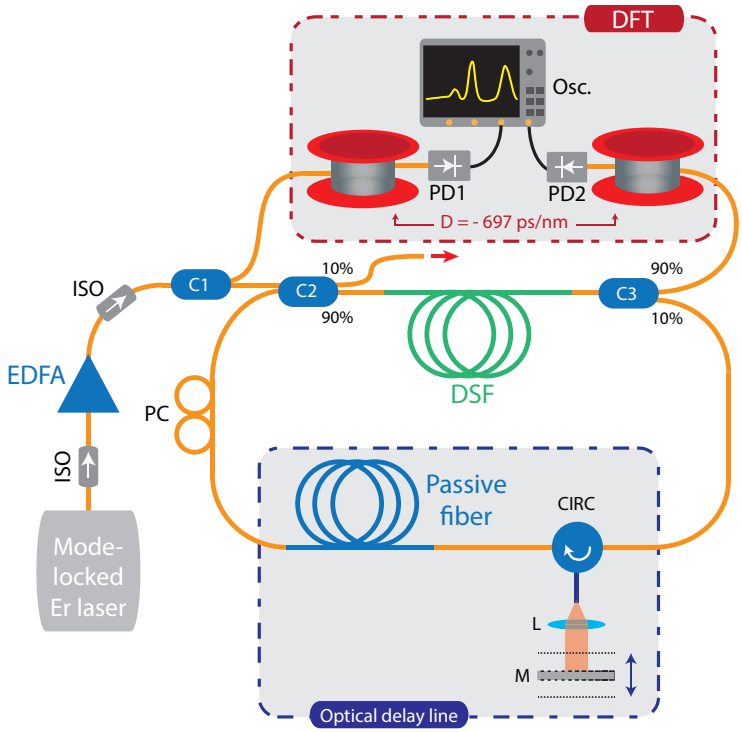

Figure 4.1: **Experimental setup for investigating the FOPO's shot-to-shot dynamics.** EDFA: Erbium-doped fiber amplifier; ISO: isolator; C: coupler; DSF: dispersion-shifted fiber; CIRC: optical circulator; PC: polarization controller; PD: photodiode; L: lens; M: mirror.

a reflective saturable absorber mirror (R-SAM). A bulk reflection grating is placed at one end of the cavity and combined with an aperture-limited lens to constitute a narrow-band spectral filter allowing to balance the pulse evolution with the dispersive propagation in the DCF and then to stabilize the mode-locking. Moreover, the grating allows for the tuning of the laser's output wavelength to generate dissipative solitons with several nanojoules of energy in the spectral range between 1549 nm and 1566 nm at a repetition rate of 6.1 MHz. In order to ensure a high stability on long terms as well as the sustainability of a single-pulse regime, the mode-locked oscillator is operated at low average power of 4.5 mW and generates chirped pulses with 28 ps average pulse duration and 2.3 nm spectral width. Fig.4.3 shows the spectrum of the generated pulses at wavelength of 1560 nm along with the corresponding auto-correlation trace. The spectrum of the generated pulses exhibits an M-shape, typical of this type of oscillator. This profile is found to be crucial for highlighting the influence of the spectral shape on the FOPO dynamics. The laser pulses are subsequently amplified up to 50 mW of average power using an EDFA, as mentionned in the previous section.

4.2.3 FOPO cavity

The FOPO cavity consists of 7.7 m of a 4 μm-core dispersion shifted fiber (DSF) acting as the gain medium for efficient DFWM, 5.4 m of HI1060 fiber and 8.5 m of UHNA4 fiber for pulse synchroni-

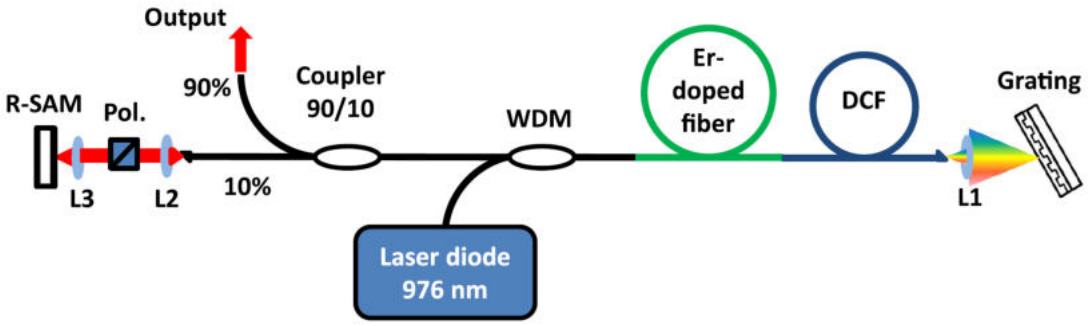

Figure 4.2: **Schematic of the homemade laser source serving as a pump for the FOPO:**WDM: 980/1550 nm multiplexer; 90/10: output coupler; DCF: dispersion-compensating fiber; L1, L2, L3:AR-coated coupling lenses; R-SAM:resonant saturable absorber mirror; Pol:polarizer. [103].

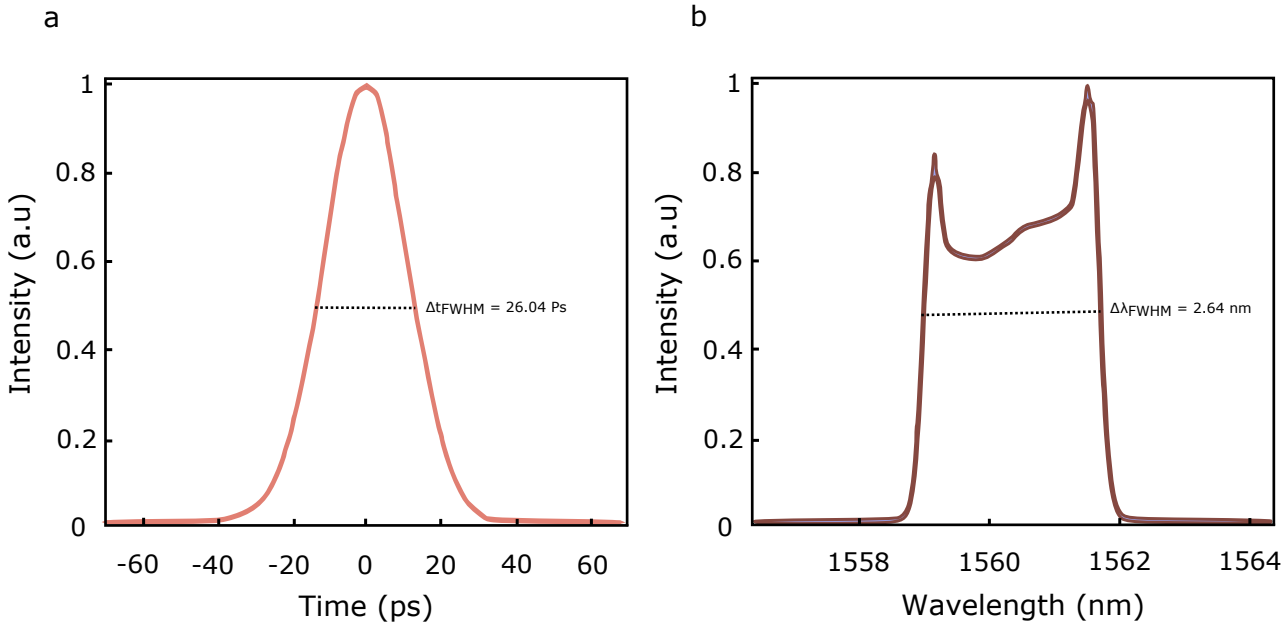

Figure 4.3: **Pump characteristics.** a) Autocorrelation trace. b) Spectrum.

sation and operation in the normal dispersion regime in order to overcome the nanojoule energy barrier around 1700 nm [102]. The FOPO's averaged-zero dispersion wavelength is estimated around 1.73 μm. The free space section of the optical delay line is used for fine adjustments of the synchronization of the oscillating pulses with fresh pump pulses. It then allows to synchronize the pump pulses either with the resonating signal or idler. In this configuration, phase-matched signal and idler can be tuned from 1340 nm to 1513 nm and 1617 nm to 1876 nm, respectively.
In order to investigate the spectro-temporal dynamics of such a cavity, the spectra at the input and output pulses need to monitored on a single-shot basis. As such measurements are inaccessible to standard optical spectrum analyzers (OSA), which provide spectra averaged over millions of pulses, a specific real-time technique, known as dispersive Fourier transformation, has to be used.

4.2.4 Dispersive Fourier transform

4.2.4.1 Theoretical bases and working principles

Dispersive Fourier transform (DFT) is based on dispersive media to perform the Fourier transform of optical signal on a single-shot basis and at high frame rates. DFT can then be used for the real-time analysis of ultrafast processes as it allows the mapping of the optical spectra of ultrafast pulses on their stretched temporal waveforms, thereby overcoming the temporal limitations of electronics-based systems (e.g. OSA). Consequently, DFT has been be widely used in ultrafast spectroscopy or in the tracking of transient events in the last decade [78, 79]. DFT is an example of the space-time duality rising from the equivalence in the mathematical expressions governing the influence of GVD on a laser pulse and paraxial beam diffraction. On the one hand, if we consider the propagation of a relatively weak laser pulse in a lossless medium with negligible nonlinearity, the NLSE given in Eq. 2.41 would only account for the effects of the dispersion on the temporal waveform of a propagating pulse. In the absence of higher order dispersion terms, the NLSE can then be expressed as follows:

$$\frac{\partial A}{\partial z} + i\frac{\beta_2}{2}\frac{\partial^2 A}{\partial T^2} = 0 \tag{4.1}$$

On the other hand, the one dimensional paraxial diffraction can be expressed with the following equation:

$$\frac{\partial A}{\partial z} + \frac{1}{i2k}\frac{\partial^2 A}{\partial x^2} = 0 \tag{4.2}$$

By comparing Eq. 4.1 and Eq. 4.2, we can see that the equation that governs pulse evolution in a dispersive medium and the one of paraxial diffraction are identical, except for the fact that the wavenumber k in Eq. 4.2 can only have positive values in contrast with β_2. This similarity gave birth to the concept of space-time duality [104, 105] which state that the observation of a phenomenon in one domain can provide a physical insight about its dual phenomenon in the other domain. Therefore, the various techniques developed in the field of Fourier optics can be employed on temporal signals for implementing powerful and innovative tools such as DFT. Fig. 4.4 illustrates this duality between paraxial diffraction and temporal dispersion. In the following, we recall the theoretical background allowing to derive the main equations governing DFT.

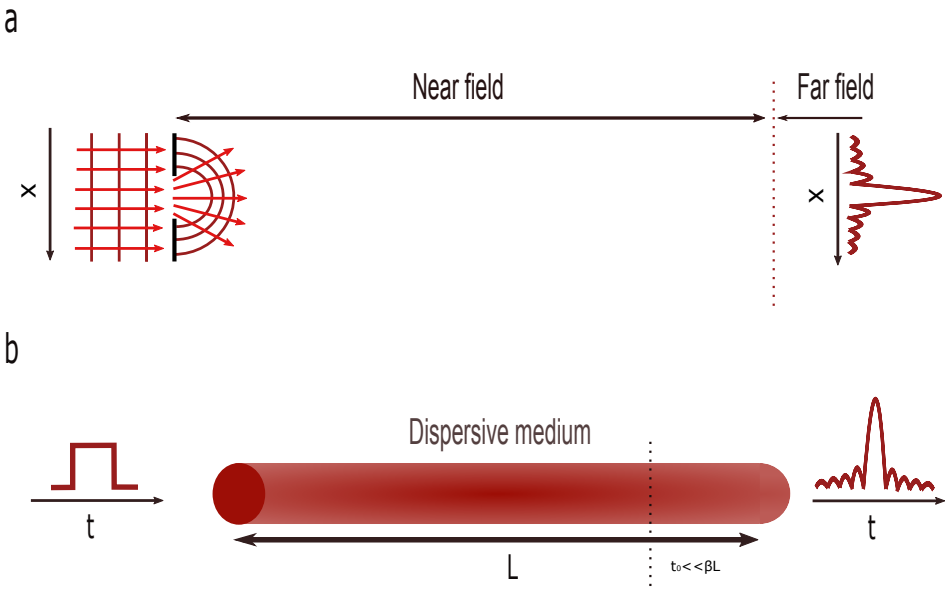

Figure 4.4: **Representation of space-time duality.** a) Paraxial diffraction. b) Temporal dispersion.

It is common knowledge that a lossless dispersive element can be considered as a linear time-invariant system (LTI) that influences the phase of the optical pulse and not its spectral amplitude [106]. The transfer function of a lossless dispersive element can be expressed as follows:

$$H(\omega) = \exp\left(-\sum_{m=0}^{\infty} \frac{\beta_m z}{(m)!}\omega^m\right) \tag{4.3}$$

Where $-\sum_{m=0}^{\infty} \frac{\beta_m z}{(m)!}\omega^m$ defines the Taylor expansion of the phase profile of the transfer function given that z is the length of the dispersive element. By only considering the second order dispersion and neglecting the effect of higher orders, the corresponding impulse response of the dispersive element is given as [107]:

$$h(t) = \sqrt{\frac{i}{2\pi\beta_2 z}} \exp\left(-\frac{it^2}{2\beta_2 z}\right) \tag{4.4}$$

In LTI systems, the output signal is the result of the convolution between the input signal and the system's impulse response in the time domain. This allows for expressing the temporal waveform of the pulse's slow-varying envelope at the output of a dispersive element in terms of its initial form at the input in the following manner:

$$A(z,t) = \int_{-\infty}^{+\infty} A(0,\tau)h(t-\tau)d\tau \tag{4.5}$$

$$= \sqrt{\frac{i}{2\pi\beta_2 z}} \exp\left(-\frac{it^2}{2\beta_2 z}\right) \int_{-\infty}^{+\infty} A(0,\tau) \exp\left(-\frac{i\tau^2}{2\beta_2 z} \exp\left(-\frac{it\tau}{\beta_2 z}\right)\right) d\tau \tag{4.6}$$

Eq. 4.6 can be approximated to the form $a\int_{-\infty}^{+\infty} f(t)\exp(iwt)dt$ if the following condition is satisfied:

$$t_0 << |2\beta_2 z| \tag{4.7}$$

This latter condition implies that the input pulse is required to be considerably narrow in the time domain, and consequently broadband in the spectral domain. In addition, the dispersive element needs to exert a strong GVD on the pulse through a sufficient distance of propagation. This condition is analogous to the far-field condition in the spatial domain (diffraction) as it leads to the so-called temporal Fraunhofer approximation. When this condition is satisfied, the temporal waveform of the laser pulse at the output of the dispersive element can be expressed as:

$$A(z,t) = \sqrt{\frac{i}{2\pi\beta_2 z}} \int_{-\infty}^{+\infty} A(0,\tau) \exp\left(-\frac{it\tau}{\beta_2 z}\right) d\tau \tag{4.8}$$

The integral is simply a scaled Fourier transform of the input pulse and represents a scaled replica of the pulse's spectrum. Therefore, propagating a broadband laser pulse through a highly dispersive medium along a sufficient distance makes the temporal waveform of the pulse to exactly mimic the shape of its spectrum. This can be easily understood since the essence of GVD is that different optical frequencies have different propagation velocities, which leads the spectral components to temporally separate along with propagation. With enough propagation, the spectral components of the pulse are then sufficiently separated so that its temporal waveform turns into a scaled replica of its spectrum. In other words, a Fourier transform is performed on the optical pulse through the exploitation of dispersion, yielding the name "dispersive Fourier transform". This process is schematically depicted in Fig. 4.5.

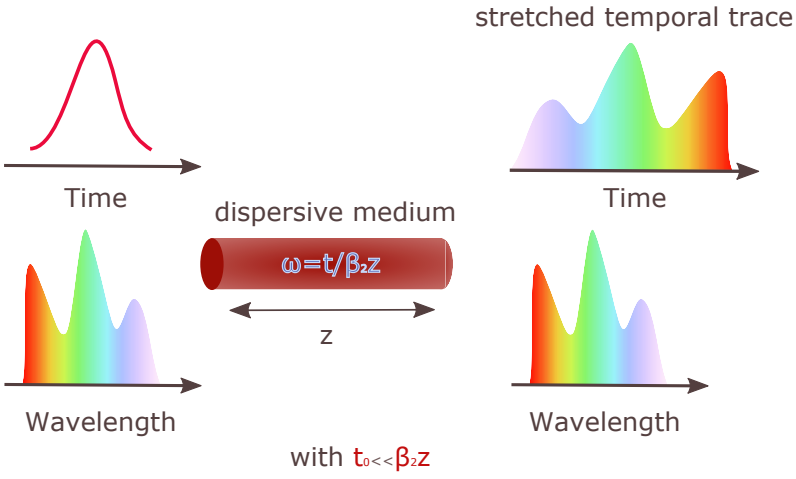

Figure 4.5: **Representation of pulse propagation through a dispersive medium.** When the equivalent of the temporal Fraunhofer approximation condition is satisfied, the optical frequencies of an optical pulse are mapped to its temporal waveform.

Eq .4.8 is obtained under the assumption that higher orders of dispersion such β_3 are negligible, and gives a linear relationship that describes the frequency-time mapping through DFT and

expressed as:

$$\Delta t = \beta_2 z \omega \tag{4.9}$$

The frequency-time mapping still exists when high orders of dispersion are considered as long as the condition for the temporal Fraunhofer approximation is satisfied. However, the relationship that links the optical frequencies to the temporal waveform in this case is not linear anymore. For this reason, a generalized mapping relationship that takes into account dispersion of higher orders has to be derived. A slightly different approach then needs to be taken in order to extract a general frequency-time mapping relationship as well as to define the spectral resolution of this mapping. For this purpose, we can start by expressing the electric field of the input pulse in the frequency domain as follows:

$$A(0,\omega) = |A(0,\omega)| \exp(i\theta(\omega)) \tag{4.10}$$

where $|A(0,\omega)|$represent the spectral amplitude of the pulse while $\theta(\omega)$ represents its spectral phase. In the case of transform-limited pulses, the derivative of the spectral phase is null and, in the frequency domain, the electric field of the output pulse can be expressed as the multiplication of the input pulse expressed in Eq.4.10 with the transfer function given in Eq.4.3. Therefore, the temporal envelope of the pulse at the output of the dispersive element can be found in the following manner:

$$A(z,t) = \frac{1}{2\pi} \int_{-\infty}^{+\infty} |A(0,\omega)| \exp\left(i\left(\theta(\omega) - \left(\sum_{m=0}^{\infty} \frac{\beta_m z}{(m)!}\omega^m\right) + \omega t\right)\right) d\omega \tag{4.11}$$

The term including the zeroth order of dispersion does not have an influence on the chirp of the propagating pulse since it is independent of frequency. This allows to remove it from the equation. In addition, we set a new temporal reference that moves at the group velocity of the pulse through the change of variable $T = t - \beta_1 z$. This way, we obtain the following formula:

$$A(z,t) = \frac{1}{2\pi} \int_{-\infty}^{+\infty} |A(0,\omega)| \exp\left(i\left(\theta(\omega) - \left(\sum_{m=2}^{\infty} \frac{\beta_m z}{(m)!}\omega^m\right) + \omega T\right)\right) d\omega \tag{4.12}$$

The phase term in Eq. 4.12 oscillates rapidly when the GVD and length of the dispersive element are sufficient (Fraunhofer condition). This oscillation results in the vanishing of the integral at all the values of ω except for a small range around a stationary frequency ω_s according to the stationary phase approximation. The stationary frequency is found by setting the derivative of the phase term in Eq. 4.12 with $\omega = \omega_s$ to zero, and as the input pulse is unchirped, the differentiation results in the following expressions:

$$\frac{d}{d\omega}\left(\omega T - \sum_{m=2}^{\infty} \frac{\beta_m z}{(m)!}\omega^m\right)|_{\omega=\omega_s} = 0 \tag{4.13}$$

$$T = \sum_{m=2}^{\infty} \frac{\beta_m z}{(m-1)!}\omega^{m-1} \tag{4.14}$$

Eq. 4.13 defines the general frequency-time mapping relationship when considering all the dispersion terms [108]. If we consider only the β_2 term in Eq. 4.14, we of course end-up with the same mapping relationship as in Eq.4.9.
Based on the stationary phase approximation, the temporal waveform of the output pulse can eventually be approximated by the following expression:

$$A(z,t) = \frac{|A(0,\omega)|}{b} \exp\left(i\left(\theta(\omega) - \left(\sum_{m=2}^{\infty} \frac{\beta_m z}{(m)!}\omega^m\right) + \omega T - \frac{\pi}{4}\right)\right) \tag{4.15}$$

with:

$$b = \sqrt{2\pi \left|\sum_{m=2}^{\infty} \frac{\beta_m z}{(m-1)!}\omega^{m-1}\right|} \tag{4.16}$$

In Eq. 4.15, we can clearly see that the output pulse's temporal waveform at the instant T_s is the mapping of its optical frequency ω_s according to the relation stated in Eq. 4.14.

4.2.4.2 Resolution of DFT

The resolution of the mapping process depends on the spectral width round the stationary frequency on which the integral in Eq. 4.12 does not vanish. By ignoring dispersive effects above the second order, this spectral region is defined by the first two zeroes of the real part of the phase term in Eq.4.12 around the stationary frequency ω_s. The resolution is then expressed as [109]:

$$\delta\omega = 2\sqrt{\frac{\pi}{\beta_2 z}} \tag{4.17}$$

In terms of wavelength, it is then given by:

$$\delta\lambda = \lambda\sqrt{\frac{2}{Dcz}} \tag{4.18}$$

where D is the dispersion parameter, c is the speed of light while z is the length of the dispersive element. Eq. 4.18 shows that the spectral resolution of DFT limits the frequency-time mapping to pulses with spectral widths above the resolution limit. This issue can be overcome either by increasing the GVD, increasing the length of the dispersive element or through temporal focusing by using a time lens along with the dispersive element. In addition, Eq.4.18 also shows that the stronger is the dispersion, the better is the resolution. This result is physically obvious since more GVD means more separation between the spectral components. However, a temporal overlap can occur between consecutive pulses if the value of GVD is too high. For this reason, the repetition rate of the laser source on which DFT is performed needs to be taken into account in order to ensure an optimal spectral resolution without any temporal aliasing.

The spectral resolution of DFT can also be limited by need for an electronic system comprising a photodiode and an oscilloscope (digitizer) in order to record the stretched pulse. For instance, the

photodiode converts the optical signal into an analog electric signal and the temporal resolution of this process is limited by the photodiode's rise time, which is directly linked to its bandwidth. Analog to digital conversion is later performed on the analog electric signal at the oscilloscope level to enable the storage of a digital version of the electric signal. The sampling frequency of the analog-to-digital conversion limits the resolution as well since it defines the temporal spacing between the samples. By considering all the limiting factors, the spectral resolution of DFT measurements is then defined as the worst of the dispersive element, photodiode and oscilloscope resolutions. It is consequently expressed as:

$$\delta\lambda = max(\delta\lambda_{dis}, \delta\lambda_{ph}, \delta\lambda_{osc}) \tag{4.19}$$

Where $\delta\lambda_{dis}$ represents the resolution limit due to the dispersive element, $\delta\lambda_{ph}$ is the resolution limit due to the photodetector bandwidth while $\delta\lambda_{osc}$ is the resolution limit due to the sampling rate of the oscilloscope.

In our experiments, real-time spectra are recorded at the FOPO's input and output using DFT where time-stretching is obtained using spools of telecommunication-grade fibers with a dispersion of -697 ps.nm^{-1} at 1550 nm. The output port of coupler C2 (see Fig. 4.1) is used for monitoring the pump pulse duration via an autocorrelator while the pump and FOPO spectra are respectively acquired in the time domain at the 10% port of coupler C1 and the 90% port of coupler C3 using two high-speed 25 GHz photodiodes (New Focus, Inc.) and a real-time 33 GHz oscilloscope (Keysight, Inc.). Taking into account the limited bandwidth of the photodetector and more importantly the magnitude of the time-stretching process, our system has a spectral resolution of 0.16 nm. The reliability of DFT measurements is ensured by comparing consecutive real-time spectra with standard measurements based on an optical spectrum analyzer (OSA, Anritsu), as shown in Fig. 4.7, where we achieve a satisfying matching of the spectral components over the full emission range of the FOPO. Note that in the following all the spectra are normalized to the pump intensity. Moreover, Fig.4.6 shows the recorded spectra displayed in 3-D form in order to better highlight the capacity of DFT to capture the spectral evolution of laser pulses in time.

In the next section, we then detail how specific statistical tools can be used to extract relevant information based on the remarkable ensembles of shot-to-shot spectra acquired using DFT. Particularly, we will focus on two specific metrics, namely Pearson correlation and mutual information analysis, to investigate the FOPO dynamics.

4.3 Statistical tools

Real-time measurement of shot-to-shot spectra enables the extraction of statistical matrices providing insights on the physical processes based on large sets of experimental data. Wavelength intensity correlations are for instance very useful to reveal energy transfers or dependency between different spectral components [83, 84]. On the one hand, correlation is a measure of the

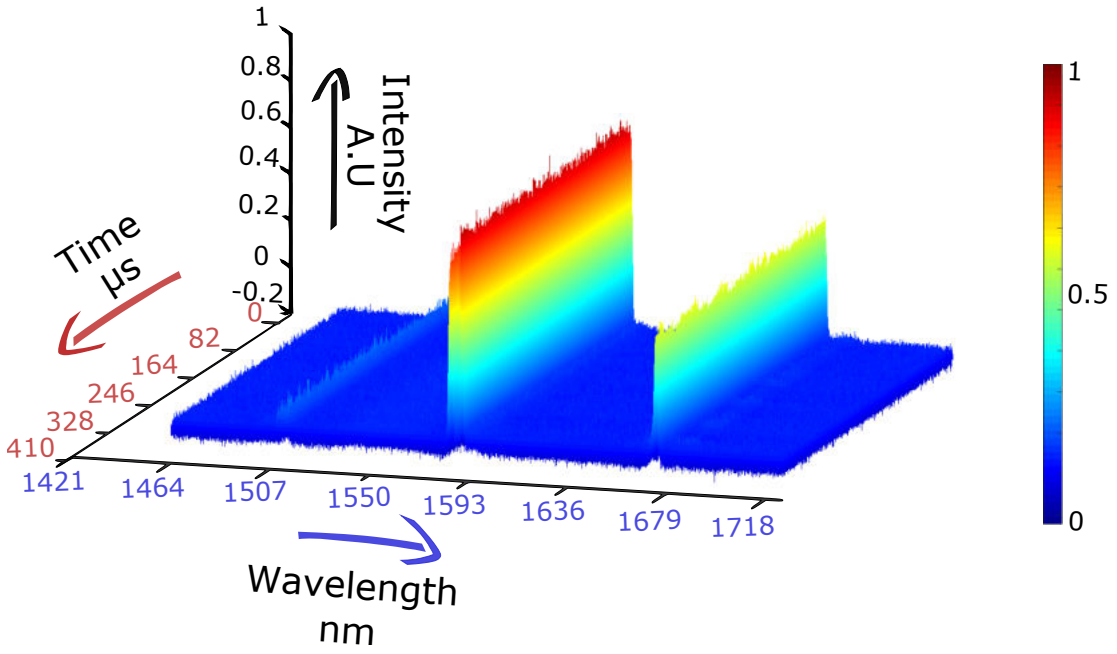

Figure 4.6: **Real-time spectra** recorded using DFT and plotted as a function of time.

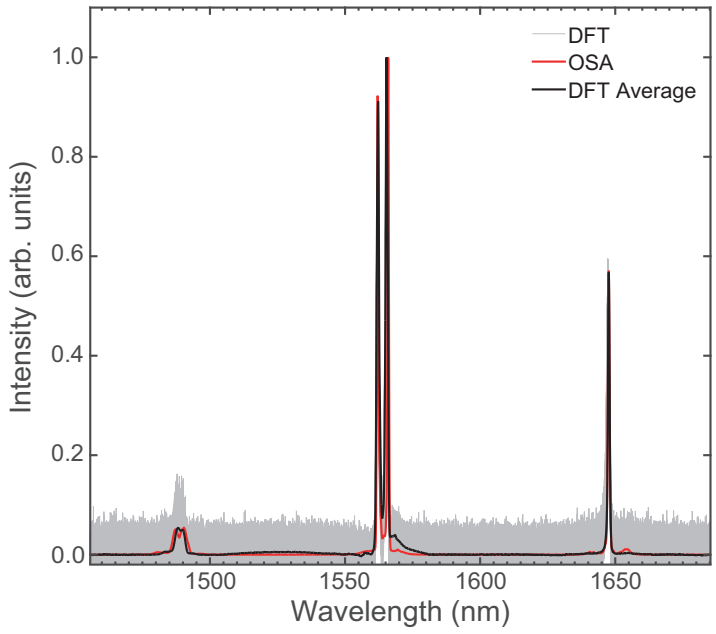

Figure 4.7: **Real-time spectra** recorded using DFT (*grey*), their average spectrum (*black*) and comparison with an OSA measurement (*red*).

linear dependency between two random variables and provides information about the strength and nature - either positive or negative - of this linear relationship. On the other hand, mutual information (MI) analysis is a similar statistical tool quantifying the general dependency between two random variables but might provide a better physical insight as it is a quantitative expression of the information obtained on one variable throughout the observation of another [110]. It then provides a measure of the dependency - linear or nonlinear - between two random variables. MI is for now underused in nonlinear optics, but has recently been proved insightful in the study of spectral dynamics in fibre laser systems [87, 111]. We then aim here at generalizing its use and evaluating its relevance when studying correlations in nonlinear optical systems. In a discrete domain, the mutual information between variables X and Y is defined as:

$$\sum_{y\in Y}\sum_{x\in X} P_{XY}(x,y) log\left(\frac{P_{XY}(x,y)}{P_X(x)P_Y(y)}\right) \tag{4.20}$$

where $P_{XY}(x,y)$, $P_X(x)$ and $P_Y(y)$ are the joint probability mass function and marginal probability mass functions of X and Y, respectively. The estimation of these probabilistic functions from a limited statistical base is a well-known problem in statistics [112]. Among the available solutions, we use histogram estimation as it is the simplest with the least computational load. As for Pearson correlation, it is commonly defined as:

$$Corr(X,Y) = \frac{Cov(X,Y)}{\sigma_X \sigma_Y} \tag{4.21}$$

with:

$$\sum_{y\in Y}\sum_{x\in X} xy[P_{XY}(x,y) - P_X(x)P_Y(y)] \tag{4.22}$$

where Cov is the co-variance of the random variables X and Y while σ_X and σ_Y are their corresponding standard deviations respectively. Eq. 4.22 can be described as the weighted sum of the product of the two random variables with the weights being a linear measure of their dependency. Therefore, the co-variance can have a value of zero even when the random variables are stochastically dependent. A direct comparison can be performed between co-variance and mutual information when Eq.4.20 is rearranged in the following manner:

$$\sum_{y\in Y}\sum_{x\in X} P_{XY}(x,y) log\left(\frac{P_{XY}(x,y)}{P_X(x)P_Y(y)}\right) = \sum_{y\in Y}\sum_{x\in X} P_{XY}(x,y)[log(P_{XY}(x,y)) - log(P_X(x)P_Y(y))] \tag{4.23}$$

Similar to the co-variance, Eq. 4.23 allows to describe mutual information as a weighted sum of the joint probability mass function of the two random variables with the weights in this case being a logarithmic measure of distance from statistical independence. The similarity between Eq.4.22 and Eq.4.23 is evident. Therefore, MI dependency maps would then share the same patterns with standard Pearson wavelength correlation maps (as in Refs [83–86]). Yet, the fact that the weights in Eq.4.23 are a logarithmic measure of distance from statistical independence makes mutual information a general measure of dependency, linear or nonlinear. Moreover, the *log*

function makes MI maps more versatile as they can visually capture the significance of larger changes. Unfortunately, this feature comes with the drawback of MI having only positive values and consequently it does not provide any information regarding the sign of the dependency between the variables.

In order to compensate for this drawback, we propose here to combine MI with the standard least square (LSQ) method to determine the derivative of the best linear fit between the two random variables in the spectral regions with considerable mutual information. The sign of this derivative indeed identifies the nature of the dependency, either positive or negative. Another reason for using linear regression is imposed by our specific system: the DFWM process corresponds to the annihilation of two pump photons while simultaneously generating idler and signal photons, making the generated photons pair correlated in the quantum sense. The conversion efficiency of this process relates to the number of converted pump photons with respect to the total number of pump photons available at a given wavelength and thereby to the probability of generation of a signal/idler photons pair in spontaneous emission. The joint spectral density function of this probability is approximated by the product of the phase matching and the energy conservation functions [89,91]. The phase matching of the DFWM process in an optical fiber directly depends on the pump power and wavelength. Consequently, for a specific pump wavelength λ_p, the conversion efficiency only depends on the pump power and any change in it would induce a change in the FWM gain and subsequently in the conversion efficiency [32]. If λ_{p_0}, λ_{s_0} and λ_{i_0} are the central wavelengths for pump, signal and idler, respectively, and Λ_{p_0}, Λ_{s_0} and Λ_{i_0} their respective spectral widths, let's consider the following variables: $\lambda_p \in [\lambda_{p_0} - \Lambda_{p_0}/2, \lambda_{p_0} + \Lambda_{p_0}/2]$ spanning the pump wavelengths, $\lambda_s \in [\lambda_{s_0} - \Lambda_{s_0}/2, \lambda_{s_0} + \Lambda_{s_0}/2]$ spanning the signal wavelengths and $\lambda_i \in [\lambda_{i_0} - \Lambda_{i_0}/2, \lambda_{i_0} + \Lambda_{i_0}/2]$ spanning the idler wavelengths. For DFWM with chirped pump pulses, every component within the pump spectrum contributes to the idler (and signal) at a specific wavelength with a certain proportion dictated by the phase mismatch and can be written as follows:

$$I(\lambda_i, n) = \int_{\lambda_{p_0} - \Lambda_{p_0}/2}^{\lambda_{p_0} + \Lambda_{p_0}/2} a(\lambda_p, \lambda_i, n) I(\lambda_p, n) d\lambda_p \tag{4.24}$$

$$= \int_{\lambda_{p_0} - \Lambda_{p_0}/2}^{\lambda_{p_0} + \Lambda_{p_0}/2} I(\lambda_i, \lambda_p, n) d\lambda_p \tag{4.25}$$

where $I(\lambda_i, n)$ and $I(\lambda_p, n)$ are the idler and pump spectral intensities and n $\in \mathbb{Z}^{(+)}$ is the pulse number. $a(\lambda_p, \lambda_i, n)$ is the pump-to-idler conversion efficiency for pulse n and $I(\lambda_i, \lambda_p, n)$ is the contribution of pump at λ_p to idler at λ_i for pulse n. In a discrete environment, it then writes:

$$I(\lambda_i, n) = \sum_{\lambda_p = \lambda_{p_0} - \Lambda_{p_0}/2}^{\lambda_{p_0} + \Lambda_{p_0}/2} a(\lambda_p, \lambda_i, n) I(\lambda_p, n) \tag{4.26}$$

$$= \sum_{\lambda_p = \lambda_{p_0} - \Lambda_{p_0}/2}^{\lambda_{p_0} + \Lambda_{p_0}/2} I(\lambda_i, \lambda_p, n) \tag{4.27}$$

For pulse $n+1$, the spectral intensity at wavelength λ_p changes to $I(\lambda_p, n+1)$. This intensity fluctuation is denoted $\Delta I_{\lambda_p} = I(\lambda_p, n+1) - I(\lambda_p, n)$. The change in the idler due to the change of the pump writes as:

$$\Delta I_{\lambda_i} = I(\lambda_i, \lambda_p, n+1) - I(\lambda_i, \lambda_p, n) \tag{4.28}$$

The pump intensity fluctuation affects the phase mismatch and thereby modifies the conversion efficiency to $a(\lambda_p, \lambda_i, n+1)$ with

$$\Delta a = a(\lambda_p, \lambda_i, n+1) - a(\lambda_p, \lambda_i, n) \tag{4.29}$$

and then

$$\begin{aligned} I(\lambda_i, \lambda_p, n+1) &= a(\lambda_p, \lambda_i, n+1) I(\lambda_p, n+1) \\ &= (a(\lambda_p, \lambda_i, n) + \Delta a)(I(\lambda_p, n) + \Delta I_{\lambda_p}) \\ &= a(\lambda_p, \lambda_i, n) I(\lambda_p, n) + a(\lambda_p, \lambda_i, n) \Delta I_{\lambda_p} \\ &\quad + \Delta a I(\lambda_p, n) + \Delta a \Delta I_{\lambda_p} \end{aligned} \tag{4.30}$$

We assume here the pump fluctuations to be small compared to the mean spectral intensity and the subsequent variation in the conversion efficiency to be small compared to its mean value as well. We can therefore write:

$$\begin{aligned} I(\lambda_i, \lambda_p, n+1) &\approx a(\lambda_p, \lambda_i, n) I(\lambda_p, n) \\ &\quad + a(\lambda_p, \lambda_i, n) \Delta I_{\lambda_p} + \Delta a I(\lambda_p, n) \end{aligned} \tag{4.31}$$

$$\approx a(\lambda_p, \lambda_i, n) I(\lambda_p, n+1) + \Delta a I(\lambda_p, n) \tag{4.32}$$

and

$$\Delta I_{\lambda_i} \approx a(\lambda_p, \lambda_i, n) \Delta I_{\lambda_p} + \Delta a I(\lambda_p, n) \tag{4.33}$$

$$\Delta I_{\lambda_i} / \Delta I_{\lambda_p} \approx a(\lambda_p, \lambda_i, n) + (\Delta a / \Delta I_{\lambda_p}) I(\lambda_p, n) \tag{4.34}$$

From a statistical point of view, we can then use a linear regression between λ_p and λ_i in order to isolate the effect of the pump on the idler, which is represented by $I(\lambda_i, \lambda_p, n)$ so that:

$$I(\lambda_i, \lambda_p, n) = A I(\lambda_p, n) + B \tag{4.35}$$

with the coefficients A and B being estimated by means of a regression between pump at wavelength λ_p and idler at wavelength λ_i.

$$\Delta I_{\lambda_i} / \Delta I_{\lambda_p} = A \tag{4.36}$$

and as a result:

$$A = a(\lambda_p, \lambda_i, n) + (\Delta a / \Delta I_{\lambda_p}) I(\lambda_p, n) \tag{4.37}$$

By using the standard LSQ method to obtain the best fit with the minimal error for a first order

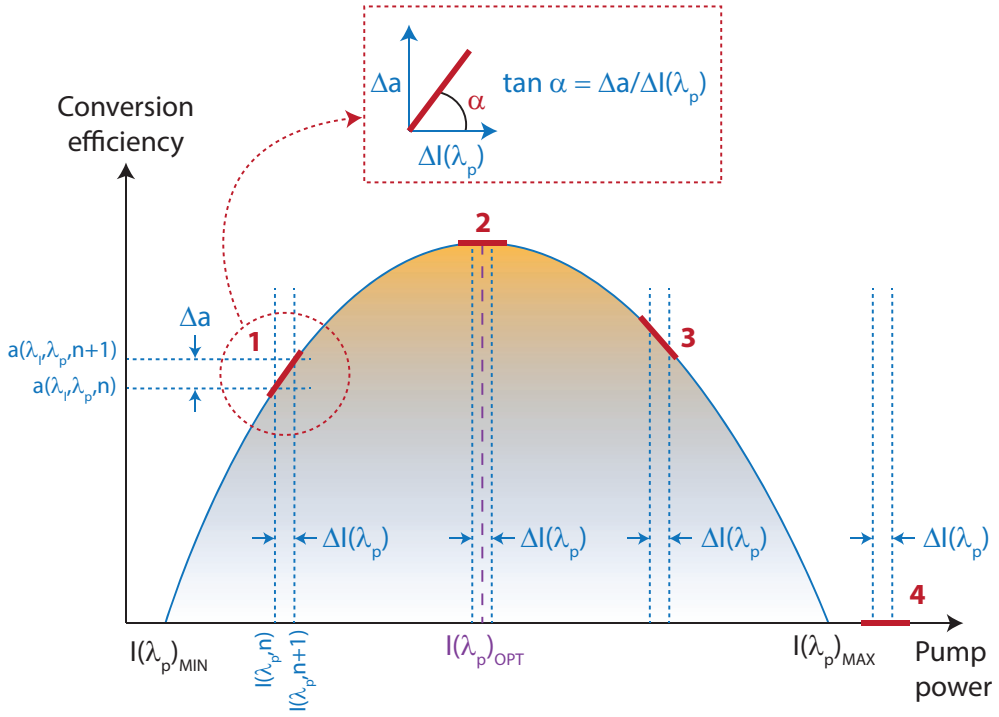

Figure 4.8: **Illustration of the effect of small changes in pump power at a specific wavelength on the conversion efficiency.** The slope, denoted α and represented in red, can be null either at maximum conversion efficiency ("2") or without any conversion at all ("4").

polynomial, we can then estimate $\Delta I_{\lambda_i}/\Delta I_{\lambda_p}$ which represents the change in the idler due to the fluctuations in the spectral intensity of the pump at wavelength λ_p, as shown in Fig. 4.8. It then directly relates to the stability of the system. As a result, the derivative of the linear fit between the idler at wavelength λ_i and the pump at wavelength λ_p has a physical significance as it relates to the change of the conversion efficiency. It then directly quantifies the phase mismatch in addition to identifying the nature of the dependency between the two wavelengths. In the following, we then use this approach to plot comprehensive maps combining mutual information analysis and least square regression in order to study the full spectral dependency throughout the FOPO spectrum both in the steady state and build-up regimes. The combination between MI and linear regression is done by calculating the coefficient of proportionality A using a regression while MI determines its trust level and acts as a validation mask. Then, we obtain a map only displaying the coefficient A where the dependency between wavelengths is significant. Similarly to standard Pearson correlation maps [88], those maps actually allow for understanding and characterizing of the parametric gain distribution and will be referred to as MI-LSQ maps in the following. In Fig. 4.9, we shows a flowchart depicting the process leading to the synthesis of these maps. The process starts with the acquisition of the DFT traces corresponding to the

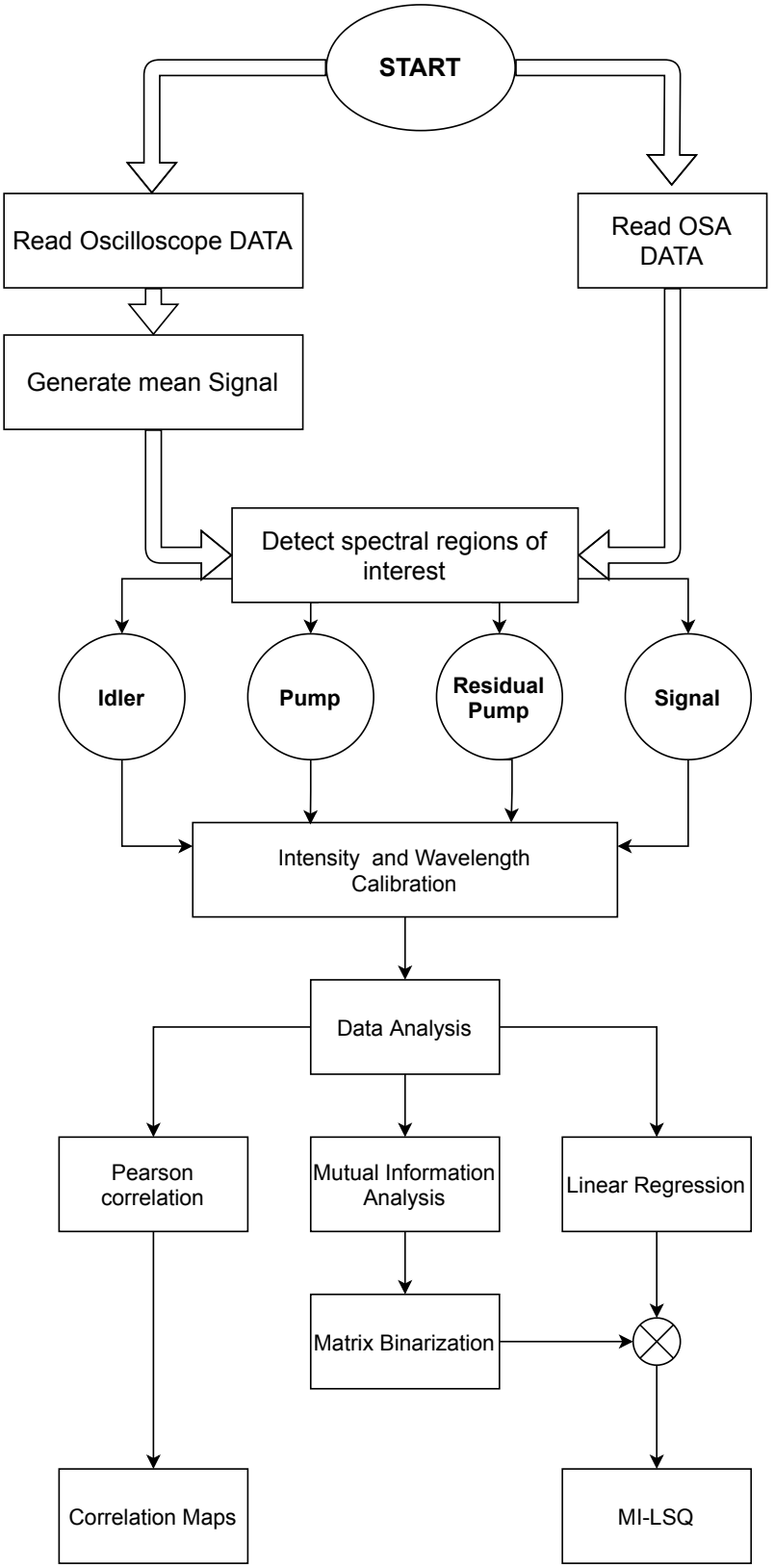

Figure 4.9: **Flowchart** describing the process used to generate correlation and MI-LSQ maps.

shot-to-shot measurements of the input and output spectra of the FOPO. The latter has three widely spaced spectral components representing the pump, signal and idler. Since the GVD of the DCF used for temporal stretching is known at $\lambda = 1550$ nm, the analytical expression defining the frequency-time mapping would not provide a precise wavelength axis for the DFT measurements as precise knowledge of GVD as a function of wavelength is missing. Therefore, the spectrum obtained using a standard OSA is used as a reference for wavelength calibration where the spectral bands containing residual pump, signal and idler are extracted from the mean of DFT traces as well as from the OSA trace. Afterwards, a cross-correlation is performed on the idler in the DFT measurement with the idler on the OSA trace in order to find the optimal time-wavelength relationship on this specific spectral band. The same process is repeated for pump, residual pump and signal. The intensity of the DFT measurements also needs to be calibrated since the losses in the DCF and the gain of photodiode are also wavelength-dependent. In this case, the OSA trace also served as a reference. The calibrated blocks of data are later used for statistical analysis using mutual information analysis and linear regression as well as Pearson correlation for comparison. For a given idler wavelength λ_i, we have a vector containing the variations of the spectral intensity of the idler at wavelength i as a function of time. Mutual information is then calculated between the vectors at idler and signal wavelengths and a matrix with values of mutual information is constructed. Using an Otsu thresholding algorithm, the matrix values are set to ones and zeroes in order to identify the signal/idler pairs having significant mutual information. The slope of the best fitting line between these pairs is calculated using linear regression (coefficient A) and an MI-LSQ map between signal and idler is thereby constructed. The signal and idler vectors are also used to create correlation maps based on Pearson correlation in a straightforward manner where a correlation value is calculated between every signal/idler pair. This process is applied to generate maps between pump, idler, signal and residual pump. The physical interpretation of these maps is detailed in the up-coming section.

4.4 Results and discussion

4.4.1 Steady state dynamics

4.4.1.1 Influence of small intensity spectral fluctuations

The FOPO is pumped at a wavelength of 1563.5 nm with pulses featuring 28.5 ps duration, 3.12 nm spectral bandwidth and 50 mW average power. Pumping the FOPO in these conditions led to an efficient energy transfer from the pump towards the idler and signal, an efficiency that is indicated by the pump depletion shown in Fig.4.10. It clearly appears that the pump depletion is much stronger in the central region of the M-shaped spectrum where the relative pump depletion exceeds 50% for most of the wavelengths while it is below 10% in the side peaks (vertical dotted lines). This already provides an indication about the wavelength-dependent conversion efficiency. For further insight, the spectra of $\sim$2000 consecutive pulses were recorded, which corresponds to a temporal window of approximately 328 μs. The coefficient A is estimated as an average

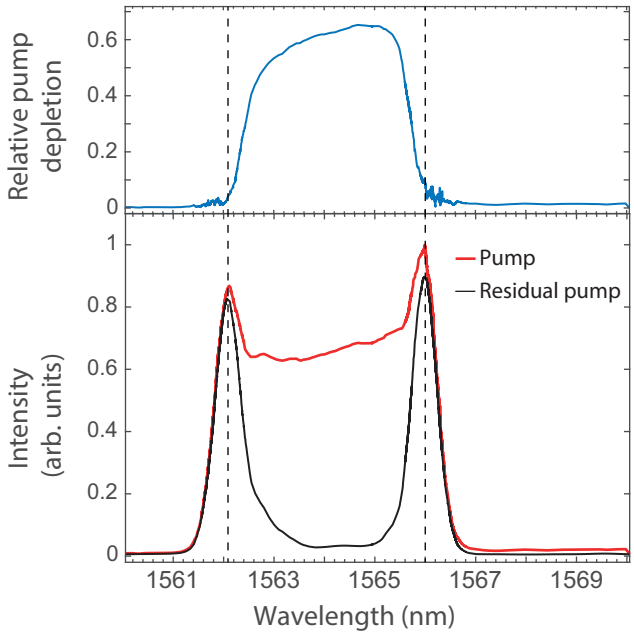

Figure 4.10: **Pump depletion.** Average pump and residual pump spectra (*bottom*) and calculated relative pump depletion (*top*).

over the whole time frame between the spectral regions of interest. Consequently, pump/idler, pump/signal and signal/idler MI-LSQ maps are generated.

Pump/idler

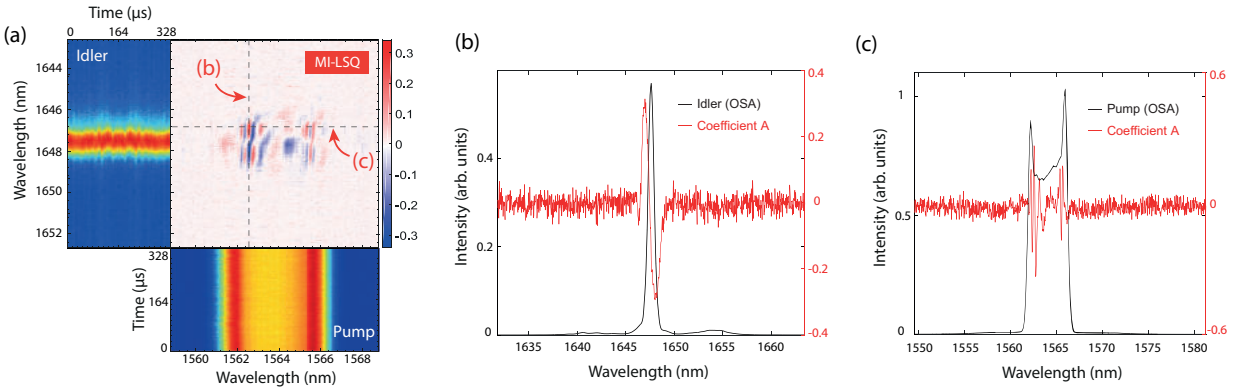

Figure 4.11: (a) **MI-LSQ map** recorded on ∼2000 consecutive shot-to-shot spectra between pump and idler waves. The color-bar denotes the coefficient of proportionality A (red: proportional, blue: anti-proportional). (b) and (c): extraction of line profiles from the dotted lines on (a).

The resulting MI-LSQ map between the idler and pump waves is shown in Fig. 4.11a. We observe a set of thin vertical stripes in the spectral regions where the two peaks of the M-shaped pump

spectrum are localized, from 1561.5 nm to 1563 nm and from 1565.5 to 1566.5 nm, respectively, as detailed in Fig. 4.11c. These patterns extend throughout the whole idler spectrum from 1646.7 nm to 1649.7 nm, which means that each pump component contributes to several or all idler wavelengths, each with a specific proportion as dictated by the phase matching conditions. The vertical stripes switch their values between positive (red) and negative (blue) showing that the spectral fluctuations of the pump at a specific wavelength in the region of the peaks of the M-shaped spectrum have different effects on the conversion efficiency for each spectral component of the idler. These stripes also switch values with respect to the horizontal axis, indicating that the fluctuations on the different spectral components of the pump affect the conversion efficiency differently for a specific idler wavelength: a pump increase reduces the phase mismatch for certain wavelengths while it increases it for others. In addition, as the phase matching conditions are different for the idler spectral components, this implies that the best possible conversion efficiency is achieved through the optimal compromise in the phase mismatch. We can also see in Fig. 4.11b that the vertical stripes change of sign around the wavelength of 1647.7 nm, which corresponds to the peak center of the idler. As previously illustrated in Fig. 4.8, the derivative of the conversion efficiency has indeed a minimal absolute value near its maximum (or when the conversion is non-existent). This indicates that the pump spectral fluctuations have minimal effects on the conversion efficiency at the idler' peak wavelength and that the conversion efficiency for this wavelength is maximal.

As stated earlier, the coefficient A in the MI-LSQ maps is estimated as an average over the total time frame which allows not to take time into account. From a statistical point of view, the time variable can be ignored when the statistical parameters of the system under study do not vary with time. Therefore, in order to verify the stationarity of our system, the total time window corresponding to ∼2000 consecutive shot-to-shot spectra was divided into 3 consecutive time slices where each contains around 660 consecutive pulses. For each time slice, a MI-LSQ map between pump and idler is generated, as shown on Fig. 4.12. The generated maps show the same pattern and are in fact almost identical except for minimal variation due to unavoidable measurement errors. This result validates the assumption that our system is stable and stationary.

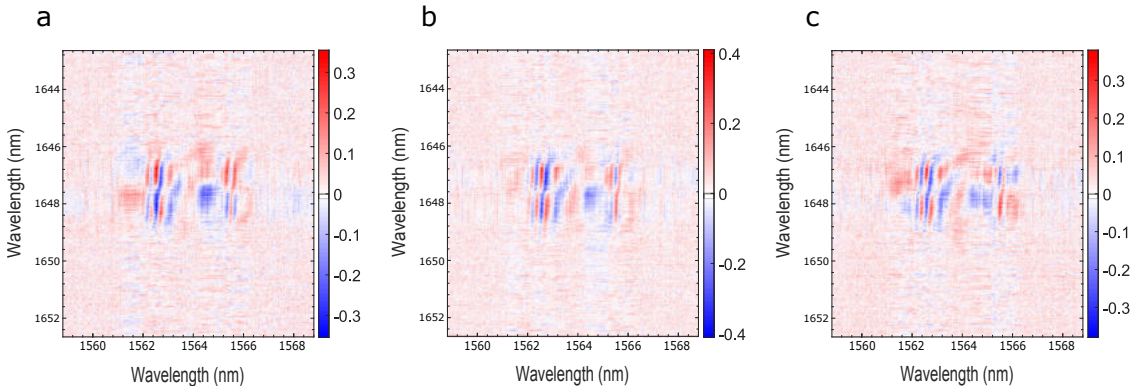

Figure 4.12: **MI-LSQ maps** recorded on ∼660 consecutive shot-to-shot spectra between pump and idler waves: (a) first time slice. (b) second time slice (c) third time slice.

Pump/signal

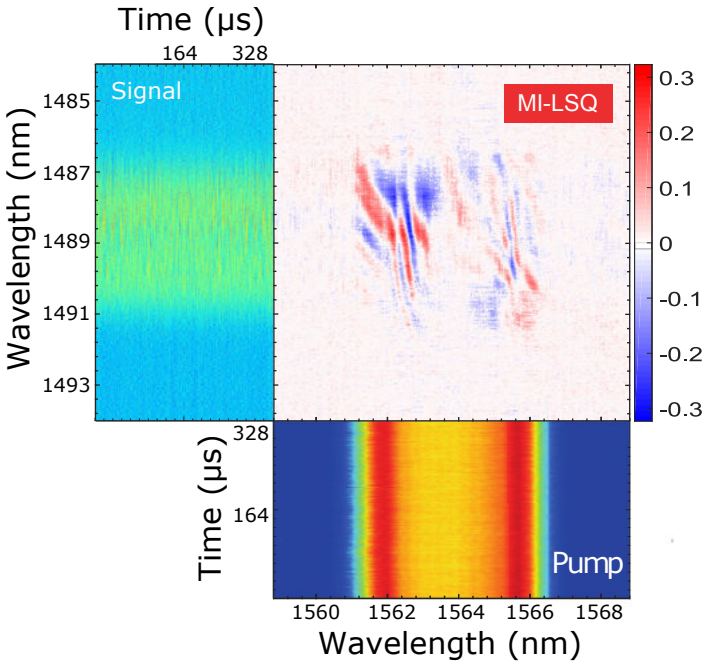

Figure 4.13: **MI-LSQ map** between pump and signal waves.

The MI-LSQ map between the signal and pump waves is shown in Fig.4.13. The patterns on this map are similar to those on the previous map between pump and idler. This is due to the fact that the creation of a new idler photon axiomatically requires the creation of a signal photon for energy conservation. We can still see a set of quasi-vertical stripes in the same spectral regions as with the idler/pump map starting from 1561.5 nm to 1563 nm and from 1565.5 nm to 1566.5 nm with respect to the horizontal axis. We can also see that the fluctuations in the pump from 1563 nm to 1565.5 nm do not have any apparent influence on the conversion efficiency for most of the signal spectrum. The existing difference between the signal/pump and idler/pump maps can be explained in the following manner: the energy conservation imposes that when two pump photons are involved in the creation of a signal photon, an idler photon is created symmetrically to the signal photon with respect to the pump in the spectral domain. However, the symmetry holds only on a single wavelength basis as one idler wavelength can be symmetrical with two signal wavelengths when two pump wavelengths are involved. Therefore, the total contribution of all pump frequencies to signal and idler is not necessarily symmetrical as it depends on the distribution of frequencies of both the pump and resonating waves in time. Otherwise, the signal and idler should have at least the same spectral shape and their respective maps should exhibit the same exact features.

Signal/idler

We now consider the MI-LSQ map between signal and idler shown in Fig. 4.14. Based on energy

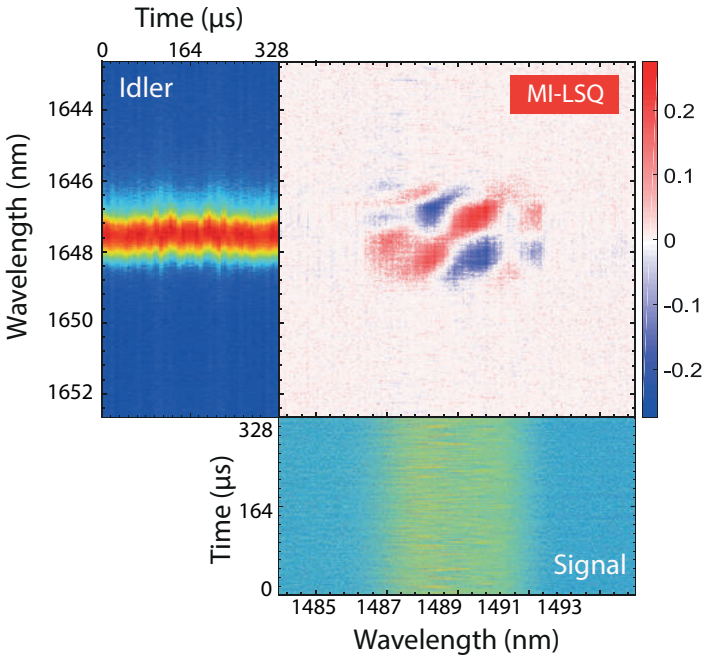

Figure 4.14: **MI-LSQ map** between idler and signal waves.

conservation in DFWM in the specific case of chirped pump pulses (see e.g. Ref. [88]), an idler-signal pair at frequencies ω_i and ω_s respectively, can be generated only through the annihilation of two pump photons at a specific frequency ω_p where $\omega_i + \omega_s = 2\omega_p$. If we consider ω_s to be increasing linearly with respect to the dummy variable x:

$$\omega_s(x) = \omega_{s_0} + \frac{\partial \omega_s}{\partial x} x \tag{4.38}$$

with ω_{s_0} the lowest signal frequency component corresponding to:

$$\omega_{s_0} = \frac{2\pi c}{\lambda_{s_0} + \Lambda_{s_0}/2} \tag{4.39}$$

The energy conservation condition still holds for w_p only if:

$$\omega_i(x) = \omega_{i_0} - \frac{\partial \omega_s}{\partial x} x \tag{4.40}$$

with

$$\omega_{i_0} = \frac{2\pi c}{\lambda_{i_0} - \Lambda_{i_0}/2} \tag{4.41}$$

This leads to:

$$\frac{\omega_i - \omega_{i_0}}{\omega_s - \omega_{s_0}} = -1 \tag{4.42}$$

This indicates that if a change in the pump at frequency ω_p induced a change in the whole signal and idler spectra, the MI-LSQ map would exhibit a "proportionality" line with an inclination of

$-45°$. Also, if the same thing occurs due to intensity fluctuations at a different pump frequency, it would result in a parallel line to the one we already have from pump at frequency ω_p [88]. In terms of wavelength, λ_i can then be written as a function of λ_p and λ_s as:

$$\lambda_i = \frac{\lambda_p^2}{2(2\lambda_s - \lambda_p)} + \frac{\lambda_p}{2} \tag{4.43}$$

For a fixed λ_p, plotting λ_i as a function of λ_s then produces a quasi-linear curve with an inclination of $-50.6°$, which does not intersect with curves generated from different pump wavelengths. This explains the localized red pattern on the diagonal of the map from which the pump spectral region responsible for the creation of the idler/signal pairs can be extracted (see Fig.4.14). This region spans from ∼1563 nm to ∼1565 nm, corresponding to the wavelengths between the two peaks of the M-shaped spectrum. On the other hand, the blue patterns representing negative values on the signal/idler map are merely the effect of the modulation of the gain window of the signal and idler due to the pump intensity fluctuations, and it can not be otherwise since the existence of an idler photon is conditional for the existence of a signal photon and vice-versa.
We have then been able to visualize the effect of pump fluctuations on the conversion efficiency on a single wavelength basis as our method allowed for the generation of spectral maps with specific patterns directly related to the conversion efficiency. MI-LSQ maps thereby proved insightful regarding the system performance as they allow to track the energy flow from pump waves toward parametric waves.

4.4.1.2 Influence of large intensity spectral fluctuations

In order to further investigate the effect of pump fluctuations on the conversion efficiency, the intensity level of the pump laser fluctuations was increased by inducing mechanical vibrations on the laser breadboard. Based on the DFT measurements, the mean spectrum of the pump did not change but its mean standard deviation increased by 4.3%. The pump wave instabilities then led the idler and signal to exhibit considerable fluctuations as shown in Fig. 4.15b. In this case, the conversion efficiency oscillates between a high level with a strong pump depletion accompanied by a growth of signal and idler waves (state 2), and a low level with a mostly undepleted pump (state 1). An inverse proportionality relationship between the residual pump and idler can easily be deduced from the MI-LSQ map on Fig. 4.15a as the coefficient of proportionality A is purely negative (blue region). In order to investigate the origin of the violent fluctuations at the level of the idler, the MI-LSQ map between pump and idler is generated and shown in Fig. 4.16a. This map presents the same pattern compared to the stable pump case shown in the previous section, in contrast with the correlation map obtained using the standard Pearson correlation in Fig. 4.16b, which exhibits a very poor contrast. MI-LSQ maps then prove superior to standard Pearson correlation maps for highlighting such fluctuations. In Fig. 4.16a, we can still see localized modulations near the two peaks of the pump spectrum while the value of coefficient A is much smaller in the central region. Strikingly, the value of coefficient A has increased by a factor of ∼66 from a maximal absolute value of 0.3 (see Fig. 4.11a) to 20, indicating that the idler's pump-

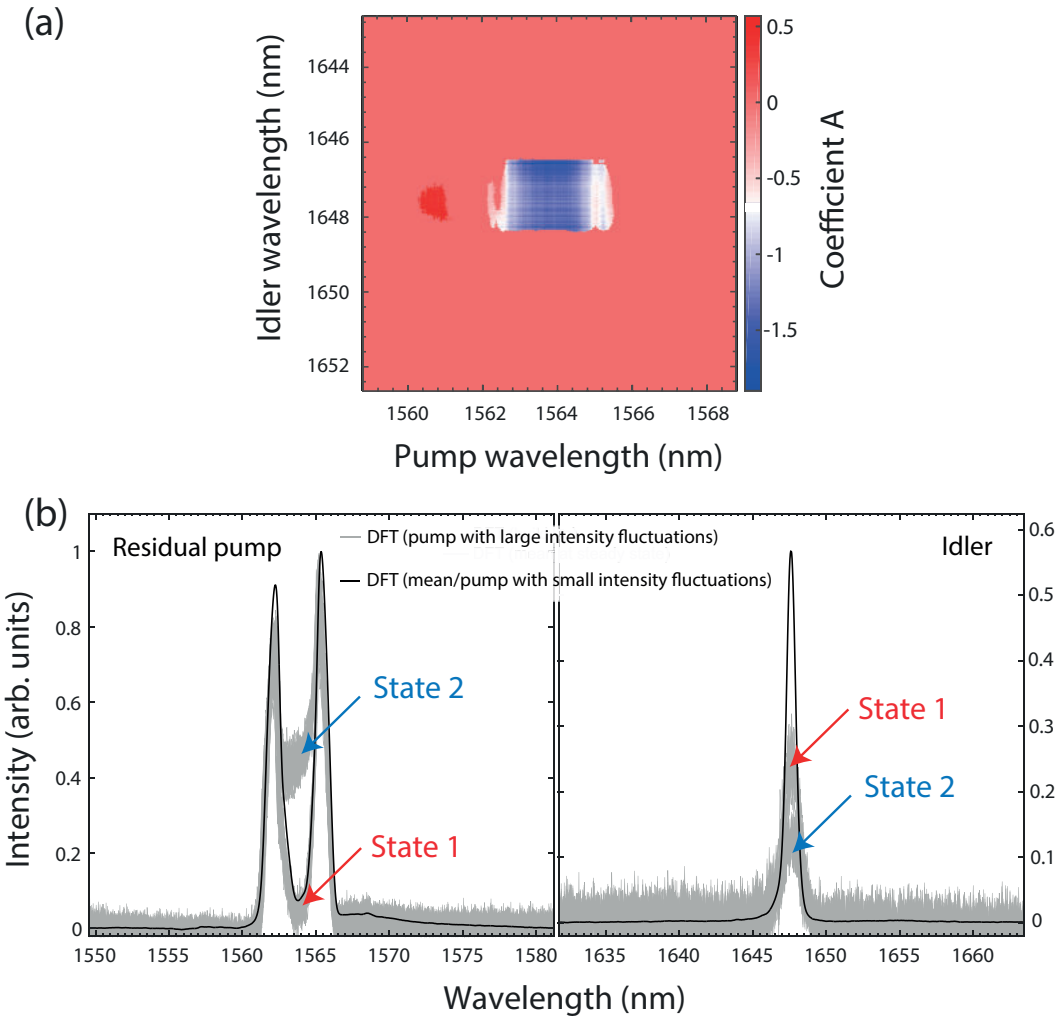

Figure 4.15: **Influence of large intensity fluctuations.** (a) Pump versus idler MI-LSQ map recorded on ∼2000 consecutive shot-to-shot spectra with a fluctuating pump, (b) Consecutive spectra for the residual pump and idler components compared with the spectra obtained with a stabler pump.

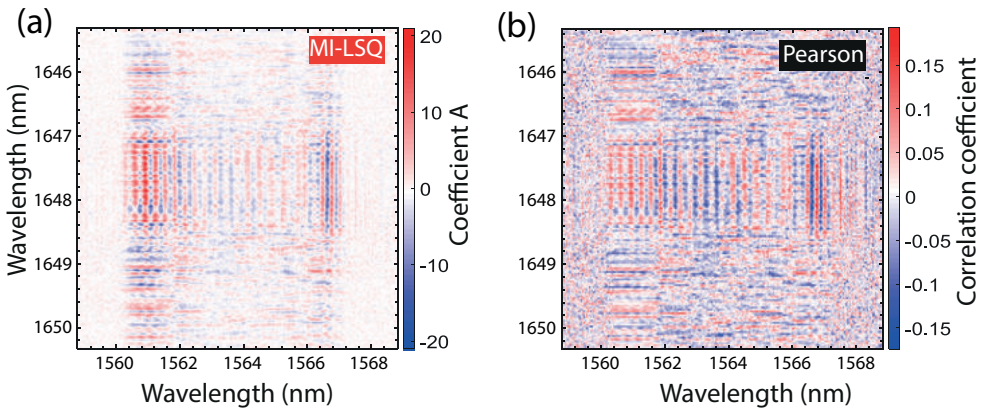

Figure 4.16: **MI-LSQ/Pearson comparison.** Pump versus idler MI-LSQ and standard Pearson correlation maps for a pump exhibiting large spectral intensity fluctuations. (a) MI-LSQ map, (b) standard Pearson correlation map.

induced fluctuations are up to 20 times greater than those of the pump itself. Fig. 4.16 also shows that the two side-peaks of the pump spectrum are mostly responsible for the violent idler and signal fluctuations. The idler and signal waves would then exhibit much weaker fluctuations and thereby be more immune to pump-induced noises if these peaks were somehow filtered out, as they have negligible contribution to the DFWM process. The change of conversion efficiency with respect to the pump power depicted in Fig. 4.8 explains this behavior, as the increase of the pump fluctuations in the spectral range where the conversion is maximal does not have a substantial effect on the conversion efficiency, and does not cause fluctuations in the generated idler and signal (region "2" in Fig. 4.8). On the contrary, in regions "1" and "3", the greater the pump fluctuations, the greater the idler and signal fluctuations. In fact, if the pump intensity fluctuations exceed a given level, their effect on the idler and signal is amplified.
This study then evidences that the FOPO can tolerate pump instabilities (i.e. parametric waves fluctuations would be much smaller than the pump ones) until a certain limit where the signal and idler fluctuations would become much stronger and give rise to particular dynamics such as the two-states evolution mentioned previously. MI-LSQ maps then remarkably allowed to highlight this phenomenon.

4.4.2 Spectro-temporal evolution & build-up regime

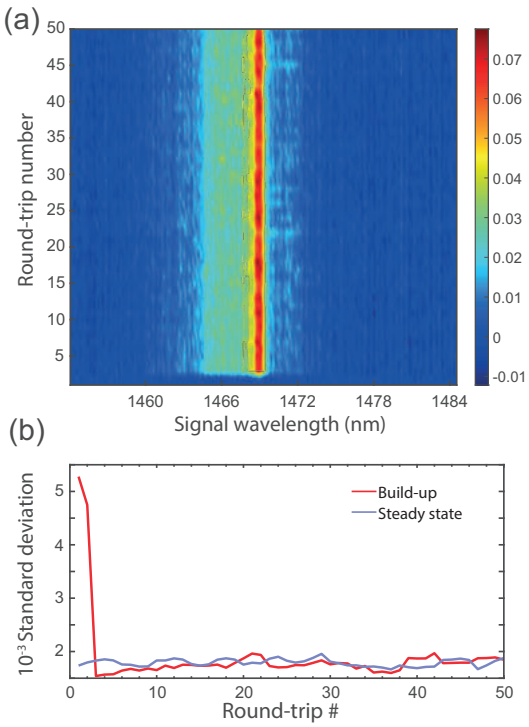

Figure 4.17: **Build-up regime.** (a) Pulse-to-pulse evolution of the FOPO's build-up. Only the first 50 shots are displayed, over a total of 10^5. (b) Moving standard deviation of the signal wave intensity in the build-up and steady-state regimes.

We then studied the FOPO build-up dynamics by inserting an acousto-optic modulator (AOM,

Fiber-Q, G&H inc.) prior to the FOPO cavity, then allowing to synchronize in time the arrival of the first pump pulse with DFT measurements. In order to operate the AOM in optimal conditions, the pump laser is tuned to a central wavelength of 1560 nm. Using a mechanical chopper to modulate the pump beam and a 50/50 coupling ratio, a comparable study has recently shown that the steady-state is reached after approximately 2000 round-trips [100]. Here, we differentiate from this study as we use a much faster modulation - the AOM has a rise time of 35 ns - in order to prevent any extra transient dynamics. In addition, an appropriate coupling is also set to quickly reach stability. This latter parameter has indeed a considerable influence on the build-up dynamics as shown in Ref. [75]. Contrary to Ref. [100], we then observe that a signal wave is almost instantaneously generated, as shown in Fig. 4.17a where the steady-state seems to be reached in the second round-trip. For the sake of clarity, only 50 consecutive shots are displayed but a total of 10^5 spectra have actually been recorded. This result is also more consistent with previous numerical studies that indeed demonstrated that idler and signal waves were stabilized after only a few round-trips [97, 102, 113]. In order to further prove that the steady-state is reached, we computed the moving standard deviation over the recorded data and compared it with the steady-state case, as shown in Fig. 4.17b. Here, the moving window contained 4 pulses. We then see that after few round-trips (less than 10), the standard deviation remains relatively stable with values similar to those in a well-established steady-state. In both cases, small-scale fluctuations are attributed to the effect of pump-induced instabilities on the conversion efficiency.

4.4.3 Influence of time-dispersion tuning

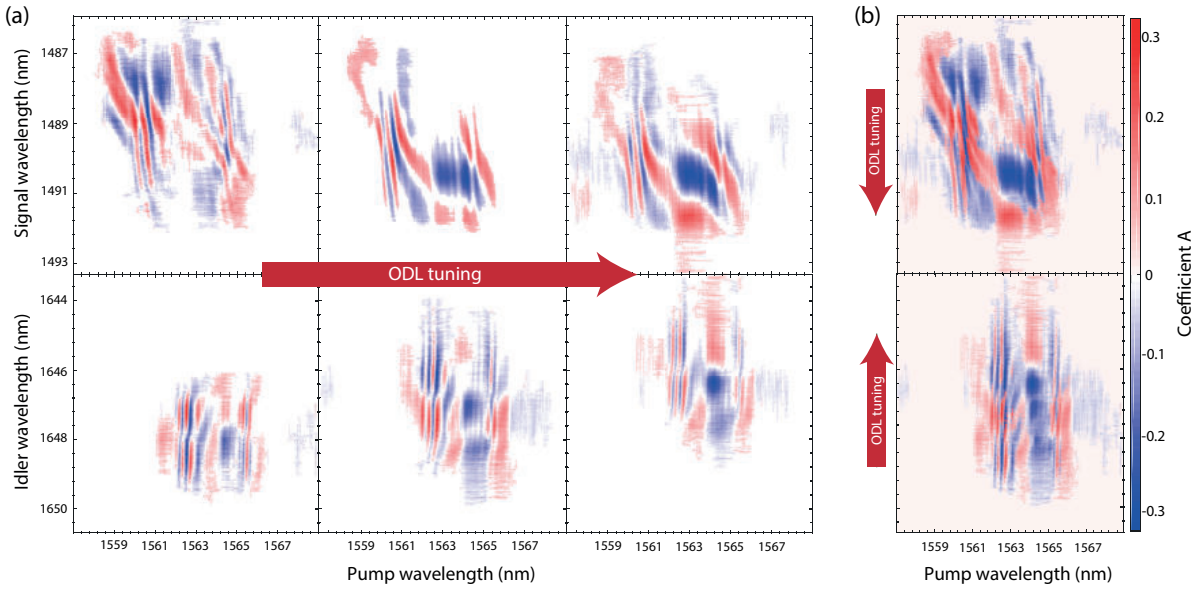

Figure 4.18: **Influence of tuning on the correlations.** MI-LSQ maps between pump and signal waves (*top*) and pump and idler (*bottom*) waves. (a) Maps recorded while varying the length of the optical delay line (ODL): initial length (*left*), ODL shortened by 50 μm (*center*), ODL shortened by 100 μm (*right*). (b) Synthesised maps superimposing the maps with different ODL lengths.

In this last section, the mirror in the free-space part of the optical delay line (ODL) is displaced in order to change the phase matching conditions and therefore to tune the idler and signal central wavelengths. Dispersion (GVD) in the passive fiber indeed stretches the resonating signal and idler while the ODL length defines which portion of it is temporally synchronized with fresh pump pulses. Such a tuning of the FOPO output wavelengths is referred to as time-dispersion tuning [102], and allows a broad tunability. We then recorded the MI-LSQ maps between idler and pump waves while tuning the ODL, as shown in Fig. 4.18a.
These figures show that the further we reduce the length of the ODL, the higher is the coefficient A in the spectral region between 1562.5 nm and 1565 nm, with respect to the horizontal axis. The increase of the proportionality coefficient implies a reduction in the conversion efficiency, which is consistent with the attenuation of the idler's peak. On the other hand, we can also see in Fig. 4.18b that the map between pump and signal waves based on their corresponding maps at different ODL lengths shows a continuous pattern that displaces vertically while tuning. As the coefficients on these maps relate physically to the conversion efficiency in the present conditions of the system, changes in ODL dispersion and length thereby allow for a certain shaping of the MI-LSQ maps by selecting vertically the width and center of the region of the map to appear. Such a technique could then now be optimized for selecting the correlated wavelengths of interest and then prove useful in the frame of tailoring correlations for specific applications.

4.5 Conclusion

In this chapter, we used an original combination of statistical tools to investigate the dynamics of a normal dispersion picosecond fiber optical parametric oscillator using dispersive Fourier transform. Our method does not only allow to track the energy transfers from pump to signal/idler pairs, but also to visually quantify the state of this energy conversion on a single wavelength basis. The outcomes of this dynamics study are then manifolds:

(*i*) The combination of mutual information (MI) analysis with least square (LSQ) regression is very efficient to extract relevant information on the dynamics of a FOPO, and proves superior to standard Pearson correlations for revealing its specific dynamics.

(*ii*) The increase of pump intensity fluctuations above a certain level results in particular unstable output dynamics, as pump fluctuations can be amplified up to 20 times when converted to the idler wave.

(*iii*) The FOPO actually reaches the steady-state in the first few round-trips.

(*iv*) The spectral correlations can be shaped to a certain extent by varying the phase matching conditions of the oscillator, a feature that could prove useful for specific quantum optics applications.

We then believe that this approach combining MI and LSQ could now be routinely used to explore specific spectro-temporal dynamics but also that this kind of measurements could be

complementary to other tools such as temporal statistics [114], to further comprehend and control the intrinsic dynamics of ultrafast optical systems.

CHAPTER 5

Acousto-optically driven ultrafast optical imaging

In the previous chapter, the shot-to-shot dynamics of a FOPO were recorded using dispersive Fourier transform, which allows for the capture of large ensembles of spectra. DFT is thereby particularly adapted to efficiently characterize the behavior of such optical systems with MHz repetition rates and to track their dynamics on the ns timescale. As a consequence, DFT has also been used as an efficient tool for ultrafast imaging through what is called serial time-encoded amplified microscopy (STEAM [109]) and such a technique has enabled the recording of various ultrafast light-matter interactions. Among them, the CORIA-DOL group has for instance applied 1D DFT-based imaging to the recording of single shock waves in a precedent PhD thesis work [115,116]. However, such a ns resolution is not sufficient to resolve the dynamics of many physical processes occurring on the ps scale, like laser-matter interactions or light propagation itself. This last chapter is then dedicated to the demonstration of a single-shot Tfps 2D optical imaging technique with both ps and ns resolution. The main objective of this work is to provide a system which is user-friendly and could be brought out of a laboratory environment, contrary to most of the existing techniques. This chapter is then structured as follows. The substantial state-of-the-art of ultrafast imaging techniques is first presented, which allows to highlight the best performances accessible to date but also the main limitations of the current techniques. This work is then focused on a specific technique, known as **sequentially timed all-optical mapping photography** (STAMP), and its improvement through the use of **acousto-optic programmable dispersive filtering** but also of digital in-line holography. This original technique is eventually demonstrated experimentally through the tracking of ultrafast phenomena on both the ps and ns scales. Its potential refinements and limitations are eventually discussed.

5.1 Introduction & state-of-the-art

Capturing the transient dynamics of ultrashort events focuses the attention of the scientific community for decades in biomedical science, chemistry and physics [117–120], and ultrafast imaging is now routinely used for research and industrial applications. The need for high temporal and spatial resolutions has then remarkably fueled unprecedented advances in ultrafast optical imaging, and sub-picosecond and sub-nanometer resolutions are now accessible to various technologies. Transient phenomena are traditionally captured using pump-probe methods, which are however intrinsically limited to highly repeatable experimental conditions [121–123]. Some techniques, such as time-stretch imaging [109], leverage their high throughput capabilities for recording high-speed processes on long - microsecond - time scales with frame rates in the order of a hundred Mfps [115, 124]. Nevertheless, such frame rates are not sufficient to resolve many ultrafast events and **single-shot techniques** with frame intervals in the picosecond range - or less - are required for imaging e.g. laser-induced phenomena [125, 126] or light propagation itself [127, 128]. In the last decade, a myriad of remarkable single-shot imaging systems have then been developed based on a variety of technologies. The most striking ones are presented in Fig. 5.1 along with their performances in terms on imaging speed and number of images per acquisition.

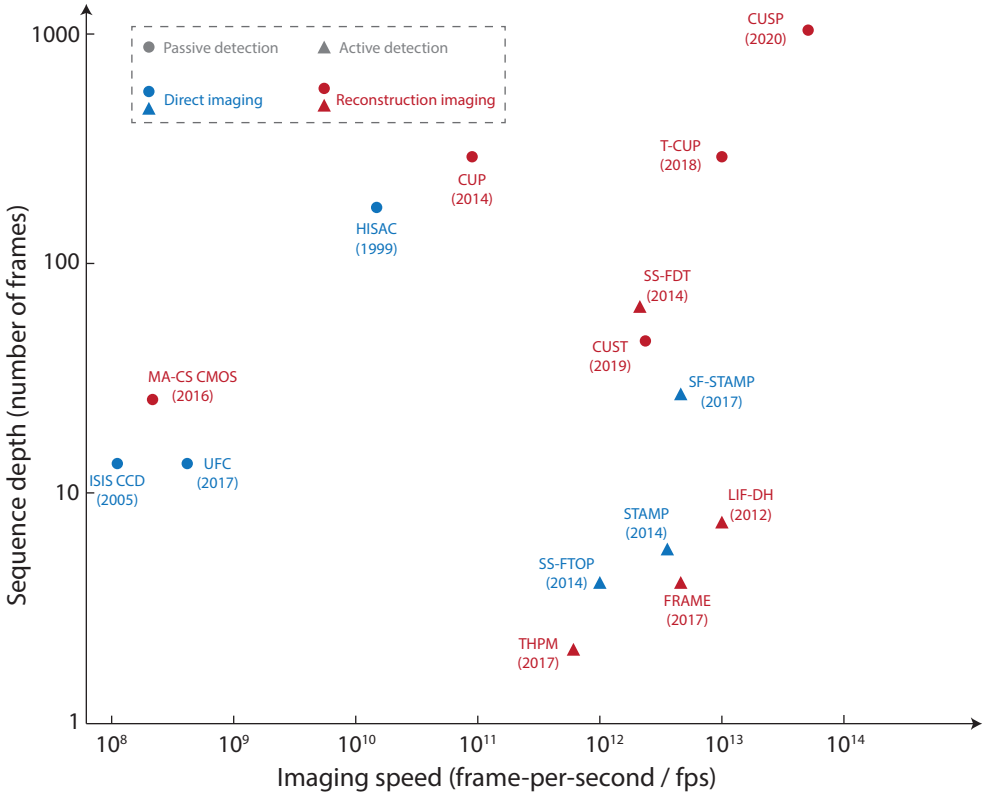

Figure 5.1: **Comparison of single-shot ultrafast optical imaging techniques** in terms of sequence depth and frame rate. Adapted from [122] and updated.

Single-shot methods can be separated between passive and active detection and further between direct imaging and reconstruction imaging [122, 129], each family having its strengths and limitations. Passive detection refers to the use of custom-designed pulse trains to probe ultrashort events while active detection relies on specific ultrafast detection schemes. On the one hand, the best performances to date in terms of imaging speed and sequence depth are undoubtedly obtained with passive detection and image reconstruction using advanced algorithms such as compressed sensing. Among those computational imaging methods, compressed ultrafast photography (CUP) [130] and its noteworthy upgradings and variants [125, 127, 131–134] then manage to reach up to 70 trillion Hz frame rates [135] and theoretically up to more than 180 Tfps [136], few hundreds of femtosecond frame intervals and potentially sequences with hundreds of frames, in a single camera exposure (see Fig. 5.1). Albeit being the spearhead of ultrafast imaging techniques and particularly relevant in a laboratory environment, these techniques could suffer from their complex reconstruction schemes hindering real-time operation and from their low flexibility. On the other hand, active imaging techniques using spatially-, temporally-, and/or spectrally-tailored ultrafast pulse trains have enabled ultra-high frame rates with simpler experimental setups and without the need of complex computational algorithms [128, 137–139] but, in most cases, to the detriment of sequence depth and without the possibility to record the spectrum (e.g. fluorescence) emitted from the dynamic scene. Among them, sequentially timed all-optical mapping photography (STAMP) [140]) and more specifically its spectrally-filtered variant (SF-STAMP) [141, 142] offer trillion-frame-per-second frame rates with real-time operation but suffer, as most of the above-mentioned techniques, from the absence of adaptability as the main parameters - namely, frame rate and exposure time - cannot be independently adjusted.

To answer this need for an independent and user-friendly "on-demand" control of these parameters for potential real-world applications, we introduce in this chapter an agile technique combining spectrally-filtered STAMP with an electronically-controllable compact acousto-optics-based phase and amplitude shaper. In the following, we recall the working principle of the SF-STAMP technique and highlight the parameters affecting its performances. We also introduce digital in-line holography as a tool to simplify its experimental implementation. We then present the acousto-optic programmable dispersive filter (AOPDF) as an efficient amplitude and phase controller within a SF-STAMP setup. This original technique is eventually demonstrated to be on par with the current state-of-the-art by performing single-shot imaging on ultrafast phenomena with different timescales.

5.2 Principles of sequentially timed all-optical mapping photography

5.2.1 Standard STAMP

Fig. 5.2 shows the key elements of a STAMP setup, namely an ultrashort pulse source, a temporal mapping device, a spatial mapping device and finally an image sensor. The core of the STAMP technique is to exploit the time separation of the chirped pulse's spectral components to obtain

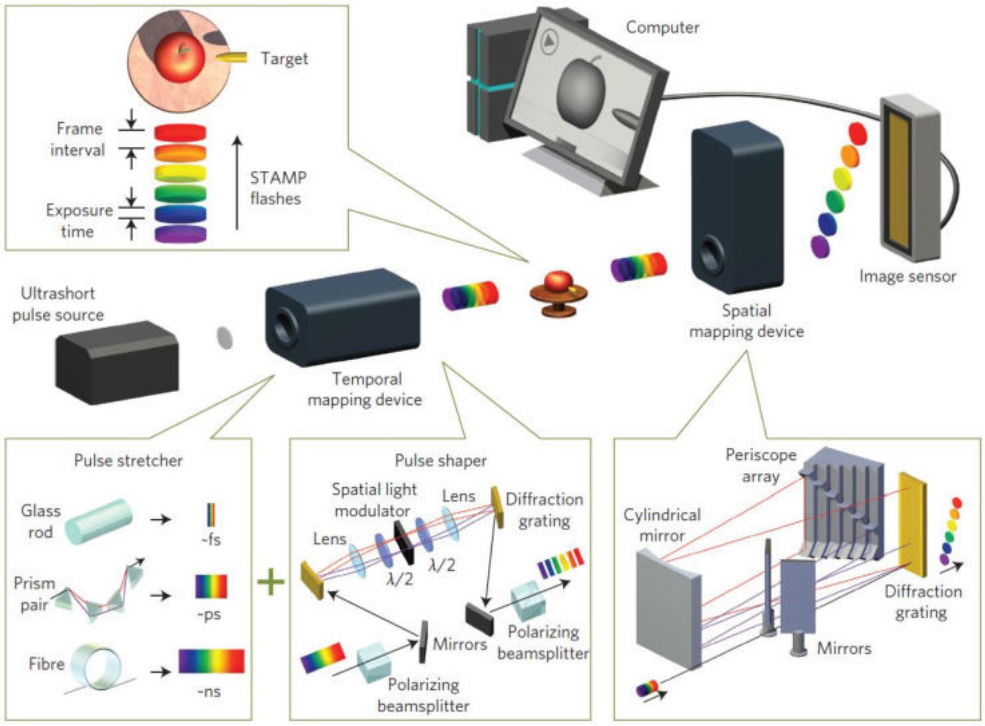

Figure 5.2: **General principles of STAMP**, highlighting the main steps to achieve Tfps imaging. Reproduced from [140].

snapshots at different instants. Therefore, the laser pulse needs to have a broad spectrum or a spectral broadening stage has to be used, i.e. through nonlinear propagation (SPM) in optical fibers. The ultrashort pulse is then stretched in order to distribute its spectral components in time. The resulting chirping factor is controlled so that the desired frame rate and exposure time are achieved. Prior to the illumination of the object, a pulse shaping stage can take place as well. Its main purpose is to divide the main broadband pulse into a set of sub-pulses that are already separated in time using the stretcher. This way, the central wavelengths and spectral widths of the generated sub-pulses can be adjusted and this permits the control the exposure time of the imaging system to a certain extent. The pulse stretching (time domain) step is usually implemented by propagating the laser pulse in glass rods or dispersive elements such as prisms while the pulse shaping (spectral domain) is usually performed using complex setups based on 4-f lines with spatial light modulators [140, 142]. Finally, the spatial information of the object in motion is recorded on the spatial profile of the generated sub-pulses, where each of them captures the object at a different instant. These sub-pulses are then spatially separated depending on their wavelength using a spatial mapping device. Once they reach the image sensor, each sub-pulse (corresponding to an image of the object at a different instant) then covers a specific area of the image sensor without a spatial overlap with other sub-pulses. This way, a single image sensor can acquire several images of the moving object at different instants, with a very small time between frames and simply using a single initial laser pulse.

One approach for the spatial separation of the sub-pulses is to use a diffraction grating along

with a set of periscopes. The diffraction grating spatially disperses the sub-pulses in the horizontal direction, and therefore diffracts each sub-pulse at a different angle. Each sub-pulse is subsequently directed toward a different periscope using a cylindrical mirror. Given that each periscope has a different distance between its mirrors, the sub-pulses are then vertically aligned toward the diffraction grating and eventually sent to the image sensor, which acquires the multiple vertical images as a single image. This approach for the spatial mapping is deemed complex as it requires precise alignment of several optical elements. We will present in the next section a more user-friendly alternative to this stage.

We have seen that in STAMP experiments, broadband chirped pulses are used to illuminate the object under study, each frequency then capturing a snapshot of the dynamic scene at different instants [140]. The different wavelengths are subsequently spatially separated in the form of several sub-pulses with different central wavelengths. The sub-pulses, corresponding to the consecutive frames, are finally recorded using a CCD sensor. As the snapshots are obtained through the spatial separation of specifically selected spectral bands from the main spectrum of the laser pulse, the exposure time of the technique is simply defined by the duration of the extracted sub-pulses. It can be obtained if the spectral width of the extracted sub-pulses along with the initial chirp of the broadband input pulse are known. It is given by the following expression [140]:

$$ET(i) = \sqrt{\left(\frac{2\lambda_{0i}^2 ln\,2}{\pi c \Delta\lambda_i}\right)^2 + (D.\Delta\lambda_i)^2}, \tag{5.1}$$

where, *i* determines the pulse number, $\Delta\lambda_i$ is the spectral bandwidth of a pulse *i*, λ_{0i} is the center wavelength of pulse *i*, *ET(i)* is the pulse width of pulse *i* and *c* is the light velocity. The initial chirp of the broadband input pulse is a major feature in the determination of the time between frames as well since it quantifies the temporal separation between the spectral components of the input pulse. Therefore, by knowing the spectral gap between consecutive sub-pulses, the time between frames can be calculated using the following formula:

$$\Delta T_{i,i+1} = D.\Delta\lambda_{i,i+1} \tag{5.2}$$

With $\Delta\lambda_{i,i+1}$ representing the spectral gap between the consecutive sub-pulse *i* and sub-pulse *i+1* and $\Delta T_{i,i+1}$ representing the respective time between them. As a result, the total observation window of the imaging system is the summation of the times between the generated sub-pulses and can be written as:

$$\Delta T = \sum_{i=1}^{n-1} \Delta T_{i,i+1} \tag{5.3}$$

Where ΔT is the total window of observation and n is the number of the generated sub-pulses.

5.2.2 Spectrally-filtered STAMP

As mentioned previously, the spatial mapping step can be highly complex and an alternative approach has then been developed. It is termed spectrally-filtered sequentially timed all-optical mapping photography (SF-STAMP) and achieves the spatial separation of the different wavelengths using the combination of a diffractive optical element (DOE) and a tilted spectral filter (SF) [141]. The DOE divides the input pulse into several replicas propagating in different directions while, for each replica, the angle of incidence on the spectral filter fixes the transmitted central wavelength, as shown in Fig. 5.3. In this configuration, both optical elements are set along the optical axis of the imaging laser pulse, and the only moving element is the spectral filter that needs to be tilted with respect to the optical axis. This angle does not affect the propagation of the transmitted laser pulse. This makes the SF-STAMP variant much simpler and easier to implement and it has been first demonstrated with a 5 sub-pulses sequence, enabling the visualization of laser ablation on the picosecond timescale [141]. The sequence depth can be extended by using a DOE generating more replicas, and frame intervals close to 100 fs with 25 frames have for instance been reported [142]. Due to its simplicity, this principle can also be applied to different temporal regimes [143] and will thereby be used in this work.

5.2.3 Lensless SF-STAMP and digital in-line holography (DIH)

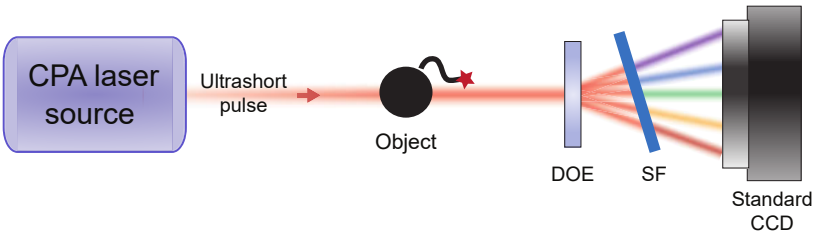

Figure 5.3: **Principle of SF-STAMP.** The spatial mapping of the different spectral bands is achieved using a diffractive optical element (DOE) and a spectral filter (SF). The DOE divides the image pulse into several replicas propagating in different directions and each replica hits the tilted SF at a different angle of incidence. A different spectral band, capturing the dynamic scene at a different instants, is then allowed to pass through the SF for each replica.

In the usual SF-STAMP system, the DOE and SF are comprised between two converging lenses in a 4f system. This restrains the object's position to a very limited range along the optical axis in order to obtain clear and possibly magnified images of it. The use of lenses also requires a careful alignment and might lead to some optical aberrations. Therefore, we decided to solely use the DOE/SF pair for the spatial separation of the spectral band of the stretched pulse and to build a lens-free optical setup for ultrafast burst imaging. Removing the lenses results in the recording

of an interference (fringes) pattern on the CCD sensor instead of its actual image. Fortunately, computational tools have been developed for the reconstruction of aberration-free images on a large range of positions along the optical axis through the principle of digital in-line holography (DIH), on which the CORIA-DOL team has a renowned expertise.

The recording process of digital in-line holograms can be simply expressed by applying a propagation model along the z-axis (i.e. the optical axis of the imaging system). Let $A_{im}(\mathbf{r},t)$ be the complex amplitude function due to the imaging pulse $I_{im}(\mathbf{r},t)$ and considered as the object to be recorded. The complex amplitude distribution in the CCD sensor plane located at a distance z_e from the object is obtained from the Huygens-Fresnel integral. According to Ref. [144], and by omitting the constant multiplicative phase term $exp\left(\frac{2i\pi z_e}{\lambda}\right)$, this integral can usefully be expressed as the following 2-D convolution:

$$A_{holo}(\mathbf{r},t,z_e) = [1 - A_{im}(\mathbf{r},t)] * *h(\mathbf{r},z_e) \tag{5.4}$$

where $h(\mathbf{r},z_e)$ is the Fresnel kernel:

$$h(\mathbf{r},z_e) = \frac{1}{i\lambda z_e} exp\left[\frac{i\pi(x^2+y^2)}{\lambda z_e}\right]. \tag{5.5}$$

The intensity distribution $\left(= A_{holo}.\overline{A_{holo}}\right)$ recorded by the sensor can also be expressed by using this formalism. Knowing that $1 * *h = 1$, it gives:

$$I_{holo}(\mathbf{r},t,z_e) = 1 - A_{im}(\mathbf{r},t) * *\left[h(\mathbf{r},z_e) + \overline{h(\mathbf{r},z_e)}\right] \tag{5.6}$$

where the top bar $\bar{.}$ stands for the complex conjugate. Note here that for simplification, the squared modulus term $|A_{im}(\mathbf{r},t) * *h(\mathbf{r},z_e)|^2$ has been omitted. This approximation is valid provided that the far-field conditions are satisfied [145]. As for the recording step, the reconstructed image at a given distance z_r from the CCD sensor can also be calculated by a convolution operation:

$$R(\mathbf{r},t,z_r) = I_{holo}(\mathbf{r},t,z_e) * *h(\mathbf{r},z_r) \tag{5.7}$$

It is easy to see, by introducing Eq. 5.6 in 5.7, that when the right reconstruction distance is reached (i.e. $z_r = z_e = z_{opt}$), we have:

$$R(\mathbf{r},t) = 1 - A_{im}(\mathbf{r},t) - A_{im}(\mathbf{r},t) * *h(\mathbf{r},2z_{opt}). \tag{5.8}$$

The reconstructed complex image amplitude $1 - A_{im}(\mathbf{r},t)$ is surrounded by the waves coming from the so-called twin image $-A_{im}(\mathbf{r},t) * *h(\mathbf{r},2z_{opt})$. By assuming that the contrast of the twin image fringes does not disturb the reconstructed sample volume, the far field conditions are thereby achieved in the present case. The real and imaginary parts as well as the phase of the reconstructed image can be obtained.

In order to demonstrate the capabilities of DIH, the preliminary experimental setup shown in

Fig. 5.3 was implemented. The laser source is a chirped pulse amplifier (CPA, Coherent Inc.) that generates linearly-polarized 100 fs pulses centered at 800 nm with a 10 nm bandwidth (FWHM) at a repetition rate of 1 kHz. The diffractive optical element (DOE, Holoeye DE224) allows to generate 2×2 beams at a diffraction angle of $\sim 5.1^{\circ}$ with respect to the optical axis while the SF (BPF, IRIDIAN, ZX000167) is set after the DOE. The SF exhibits a transmittance superior to $\sim$90 % at 830 nm and has a spectral bandwidth of 2.2 nm. The filtered beams are then captured by a CCD sensor (JAI, RM-4200 CL) with 2048×2048 pixels and 15.15×15.15 mm sensor dimensions. As a test target, two optical fibers were set at different positions along the optical axis prior to the DOE, with a shift between them. The CCD sensor then captures the fringe pattern shown in Fig. 5.4a. Using DIH, we were eventually able to reconstruct individual images of the fibers, as shown in Fig. 5.4b and c. We were also able to determine the distance at which they were set with respect to the CCD sensor, an additional information that cannot be obtained using conventional imaging.

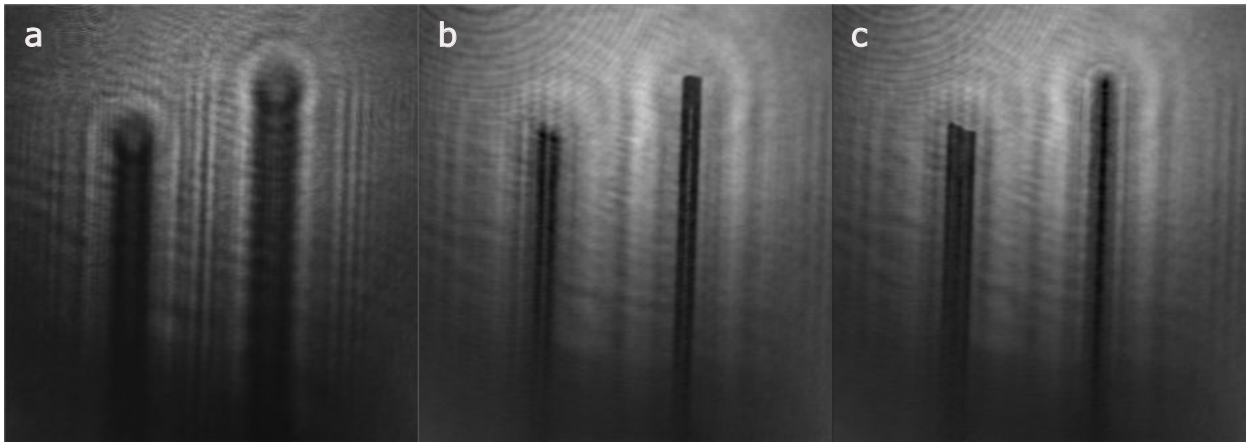

Figure 5.4: **Image reconstruction using digital in-line holography.** a) Both fibers are out of focus. b) Reconstruction in the exact plane of the right fiber. c) Reconstruction on the exact plane of the left fiber.

5.2.4 Interference filter adjustment

The main property of the spectral filter is its fixed band-pass window $\Delta\lambda$. Yet, the angle of incidence of light with respect to the normal of the SF plane alters the transmitted central wavelength $\lambda_0(\beta)$. The angle dependence of the central wavelength of the transmitted band is expressed as follows [141]:

$$\lambda_0(\beta) = \lambda_0 \left[1 - \frac{\beta^2}{2n_{eff}^2}\right] \tag{5.9}$$

Where $\lambda_0 = 830$ nm is the central wavelength of the pulse at a normal angle of incidence with respect to the SF plane, β is the angle of incidence while $n_{eff} = 1.45$ is the effective refractive index. By assuming the transmission window to have a Gaussian shape and using the angle-dependent

central wavelength along with the width (FWHM) of the bandpass, the wavelength-dependent transmitted intensity of the SF can be expressed as:

$$I(\lambda) = exp\left(\frac{-4ln(2)(\lambda - \lambda(\beta))^2}{\Delta\lambda_{SF}^2}\right) \tag{5.10}$$

Where $\Delta\lambda_{SF}$ is the spectral bandwidth of the SF. In Fig. 5.3, the DOE/SF pair is used for the spatial extraction from a single pulse of five spectral bands that are equally spaced and non-overlapping in the spectral domain. The beams diffracted from the DOE take the form of the four corners of a square on the transverse axes while the non-diffracted beam (zero-order) hits the center of the square (Fig5.5.a). Initially, the SF is set after the DOE orthogonal to optical axis. In this case, the beams exiting the DOE can be represented as vectors in 3D Cartesian coordinates systems with the origin of each system defined by the location at which the corresponding beam crosses the SF as shown in Fig. 5.5.b. The beams are then represented with normalized vectors as:

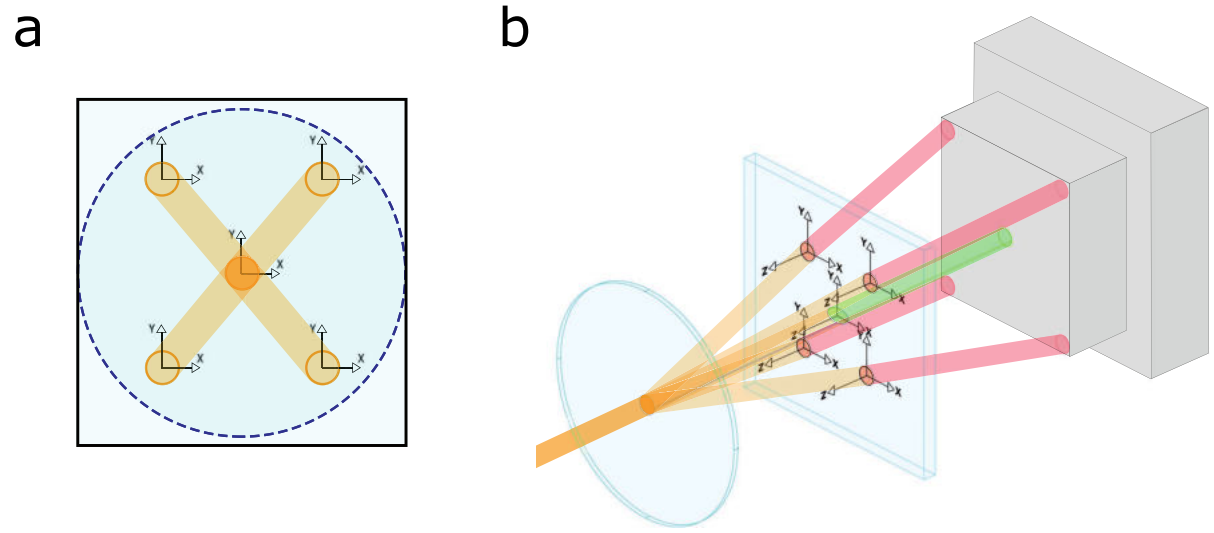

Figure 5.5: **Sub-pulses generated by diffraction on the DOE.** a) Positions in the front view. b) Coordinates of the 5 sub-pulses.

$$\mathbf{V}_1\,(\,\mathbf{x}_1, \mathbf{y}_1,\ \mathbf{z}_1) = (sin(\beta)cos(\frac{\pi}{4}), sin(\beta)sin(\frac{\pi}{4}), cos(\beta)) = (V_{1x}, V_{1y}, V_{1z})\,; \tag{5.11}$$

$$\mathbf{V}_2\,(\,\mathbf{x}_2, \mathbf{y}_2,\ \mathbf{z}_2) = (sin(\beta)cos(-\frac{\pi}{4}), sin(\beta)sin(-\frac{\pi}{4}), cos(\beta)) = (V_{2x}, V_{2y}, V_{2z})\,; \tag{5.12}$$

$$\mathbf{V}_3\,(\,\mathbf{x}_3, \mathbf{y}_3,\ \mathbf{z}_3) = (0, 0, 1) = (V_{3x}, V_{3y}, V_{3z})\,; \tag{5.13}$$

$$\mathbf{V}_4\,(\,\mathbf{x}_4, \mathbf{y}_4,\ \mathbf{z}_4) = (sin(\beta)cos(\frac{3\pi}{4}), +sin(\beta)sin(\frac{3\pi}{4}), cos(\beta)) = (V_{4x}, V_{4y}, V_{4z})\,; \tag{5.14}$$

$$\mathbf{V}_5\,(\,\mathbf{x}_5, \mathbf{y}_5,\ \mathbf{z}_5) = (sin(\beta)cos(\frac{-3\pi}{4}), sin(\beta)sin(\frac{-3\pi}{4}), cos(\beta)) = (V_{5x}, V_{5y}, V_{5z})\,; \tag{5.15}$$

The diffracted beams from the DOE have the same angle β with respect to the normal of SF plane. Therefore, the SF transmits the same spectral band for all the diffracted beams. This can be changed by rotating the SF in the azimuthal and radial planes (angles θ and ϕ, respectively), which rotates the previously defined Cartesian coordinate systems in the following manner:

$$\begin{pmatrix} \mathbf{x'}_i \\ \mathbf{y'}_i \\ \mathbf{z'}_i \end{pmatrix} = \begin{pmatrix} cos\theta & 0 & sin\theta \\ 0 & 1 & 0 \\ -sin\theta & 0 & cos\theta \end{pmatrix} \begin{pmatrix} \mathbf{x}_i \\ \mathbf{y}_i \\ \mathbf{z}_i \end{pmatrix} \tag{5.16}$$

$$\begin{pmatrix} \mathbf{x''}_i \\ \mathbf{y''}_i \\ \mathbf{z''}_i \end{pmatrix} = \begin{pmatrix} 1 & 0 & 0 \\ 0 & cos\phi & sin\phi \\ 0 & -sin\theta & cos\theta \end{pmatrix} \begin{pmatrix} \mathbf{x'}_i \\ \mathbf{y'}_i \\ \mathbf{z'}_i \end{pmatrix} \tag{5.17}$$

The beams' vectors on the rotated Cartesian systems are then given by:

$$\mathbf{V"}_{i_{(\mathbf{x"}_i, \mathbf{y"}_i, \mathbf{z"}_i)}} = (V"_{ix"}, V"_{iy"}, V"_{iz"}) \tag{5.18}$$

$$V"_{ix"} = V_{ix}cos\theta - V_{iz}sin\theta \tag{5.19}$$

$$V"_{iy"} = V_{iy}cos\phi + sin\phi(V_{iz}cos\theta - V_{ix}sin\theta) \tag{5.20}$$

$$V"_{iz"} = -V_{iy}sin\phi + cos\phi(V_{iz}cos\theta - V_{ix}sin\theta) \tag{5.21}$$

The angles of incidence of the five beams with respect to the normal of the tilted SF is then found as follows:

$$\beta_i = arccos\left(\frac{V"_{iz"}}{|\mathbf{V"}_i|}\right) \tag{5.22}$$

Through the set of effective angles $\beta_{1,2,3,4,5}$ obtained using Eq. 5.22 along with their corresponding transmission central wavelength using Eq. 5.9, the central wavelength of the transmitted spectral bands for each of the 5 sub-pulses is plotted as a function of the azimuthal and radial angles (θ, ϕ), as shown on Fig. 5.6.

Fig 5.6 shows that the angle pairs (θ, ϕ) that allow for the transmission of light through the SF for a given sub-pulse form a ring shape. The center of the ring is defined by the initial propagation direction of the sub-pulse while its inner and outer radii are defined by the spectral bandwidth of the laser source. The limited bandwidth of the input pulse intrinsically limits the freedom in the azimuthal and radial angles of the spectral filter, and thereby hinders the acquisition of equally-spaced non-overlapping (in the spectral domain) sub-pulses. For instance, if we only exploit the spectral width of the laser pulse, the simultaneous transmission of light for the five

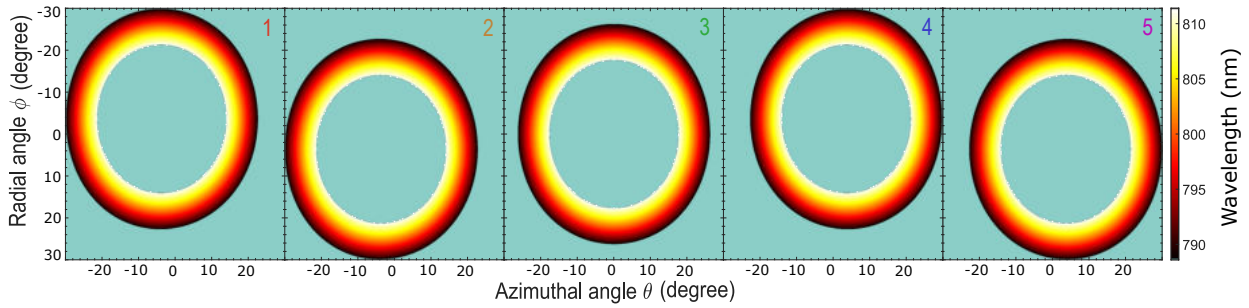

Figure 5.6: **Transmission of the spectral filter.** Central wavelength of the transmitted spectral bands for each of the 5 sub-pulses versus azimuthal and radial angles.

sub-pulses cannot be achieved. Therefore, it is vital to exploit the pedestal of the laser pulse spectrum that extends to up to 25 nm. By overlapping the rings in Fig. 5.6, the intersection between them defines the angle pairs at which we have the simultaneous transmission for the 5 sub pulses. They are shown on Fig. 5.7a.

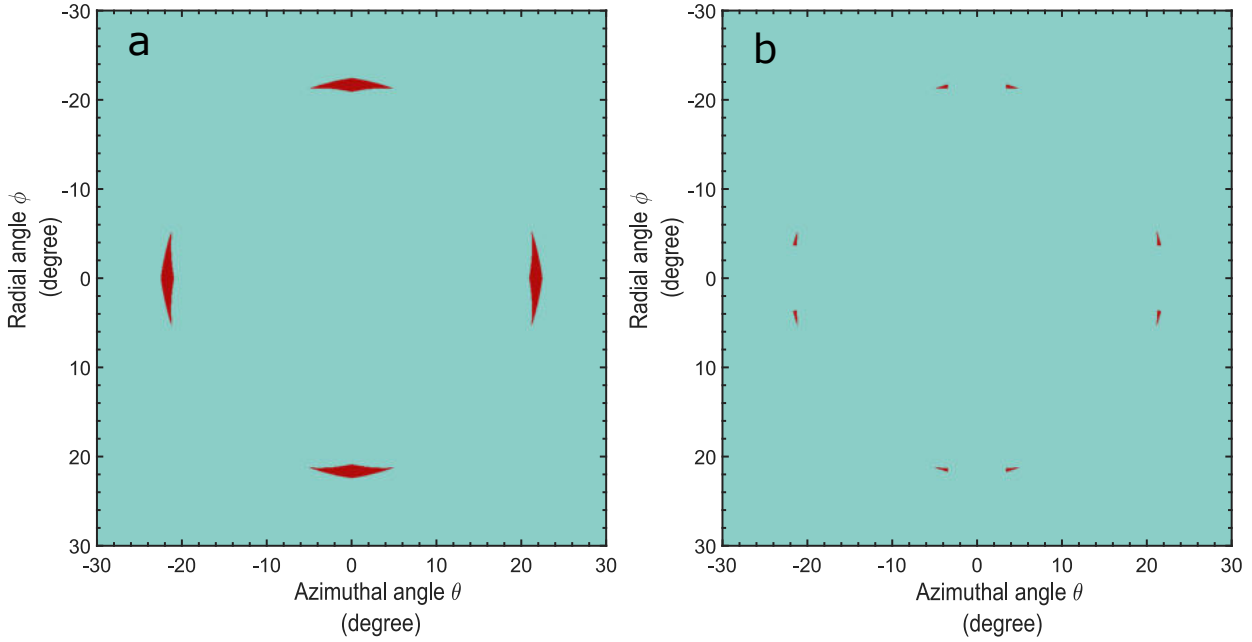

Figure 5.7: **Constrained transmission of the spectral filter.** (*left*) Conditions for the simultaneous transmission of the 5 sub-pulses. (*right*) Extra constraint of a spectral gap of at least 3 nm.

The set of angle pairs (θ, ϕ) was further reduced to contain only the pairs that result in the transmission of 5 sub-pulses with a spectral separation of at least 3 nm. This constraint is set so that the transmitted sub-pulses have a spectral separation between them that exceeds the band-pass window of the SF. As a result, capturing redundant images of the object on multiple sub-pulses is avoided. This set is shown on Fig. 5.7 b. Imposing a higher spectral separation reduces the angle pairs set even more and the angle pairs set becomes limited to very specific points in the

whole 2D space. Therefore, considering the limited precision of the rotation opto-mechanics, the experimental adjustment of angles θ and ϕ needed to meet these points is evidently challenging. The central wavelength of the transmitted spectral band of each of the 5 sub-pulses for this specific set of angle pairs is shown on Fig. 5.8a, while Fig. 5.8b is a zoomed view on the angle ranges $\theta \in [19.9^\circ; 22.9^\circ]$ and $\phi \in [2.4^\circ; 5.4^\circ]$ of Fig. 5.8a.

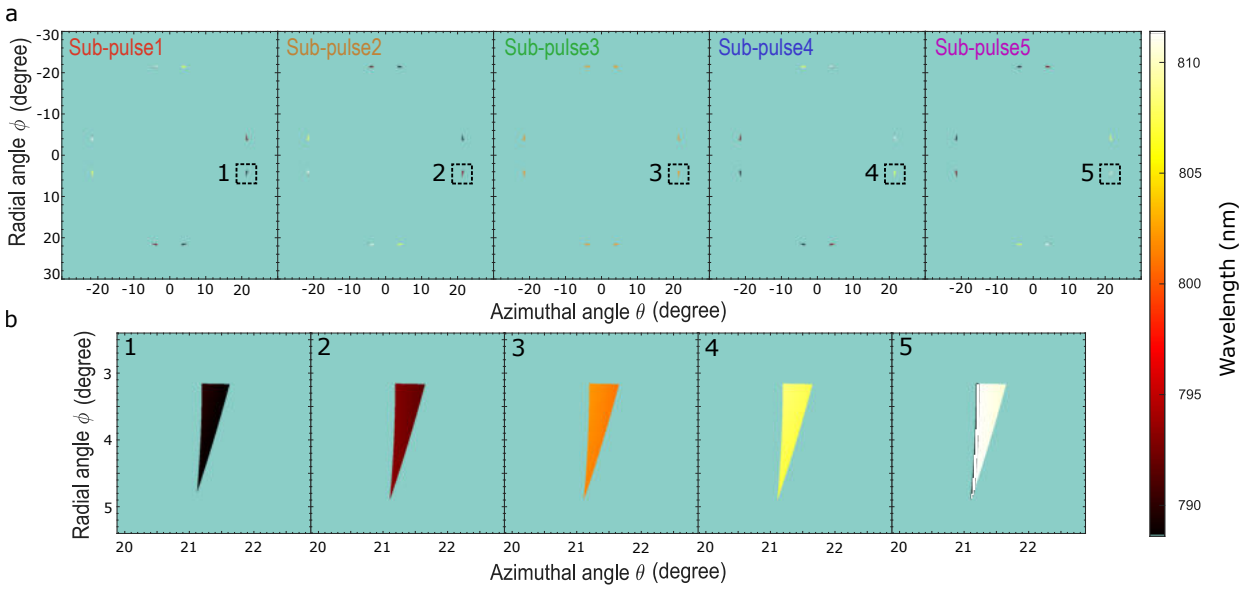

Figure 5.8: **Central wavelength of the transmitted pairs.** General and zoomed views.

Based on the color maps in Fig. 5.8b, if the SF is rotated in the azimuthal and radial planes with angle pair (θ, ϕ) that falls within the colored triangular shape as shown in 5.8a, the SF will transmit a different spectral band for each of the 5 sub-pulses. Therefore, the SF was rotated around the angles $\theta = 21.5^\circ$ and $\phi = 3.5^\circ$ and the resulting filtered spectrum is shown on Fig. 5.9c along with the expected spectrum on Fig. 5.9b.

The measured spectrum in Fig. 5.9c differs slightly from the desired spectrum in Fig. 5.9b where a larger spectral overlap is seen between sub-pulse 4 with sub-pulse 5 while a lesser overlap is seen between sub-pulse 1 with sub-pulse 2. This difference is due to the precision of the rotation platforms as well as an existing slight rotation of the diffraction pattern of the DOE with respect to the transverse axes. Nevertheless, the spectral overlap exist in both Fig. 5.9b and c regardless to the fact that this spectral distribution of the five sub-pulses is shown to be optimal. This overlap rises a set of issues with regard to the proposed basic SF-STAMP setup. Firstly, the spectral overlap between the sub-pulses indicates that although the input pulse is temporally stretched, there is a temporal overlap between sub-pulse 1 and sub-pulse 2 and between sub-pulse 4 and sub-pulse 5. As a result, these sub-pulses illuminate the object at partially the same instant and therefore capture the same image. In addition, the spectral overlap indicates that a portion of sub pulse 1 would pass through the SF along with sub-pulse 2 and vice versa. In consequence, the SF-STAMP system captures only 3 valid images of the object instead of five. Secondly, the spectra of the five

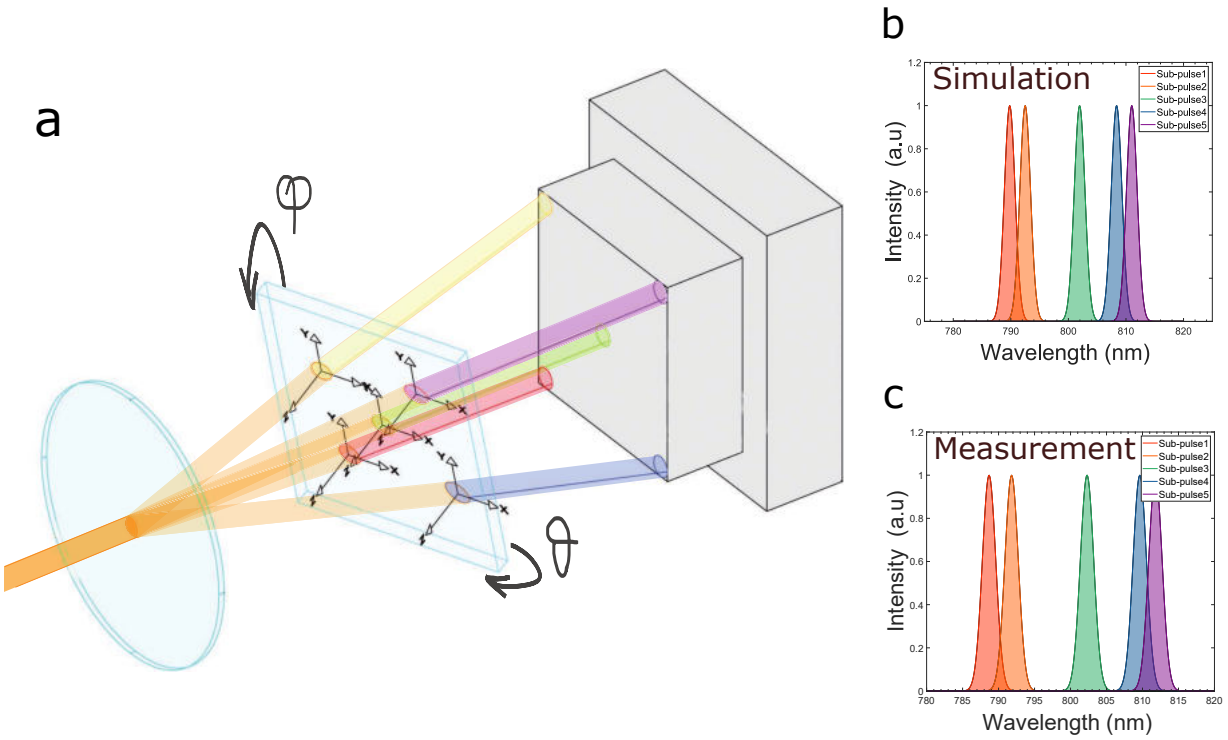

Figure 5.9: **Effect of the tilt of the spectral filter.** a) General view. b) Expected spectrum. c) Experimental spectrum.

sub-pulses are not equally spaced. Therefore the time between the images that they capture is non-constant. Thirdly, the spectral width of the 5 sub-pulses is fixed to a constant value of 2.2 nm, which represents the band-pass window of the SF. Therefore, the exposure time and time between frames cannot be adjusted independently as the only adjustable parameter in the setup is the chirping factor of the input pulse. Finally, the last issue regarding this basic SF-STAMP system is raised by Fig. 5.10.a and b. The spectra of the diffracted and filtered sub-pulses overlap with the pedestal of the spectrum of the input pulse, while the spectrum of the central sub-pulse falls within the spectral range of the input pulse. This leads to a huge difference in the intensity of the diffracted sub-pulses with regard to the non-diffracted sub-pulse. The difference that can be clearly seen in the huge contrast between them in the corresponding images on Fig. 5.10b and thereby results in a very poor intensity dynamics.

These issues can be fixed in several ways. On the one hand, an extra spectral broadening stage could primarily fix some of the issues stated above since a larger spectrum provides more freedom in rotation of the SF. Thereby, it might result in obtaining equally spaced sub-pulses that fall within the FWHM of the broadened laser pulse in the spectral domain. This can potentially fix the contrast issue, and it might also even the time between frames and eliminates the spectral overlap between the sub-pulses as well. On the other hand, a pulse shaping can eliminate the spectral overlap between the sub-pulses but also adjust their spectral width below 2.2 nm. Therefore, it allows for a slight change in the pulse duration of the sub-pulses independently from their time separation. The complexity of "standard" spectral broadening using SPM in optical fibers as well as the usual pulse

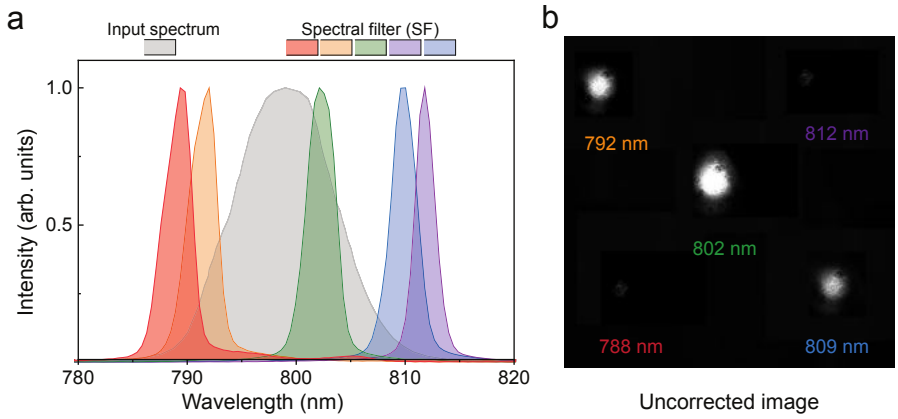

Figure 5.10: **Poor intensity dynamics.** a) Input laser spectrum compared with the normalized transmission bands of the STAMP spectral filter (SF). b) The convolution of the input spectrum with the SF leads to an inhomogeneous sub-pulse intensity distribution on the CCD camera and is associated with poor intensity dynamics.

shaping schemes (e.g. spatial light modulators) contradict with our attempt to implement a simple, flexible and user friendly SF-STAMP imaging system. Such pulse shaping stages, in addition to being bulky and expensive, exhibit a very low flexibility as the independent adjustment of the frame rate and exposure time by the end-user. **Here, we then propose to circumvent these steps using a single acousto-optics programmable dispersive filter for both temporal and spectral shaping and then for the full control of the illumination conditions.**

5.2.5 Acousto-optic programmable dispersive filtering

5.2.5.1 AOPDF-based pulse shaping

Acousto-optic programmable dispersive filters (AOPDF) have originally been designed to compensate for the group delay dispersion (GDD) in ultrafast laser systems [146], carrier-envelope phase (CEP) stabilization [147, 148] or pulse shaping in various applications [149–151]. AOPDF have also been used as ultrafast delay lines in terahertz spectroscopy [152] and pump-probe spectroscopy and imaging [153]. Their ability to fully tailor the pulse phase and amplitude then enabled the synchronization and chirp control of fs pulses, e.g. in stimulated Raman spectroscopy [154, 155].

The AOPDF [156] is a pulse shaping system that takes advantage of the high birefringence of acousto-optic crystals for both the acoustic and optical waves [157]. When an acoustic wave propagates through such crystals, it alters its optical properties: the crystal lattice is alternately compressed and relaxed in response to the oscillating wavefront in what is known as the elasto-optic effect. Thus, the refractive index fluctuates and can diffract the incoming light if the Bragg diffraction condition is met. The crystal then acts as a wavelength-dependent diffraction grating and this feature allows for the use of the acousto-optic crystal as a spectral filter with control over both the spectral amplitude and phase. Consequently, in the context of this work, the AOPDF could be efficiently used to: *(i)* replace the stretcher for the separation of the spectral components

of the input light pulse in time, *(ii)* eliminate the existing spectral overlap between the sub-pulses, *(iii)* adjust the time between them, and *(iv)* equalize their respective intensities. In addition, all these features would be accessible simply using a custom-designed electronically-controllable RF signal, making the system highly flexible and user-friendly, as shown in Fig. 5.11.

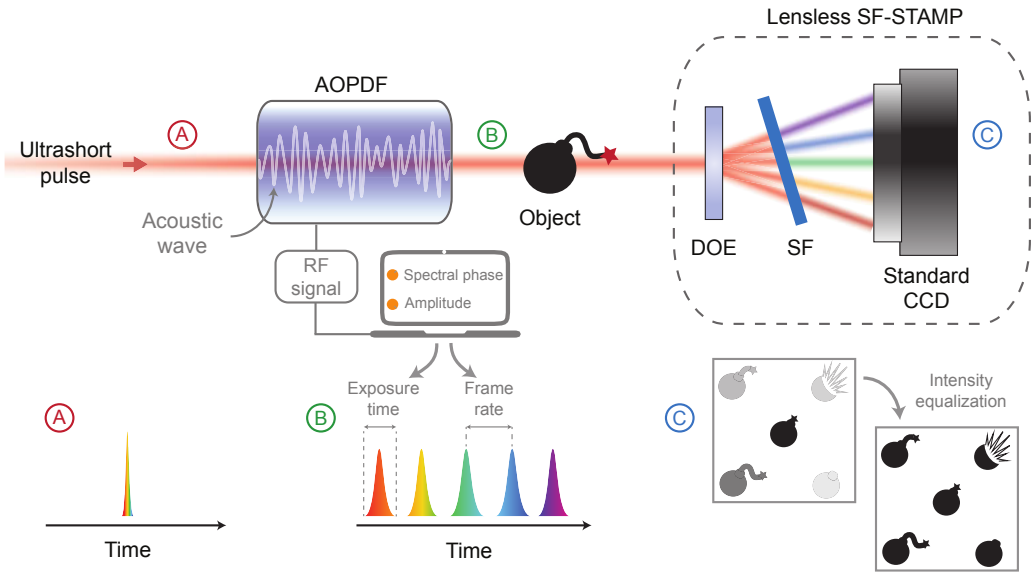

Figure 5.11: **Principle of operation.** The acousto-optics programmable dispersive filter (AOPDF) tailors the pulse shape in both the spectral and temporal domains via its interaction with an electrically-driven acoustic wave, then enabling the full and independent control over the exposure time and frame rate in the subsequent SF-STAMP detection scheme, comprising a diffractive optical element (DOE) and a tilted spectral filter (SF).

The AOPDF (Dazzler, Fastlite) used in our experiments consists of a 25 mm long TeO_2 birefringent acousto-optic crystal where a longitudinal interaction between the acoustic wave and the optical field (polarized along the ordinary axis) occurs. This interaction can be viewed as a three wave mixing process. It results in the diffraction of optical wavelengths to the extraordinary axis depending on the phase matching conditions. These conditions are given by:

$$\mathbf{k}_{diff} = \mathbf{k}_{opt} + \mathbf{k}_{ac} \tag{5.23}$$

where $\mathbf{k}_{diff}$, $\mathbf{k}_{opt}$ and $\mathbf{k}_{ac}$ are the diffracted, optical and acoustic wavevectors, respectively. Depending on the angles of incidence of the acoustic wave and the optical field, the phase matching conditions create an almost bijective relationship between the optical and acoustic frequencies (thick crystal). This relationship is nearly linear and depends mainly on the crystal properties in addition to the phase matching conditions and is given by:

$$\omega_{opt}/\omega_{ac} \sim \alpha \tag{5.24}$$

where α is the optical to acoustic frequencies ratio. Here, $\alpha = 2.3 \times 10^{-7}$. This enables pulse

shaping of an optical field simply using an electronically-generated acoustic wave. The shaping process in the AOPDF can be represented with a convolution of the complex electric field of the input optical wave with the acoustic signal. In the frequency domain, this convolution is expressed as:

$$E_{diff}(\omega_{opt}) \propto E_{in}(\omega_{opt}).S(\omega_{ac}) = E_{in}(\omega_{opt}).S(\alpha.\omega_{opt}) \tag{5.25}$$

Based on Eq. 5.25, the amplitude of the diffracted electric field E_{diff} at a given angular frequency ω_{opt} is proportional to input electric field E_{in} at the same angular frequency. The proportion is determined by the amplitude of the acoustic wave with the frequency $\alpha\omega_{opt}$, as dictated by the phase matching conditions.

5.2.5.2 Amplitude control

The amplitude of the diffracted electric field E_{diff} can be tailored through the design of the acoustic wave that interacts with the input electric field E_{in}. So, in order to eliminate the spectral overlap between the sub-pulses, the acoustic wave is designed for the purpose of diffracting only non-overlapping spectral components of the sub-pulses as shown in Fig. 5.12a. The overlap between sub-pulses 4 and 5 is reduce to less than 4% of the intensity of each while the overlap between sub-pulses 1 and 2 is reduced to less than 0.3%. The sub-pulses are set to have a spectral width of 1.5 nm centered at $\lambda_1 = 788$ nm, $\lambda_2 = 792$ nm, $\lambda_3 = 802$ nm, $\lambda_4 = 809$ nm and $\lambda_5 = 812$ nm. After the elimination of the overlap, the spectra of the sub-pulses would be proportional to the multiplication of the input spectrum with the AOPDF mask as stated by Eq. 5.25.

$$E_{diff}(\lambda) \propto E_{in}(\lambda).\sum_{i=1}^{5} U(\lambda_i - 0.75) - U(\lambda_i + 0.75) \tag{5.26}$$

Where U is the unit step function and λ_i is the central wavelength of sub-pulse i. As a result, the sub-pulses would have a significant difference in their intensities depending on their position relative to the input spectrum. Sub-pulses 3 and 5 are the most and least intense, respectively, as shown in Fig. 5.12b. Thus, the sub-pulse 3 would saturate the CCD sensor while sub-pulse 5 would result in a very low signal to noise ratio. To fix this problem, the AOPDF mask is adjusted in the following manner:

$$AOPDFmask = Norm\left(\frac{1}{E_{in}(\lambda).\sum_{i=1}^{5} U(\lambda_i - 0.75) - U(\lambda_i + 0.75)}\right) \tag{5.27}$$

The AOPDF mask is shown in Fig. 5.12c. The mask covers a spectral range of 25 nm with a maximum of 110 channels corresponding to a maximum resolution of 0.23 nm. This way, the diffraction efficiency is adjusted for each sub-pulse to eliminate the intensity difference between

them. The amplitude of the diffracted electric field can then be represented as:

$$E_{diff}(\lambda) \propto \sum_{i=1}^{5} U(\lambda_i - 0.75) - U(\lambda_i + 0.75) \tag{5.28}$$

As a result, the spectrum of the diffracted output pulse is made of five lobes with the same width

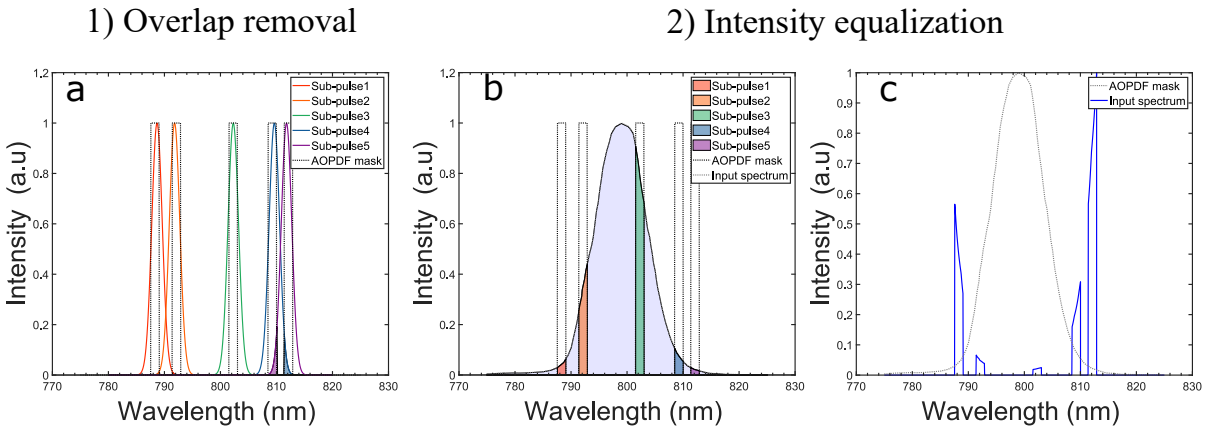

Figure 5.12: **Amplitude control.** a) Non-overlapping components. b) Relative pulse intensities. c) Mask applied on the AOPDF.

and quasi-equal intensities regardless to their spectral position with respect to the input spectrum. Each lobe represents the optical spectrum of one of the five sub-pulses. They are shown on Fig. 5.13a in contrast with the input spectrum and the AOPDF mask on the background. Fig. 5.13.b shows the achieved enhancement in illumination conditions of the imaging system compared to Fig. 5.10b. The sub-pulses illuminate the object in a similar manner, which allows for an optimal exploitation of the dynamic range of the CCD sensor. In addition, in order to make sure that

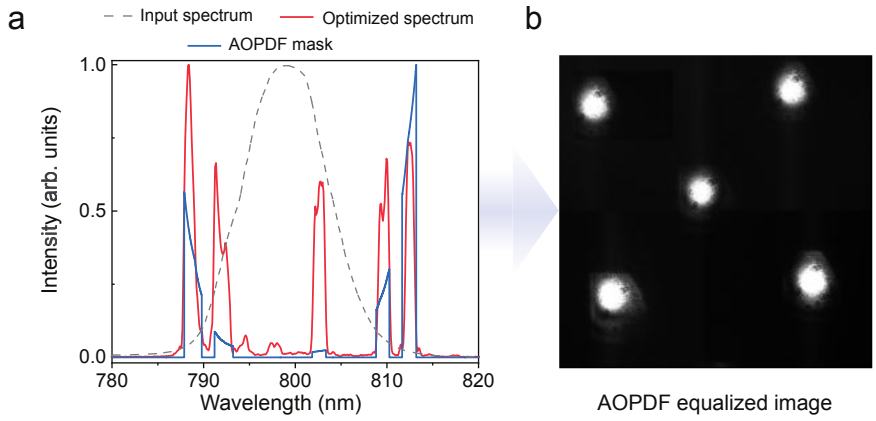

Figure 5.13: **Intensity equalization.** a) Amplitude mask applied on the AOPDF (blue) and resulting optimized spectrum (red) compared with the input spectrum (dotted gray). b) Resulting image with equalized intensities and optimized dynamics (raw images without any post-processing).

the spectral overlap between the sub-pulses is eliminated, each of the sub-pulses is diffracted individually using the AOPDF and the resulting images are shown on Fig. 5.14. We can clearly see that each sub-pulse illuminates the CCD sensor in a specific isolated area. Therefore, there is no spatial overlap between sub-pulses which indicates the lack of significant spectral overlap.

Figure 5.14: **Individual diffraction of each sub-pulse.**

5.2.5.3 Phase control

Eq. 5.25 also signifies that the spectral phase of the diffracted optical pulse is simply the addition of the initial phase of the input optical pulse with the induced phase due to the acousto-optic interaction in the crystal:

$$\phi_{diff} = \phi_{opt} + \phi_{AOPDF} \tag{5.29}$$

ϕ_{AOPDF} is a mere exploitation of the crystal birefringence to create group delay between wavelengths of the optical pulse depending on the position along the crystal at which they have been diffracted from the ordinary to the extraordinary axis, as shown in Fig. 5.15. The group delay is given by:

$$\tau(\omega) = (n_{go}(\omega)/c) \times z(\omega) + (n_{ge}(\omega)/c) \times (L - z(\omega)) \tag{5.30}$$

With n_{go} and n_{ge} being the ordinary and extraordinary group refractive indices, respectively. z(ω) is the distance covered by the optical frequency ω along the ordinary axis of the crystal and L the total length of the crystal (L = 25 mm). By adjusting z(ω), the group delay of every optical frequency ω can be adjusted to a maximum value of 8.5 ps. Thereby, the phase of the diffracted optical pulse can be controlled.

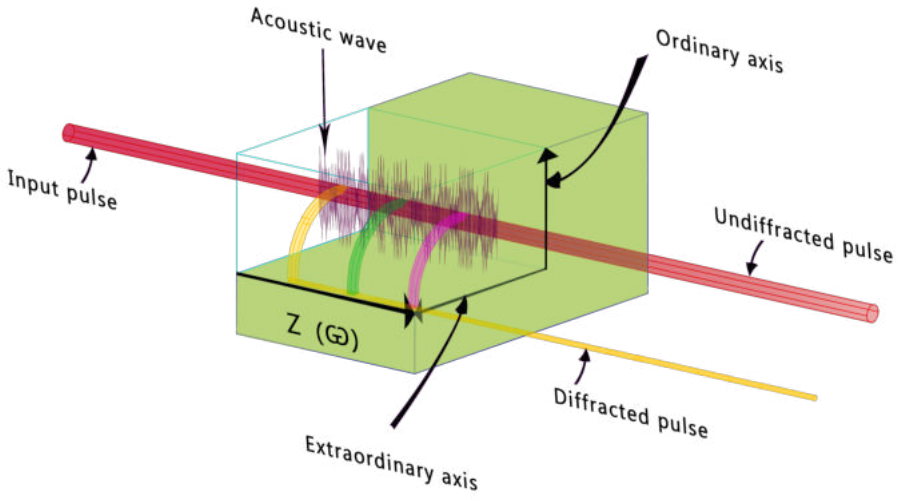

Figure 5.15: **Schematic representation of pulse diffraction in the AOPDF.**

First, the acoustic wave is set to cover most of the crystal length when interacting with the unchirped input pulse. This increases the diffraction efficiency of the frequency mixing process and allows to efficiently diffract a linearly chirped output pulse. The resulting equivalent accumulated dispersion leading to the chirp of the input pulse needs to be known in order to determine the pulse width of the generated sub-pulses along with the time between them using Eq. 5.1 and Eq. 5.2, respectively. Second, an additional group delay (positive or negative) is imposed on the second, third and fourth sub-pulse in order to equalize the time between the sub-pulses without affecting their width. Using these two steps, we can generate 5 equally-spaced sup-pulses in time within a range that extends to up to 8.5ps, as shown in Fig. 5.16 . As a result, the AOPDF is able to replace the stretcher in the SF-STAMP setup, and to adjust the time between frames independently of the exposure time. This makes the SF-STAMP system much more compact, less complex, user friendly, more flexible and easier to adjust for the observation of phenomena that occur in the picosecond scale. However, the proposed SF-STAMP imaging system is unable of capturing many transient or non-repeatable phenomena (e.g. in light-matter interactions) that occur in a larger timescale due to the limit in the AOPDF crystal length. In order to overcome this issue, an increase in the temporal flexibility of the proposed SF-STAMP imaging system is required. This has already been demonstrated e.g. using free-space angular-chirp-enhanced delay (FACED) [124, 143], but to the detriment of simplicity as the frame rate and exposure time are intrinsically related in such techniques. Here, we aim to increase the time between frames of the imaging system with the attempt of keeping the exposure time unaffected. This can be accomplished through the generation of a controlled group delay between the pulses to obtain a larger but still adjustable temporal

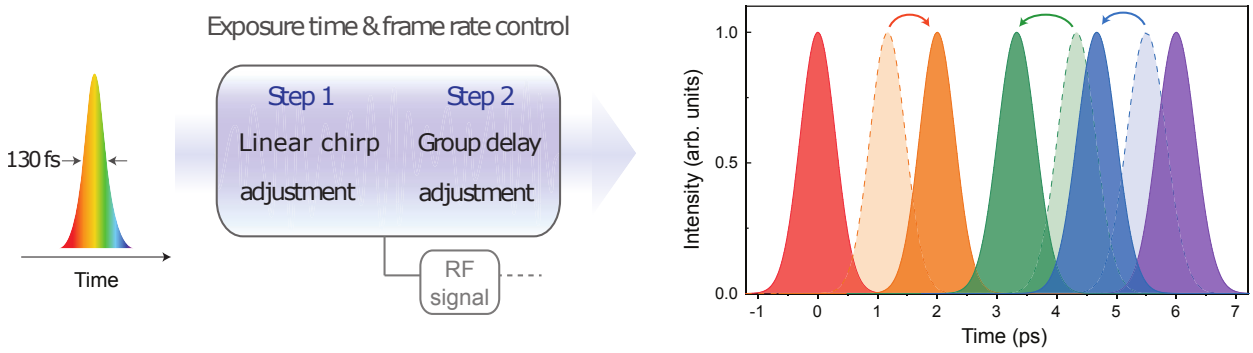

Figure 5.16: **Control of exposure time and frame rate.** Spectro-temporal distributions of the illuminating pulses: Exposure time and frame rate can be independently controlled by adding a linear chirp and adjusting the group delay of each spectral component, respectively. The arrows correspond to the group delay effect on the sub-pulses.

window. This way, the ratio between the exposure time and the time between frames of the imaging system is reduced to a minimum.

5.2.5.4 Extension of the observation window to the nanosecond time scale

For the purpose of extending the observation window to the nanosecond time scale, we propose

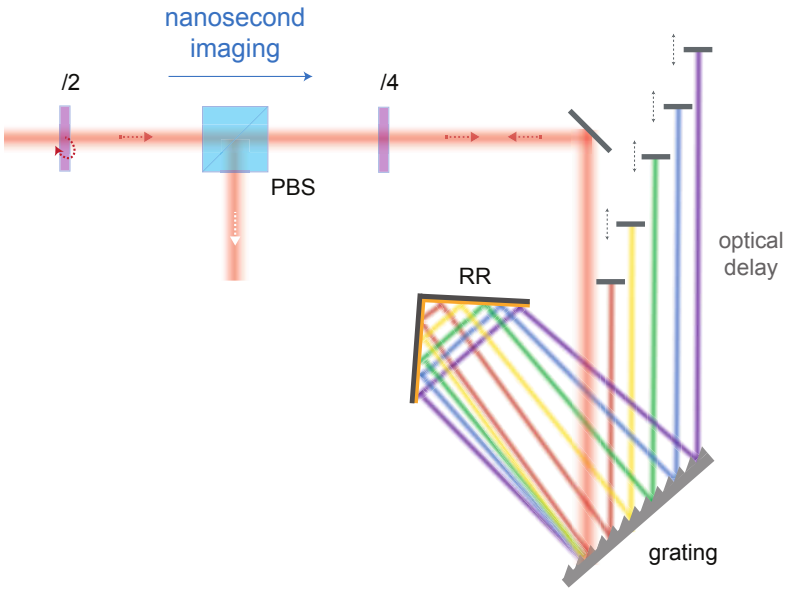

Figure 5.17: **Extension of the system to the nanosecond time scale** through the use of a modified single-grating compressor. PBS: polarized beamsplitter, RR: retroreflector.

the optical system shown in Fig. 5.17 to be set prior to the AOPDF. This system is a modified single

grating pulse compressor and uses a diffraction grating and a roof retroreflector mirror in order to spatially separate the spectral components of the laser pulse into a spectral layer. The spectral bands of the five sub-pulses are then reflected back to grating after crossing different path lengths to create a group delay between them, while the grating together with the roof mirror collects the spectral components of the laser pulse. As a result, the initial spectral phase of the pulse is modified prior to the acousto-optic filtering and therefore adds up to the phase of the diffracted pulse after the AOPDF, as stated in Eq. 5.29. The modified single grating pulse compressor affects the spectral phase of the laser pulse in two ways: *(i)* it creates a group delay between predefined spectral bands of the laser pulse, *(ii)* it also induces a negative group velocity dispersion (GVD) as an ordinary single grating compressor. The group delay is defined by the path length difference between the predetermined spectral bands while the GVD is determined by the grating density as well as the distance between the grating and the roof mirror. These two parameters also define the length of the spectral layer which should be sufficient so that each spectral band of interest is individually reflected.

Other compressor configurations using multiple gratings can also be used to produce the same results. However, it is simpler to use a single grating as it is easier to align, has a more compact structure and insures a good beam profile and compression ratio [158].

5.3 Demonstration of acousto-optically driven ultrafast imaging

5.3.1 Experimental setup

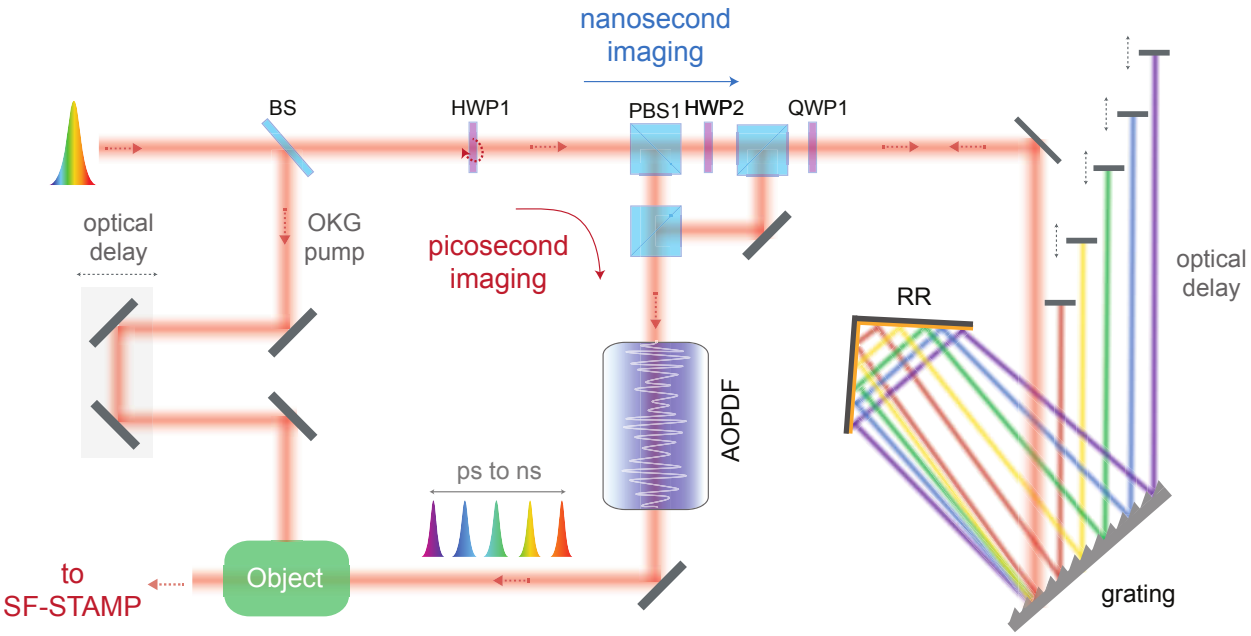

Figure 5.18: **Full experimental setup.** An half-wave plate (HWP1) allows to either operate the system in the picosecond or nanosecond regime.

The general AOPDF-based SF-STAMP setup we developed to access different temporal resolutions is shown in Fig. 5.18. We used a chirped pulse amplifier (CPA, Coherent Inc.) to generate linearly-polarized 100 fs pulses centered at 800 nm with a 10 nm bandwidth (FWHM) at a repetition rate of 1 kHz. The generated laser beam has a diameter of 3 mm with an average power reduced to a maximum of 30 mW in order to avoid damaging the AOPDF. A half-wave plate (HWP1) is used to operate the imaging system either in the picosecond or the nanosecond regime through the free space optical circulator. The latter is made of 3 polarizing beamsplitters (PBS) that are set so that when the beam exits toward the AOPDF, its polarization is orthogonal to the diffraction plane of the acousto-optic crystal. In the picosecond regime, the half-wave plate HWP1 is rotated so that the laser beam goes directly toward the AOPDF in order to create five pulses with equal intensities, equal time delay between them and with specifically selected central wavelengths and spectral widths. In the nanosecond regime, the half-wave plate is rotated so that the laser beam exits the PBS toward the nanosecond extension. A quarter-wave plate (QWP1) ensures that the returning beam exits the PBS toward the AOPDF. As stated earlier, the nanosecond extension consists of a modified single grating compressor where the laser beam is diffracted by a 600 lines/mm grating set at an angle of 45° with respect to the incoming beam optical axis. The first-order diffracted beam is sent back to the grating by a roof mirror reflector set 300 mm away from the grating. This provides a GVD of -1.28 ps/nm. The five selected spectral bands are then reflected back to the grating using five mirrors placed 375 mm apart. The first mirror reflects the spectral band up to 790 nm while the rest is left to propagate toward the remaining mirrors. In ascending order, these mirrors reflect the spectral bands up to 800 nm, 807 nm, 811 nm and the last mirror reflects the remaining of the spectrum. A group delay of 2.5 ns between the sub-pulses is then obtained prior to injection to the AOPDF. Here, the spectral widths and central wavelengths of the five sub-pulses can be finely tuned in order to avoid any spectral overlap by the SF and their respective intensities can also be equalized. Finally, the GVD induced by the modified single grating compressor can be compensated to a certain limit in order to compress the five pulses as close to their Fourier limits as possible.

Before the AOPDF, the beam diameter was reduced to 1.6 mm with a divergence inferior to 0.04° in order to maximize both the resolution and efficiency of the pulse shaping system. The shaped pulse eventually exits the acousto-optic crystal at an angle of 1.4° with respect to the input pulse. The next two sections are dedicated to the demonstration and validation of this system on two different timecales, first in the ps regime and then in the ns regime.

5.3.2 Imaging ultrafast phenomena in the picosecond regime

The temporal capabilities of ultrafast systems are usually validated by imaging femtosecond- or picosecond-scale light-induced phenomena such as the propagation of a pump pulse through a nonlinear medium. In order to demonstrate that our flexible technique is on par with state-of-the-art active imaging methods, we then used our system to capture the opening and closing of

a CS_2-based optical Kerr gate (OKG). The OKG was also used as a reference for the temporal characterization of the imaging system in the picosecond time scale.

As indicated by its name, the OKG is solely based on the optical Kerr effect (OKE) in a nonlinear medium of which the refractive index is modulated by the intensity of an intense electric field propagating through it. The most used medium to achieve a measurable OKE is CS_2 (carbon disulfide). It is made of linear molecules that are naturally randomly orientated and when exposed to a strong external electromagnetic polarized field, that tend to adopt the same orientation, thereby inducing a birefringence [159].

In an OKG setup, a transparent medium with a high nonlinear refractive index (liquid CS_2 here) is placed between two crossed polarizers along the optical axis of an image beam. An intense ultrashort pump pulse is then used to induce birefringence in the transparent nonlinear medium so that the polarization of the image beam is changed from linear to elliptic. Therefore, a portion of the image beam is transmitted through the second polarizer. The duration of this pump-induced birefringence (i.e. the time gate) depends on the pump pulse duration along with the relaxation time of the nonlinear medium. Therefore, its duration is larger than the duration of the pump pulses. Yet, it is still considered as an ultrafast phenomenon that takes place in few picoseconds. As a result, OKGs are routinely used as simple and efficient time gates e.g. for capturing ballistic photons (and reject multi-scattered photons) in ultrafast imaging experiments [160].

5.3.2.1 Temporal characterization of the SF-STAMP system using an OKG

In our case, the acousto-optics filtering results in the generation of 5 independent temporally separated sub-pulses. When these pulses are used as a probe for the OKG, the OKG transmittance for each of the five sub-pulses is identical. Yet, it is delayed in time with a delay corresponding to the time between the sub-pulses (time between frames). Using a pump-probe experiment, the time difference can be easily obtained using cross-correlation on the resulting transmittance curves of the OKG for each of the five sub-pulses. When the time separation between the sub-pulses is obtained, it is used along with their corresponding central wavelength to estimate the accumulated dispersion parameter D using a first order linear regression. Once the accumulated dispersion D is determined, knowing the optical spectrum, we are able to obtain the pulse width (exposure time, ET) of each of the five sub-pulses using Eq. 5.1. In our experiment, the femtosecond laser pulse was linearly polarized and split by a 90/10 beamsplitter prior to the pulse shaping stage. 90% of the power was used as a pump while the rest was directly injected into the AOPDF. At the output of the AOPDF, we obtained five linearly polarized pulses with equal intensities and temporal and spectral separations as discussed in the previous section. This beam was enlarged to a diameter of 3 mm by a lens telescope. The telescope was made of a diverging and a converging lens (with $f_1 = -75$ mm and $f_2 = 150$ mm) set 75 mm apart along the optical axis. A CS_2 cell and a single polarizer were eventually set between the telescope and the lensless SF-STAMP as a Kerr time-gate. The pump pulse was synchronized with the image pulses via an optical delay line and a cylindrical lens ($f = 75$ mm) was used in order to focus the pump beam within a single axis

(vertical) inside the 10×10 mm CS_2 cell at an angle of 42° with respect to the image beam. The image beam size was reduced (using a pinhole) to limit the spatial interaction in the CS2 cell with the pump beam for the temporal characterization. The transmittance of the OKG for each of the image pulses is measured as a function of the delay between the pump and the image pulses. It is represented by the floored summation of the measured intensity on the pixels of the CCD sensor at the location where each sub-pulse hits. The phase induced by the acousto-optic interaction in the crystal is represented as a Taylor expansion up to the 4^{th} order:

$$\phi_{AOPDF} = \sum_{i=1}^{4} -(\frac{a_i}{i!}(\omega - \omega_0)^i) \tag{5.31}$$

Where ω_0 is the central frequency, a_1 represents the group delay while a_2, a_3 and a_4 represent the 2^{nd}, 3^{rd} and 4^{th} orders of the phase, respectively. Using the Dazzler software, these coefficients can be adjusted in order to control the induced phase. The acoustic wave and the light pulse are then synchronized to interact within the AO crystal. The group delay is set so that the acoustic frequency phase-matched with the central wavelength of the input pulse is located at the center of the crystal at the moment of interaction. The coefficient a_2 is set so that the acoustic wave is spread along the crystal to induce a linear variation of the instantaneous frequency of the input pulse, but also to increase the interaction length between the acoustic wave and the optical pulse, which implies the increase of the diffraction efficiency of the AOPDF. For the 25 mm long crystal, the maximum value of the coefficient a_2 is around 60000 fs^2 for a bandwidth of 25 nm. At this value, the acoustic wave extends along the total length of the crystal and it determines the total observation window of the SF-STAMP imaging system. For the OKG imaging, the total observation window needs to be adapted so that it is sufficiently large to capture (in a single shot) the gate opening on the first sub-pulse while the gate closing is captured on the last sub-pulse. The total observation window of the SF-STAMP imaging system is expressed as:

$$\Delta T_{window} = D.(\lambda_5 - \lambda_1) \tag{5.32}$$

The coefficient a_2 is set to a value of 20000 fs^2, 40000 fs^2 and 60000 fs^2. For each case, the transmittance of the OKG for the image pulses is measured as a function of the inter-pulse delay and the pump pulse. On the one hand, the transmittance of the OKG is shown in Fig. 5.19c,a(bottom) and d for the three values of a_2 in ascending order. On the other hand, Fig. 5.19a(top) shows the images of the OKG as a function of the delay between the pump and the image pulse train for $a_2 = 40000$ fs^2. In this case, the time between frames is further adjusted by adding a positive or negative group delay to the 2^{nd}, 3^{rd} and 4^{th} pulses to equalize the time separation between our five pulses. This evidently does not affect their pulse duration. Using the same pump probe CS_2 experiment, we can define the time separation between the five pulses and after few iterations, we obtained a quasi-constant time between frames as shown in Fig. 5.19b(bottom), while the corresponding images are shown on Fig. 5.19b(top).

In this case, the estimated value of the accumulated dispersion is $D = 0.269$ ps/nm which

yields to an average exposure time $ET_{average} \sim 723$ fs. In addition, the group delay adjustment led to a time between frames of 2 ps between the two first images and 1.33 ps between the next ones.

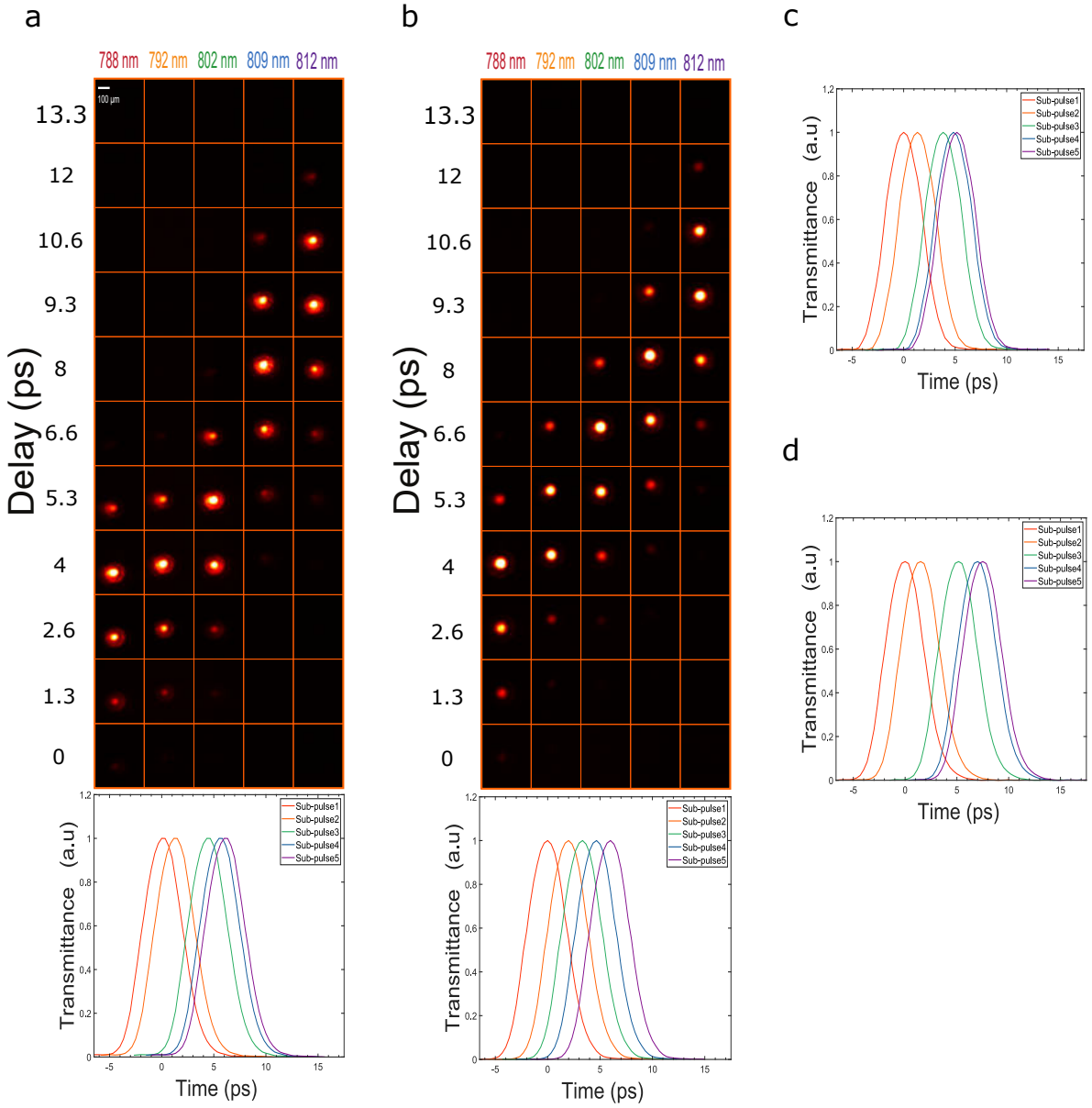

Figure 5.19: **Temporal characterization of the system.**

When operating in the nanosecond time scale, the total accumulated dispersion amounts to $D = 1.01\ ps/nm$. Therefore, the average pulse duration in this case is $ET_{average} \sim 2$ ps. As for the time between frames, it was precisely adjusted to 2.5 ns using fast photodiode and oscilloscope as shown in Fig 5.20.

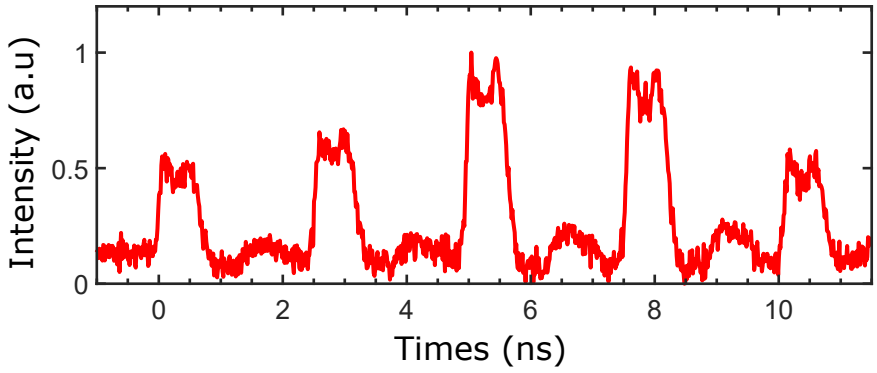

Figure 5.20: **Time between frames** in the nanosecond regime.

5.3.2.2 Ultrafast imaging of an optical Kerr gate

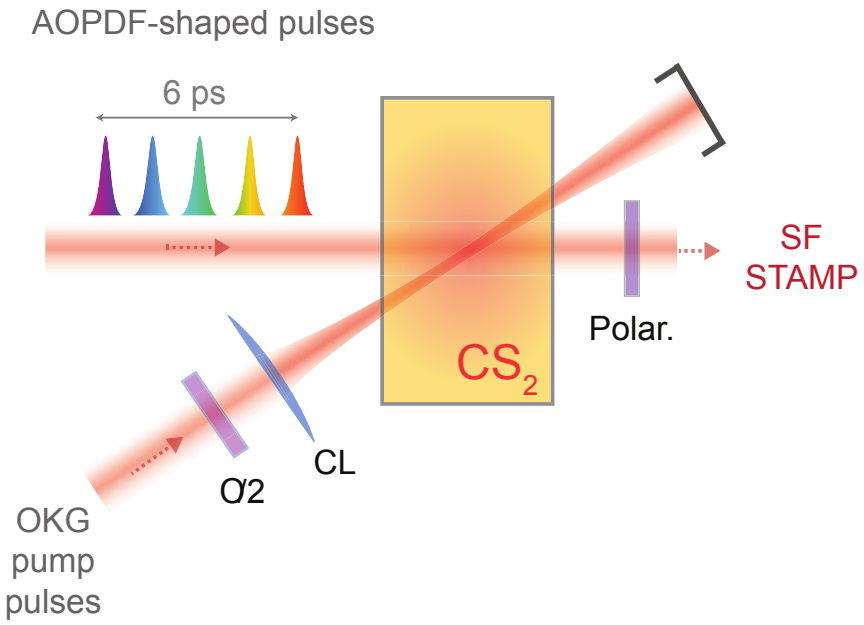

Figure 5.21: **Experimental configuration** used for the picosecond-scale imaging of an optical Kerr gate (OKG) in a CS_2 cell. An optical delay line is used to synchronize the pump pulses with the imaging pulses in the CS_2 cell and to precisely capture the Kerr gate dynamics.

After the temporal characterization of our imaging system, we then used it to capture the whole OKG process using the same setup. The only change was to remove the pinhole from the image beam trajectory as shown in Fig. 5.21. This leads to the image beam becoming larger than the pump beam and then able to capture the full OKG along with its spatial displacement in time. For each optical delay, the imaging system then captures five single-shot images of the OKG, as shown in Fig. 5.22a where the images are displayed as a matrix in which the rows represent the single-shot images while the columns represent the group optical delay. For a delay of 6.6 ps, the five frames

capture the whole pump-induced process, from the opening to the closing of the time gate. An horizontal spatial displacement of the intensity can also be noticed, which corresponds to the propagation of light within the CS_2. In order to further confirm the ability of our system to provide accurate measurements, the propagation of the pump and imaging pulses within the CS_2 cell have been simulated using a validated standard model [160]. The latter allows to predict the transmitted light from the polarizer as a function of the pump and image pulses parameters by modeling the CS_2 response using a single relaxation process (see "appendix" section). The simulated snapshots for each spectral component, in full agreement with the experimental measurements, are shown in Fig. 5.22b and then fully validate our AOPDF-based imaging technique.

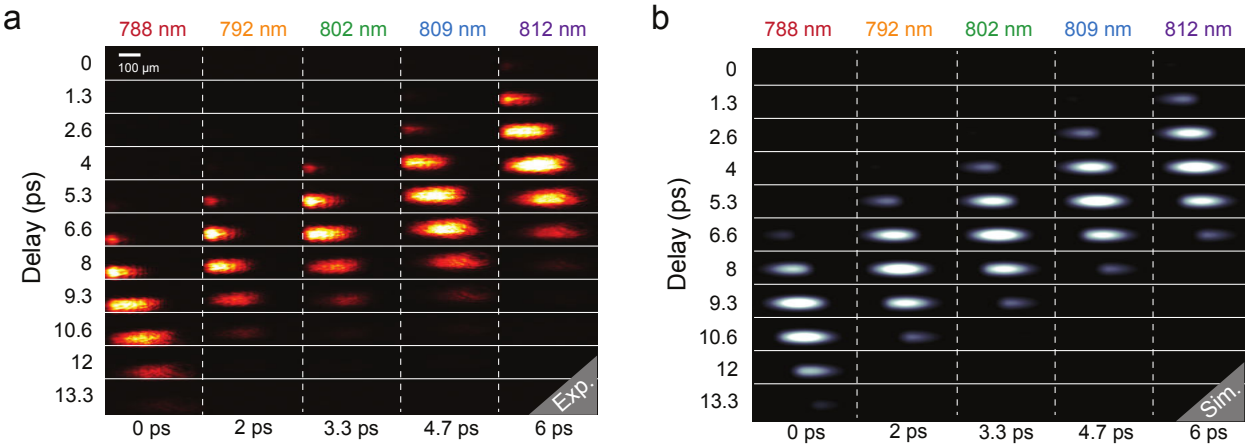

Figure 5.22: **Ultrafast imaging of the Kerr gate.** a) Vertically-stacked images of the transmitted pulses while varying the optical delay. The opening and closing of the OKG are fully acquired for a delay of 6.6 ps. b) Numerical simulation of the OKG imaging process.

5.3.3 Imaging ultrafast phenomena in the nanosecond regime

5.3.3.1 Laser-induced ablation dynamics

Numerous laser-matter interaction phenomena also occur in the nanosecond time scale, such as laser ablation. This process is essential for various applications such as laser-induced breakdown spectroscopy (LIBS), material treatment, micro machining or the synthesis of nanoparticles, to name a few. The aim of this section is to highlight the versatility of our system by validating its nanosecond scale imaging capabilities via the tracking of laser-induced ablation dynamics.

Laser ablation is a complicated process that is mainly based on the focusing of intense laser beam on a target material for removing a certain portion of its surface. Meanwhile, the gas above the surface experiences several dynamic processes as a result of the interaction of the intense laser pulse with the target. These processes have a great impact on the end result of the laser ablation process and we then aim here to visualize such laser-induced gas dynamics in the nanosecond time scale. For this purpose, the same optical setup as in Fig. 5.18 is used while adjusting the observation window of the SF-STAMP system to cover a temporal range of 10 ns. This is accomplished through the rotation of half-wave plate (HWP1) as explained in the experimental setup section. Laser

ablation is performed by focusing 532 nm nanosecond pulses on solid samples using a lens with $f = 12$ mm. As a result, a shock wave (SW) is created and captured by our 5 sub-pulses with a time between frames of 2.5 ns. The lensless configuration of the SF-STAMP leads the CCD sensor to capture the shock wave-induced fringes pattern shown in Fig. 5.23. By applying the propagation

Figure 5.23: **Capture of shock waves via lensless AOPDF-based SF-STAMP.** Raw image corresponding to the hologram of the object of interest.

model described in section5.2.3 along the optical axis of the image beam, the complex image of the shock wave can be reconstructed when the right reconstruction distance is reached. The resulting real and imaginary parts of the reconstructed complex image of the shock wave are shown in Fig. 5.24b and Fig. 5.24c, respectively. The numerical reconstruction distance is found to be 250 mm and matches the measured distance between the CCD sensor and the plane at which the shock wave is generated. This reconstruction distance is calculated considering a 40×40 pixels area

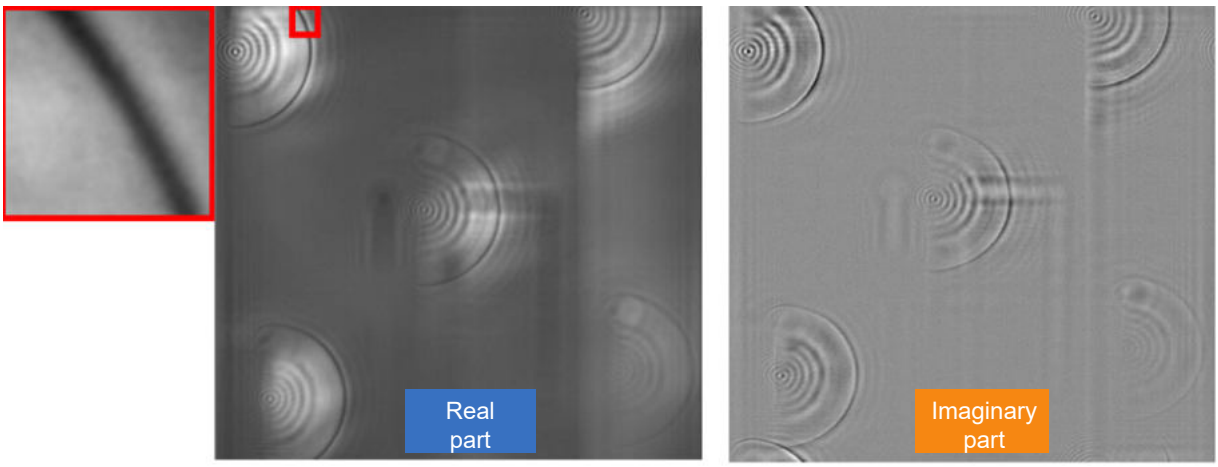

Figure 5.24: **Object reconstruction** using a digital in-line holography model.

(red rectangle on Fig. 5.24b, enlarged in Fig.5.24a) where the front of shock wave is supposed to exist. After the reconstruction, a circular front with a high contrast appears, as shown in Fig. 5.24a. Although the reconstruction of the shock wave image was successful, we obtain 5 single shot images on which the shock wave seems to be static. This indicates that even with the enlargement of the observation window by approximately 1600 times, the frame rate is still too high to capture the shock wave in motion in a field of view that covers the area of 4×4 mm^2, considering the limited number of frames. This necessitates either enlarging the window observation even further or reducing the field of view. The first option is deemed complex as it renders the nanosecond extension setup larger and harder to align. Therefore, the lensless SF-STAMP is replaced by a 4f system with a magnification of one where the DOE and SF are placed in between two identical lenses with focal lengths of 50 mm.

In order to access the field of view at which we can observe the laser-induced gas-dynamics, a microscope system comprising a $f = 50$ mm condenser lens and an objective lens ($\times$20, NA = 0.35, Nachet) is constructed. The beam was subsequently enlarged by a factor two using another telescope as shown in Fig. 5.25. The spatial characteristics of the imaging system are determined

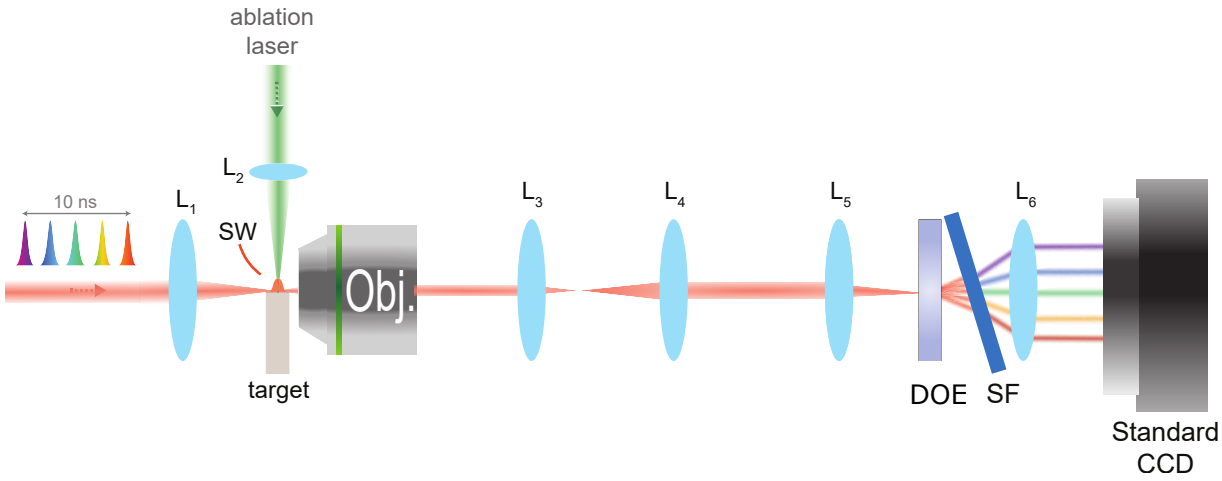

Figure 5.25: **Modification of the experimental setup** in order to capture laser-induced gas dynamics.

using the standard 1951 USAF resolution test target and the resulting image is shown in Fig. 5.26a while Fig. 5.26b shows sample traces of the horizontal and vertical lines from element 3 of the 7^{th} group. Fig. 5.26a shows that the three lines in the 3^{rd} element of the 7^{th} group are clearly distinguishable. The contrast function for these lines can be calculated from the traces on Fig. 5.26b and it yields to a value greater than the limit of 0.1 for both the horizontal and vertical sampled lines (red and blue in Fig. 5.26a). The traces in Fig. 5.26b are also used to determine the magnification of our imaging system, which is found to be 10.18, resulting in a camera resolution limit of 1.67 μm. The imaging system is then used to image the laser-induced gas-dynamic processes due to the intense laser-matter interaction. An example of the obtained images when ablating glass is shown

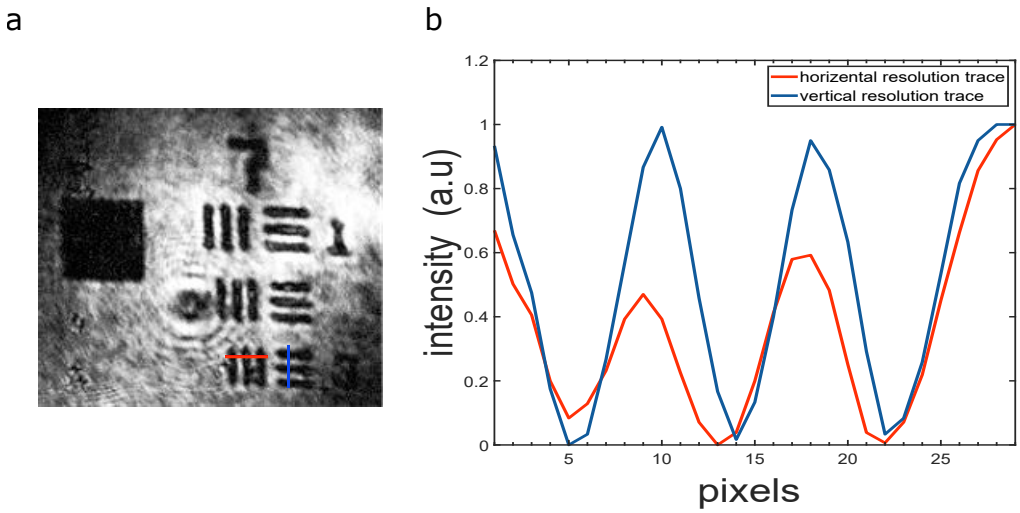

Figure 5.26: **Spatial characterization of the system** using a standard 1951 USAF resolution test target. a) Image of the target (3^{rd} element, 7^{th} group). b) Contrast function.

on Fig. 5.27 along with a schematic representation inspired from [161] that illustrates the different discontinuities arising in the ambient air due to the laser ablation process. As seen in Fig. 5.27,

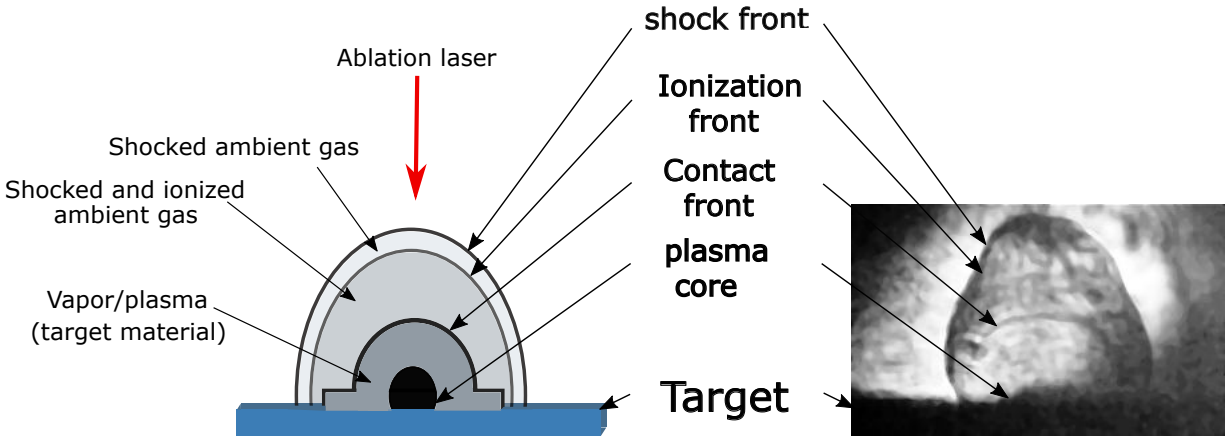

Figure 5.27: **Laser ablation on glass.** a) General representation of the gas dynamics in laser ablation. b) Image obtained using our system.

the laser ablation process results in the creation of a shock front in ambient air propagating in the reverse direction to the pump pulse. It also creates an ionization front closely backing the shock front. Behind it, a contact front containing a dark area of plasma/vapor develops to be followed by an even darker area corresponding to the plasma core.

Using our imaging system, we could observe the birth and development of these discontinuities in time, as shown in Fig. 5.28. The resulting dynamics can be explained as follows [162]. When the intense laser pulse illuminates the area of ablation, it causes its liquefaction and evaporation. The high velocity of the evaporated material into the ambient air leads to its compression in a thin shell.

Therefore, a strong nearly-transparent external shock front is formed. The external shock front is almost attached to an ionization front that consist of shocked and ionized air. Afterwards, the ablated material produces a contact front with a planar shape confining vapor and plasma from the target material, and the composition of the confined gas explains the contrast of this region with respect to the air confined by the external shock wave. The possible existence of plasma ions and free electrons leads to a high absorption of light and, in addition, the high-density vapor can contribute to this contrast. Finally, an even darker region with a planar shape is created above the ablated area defining the plasma core.

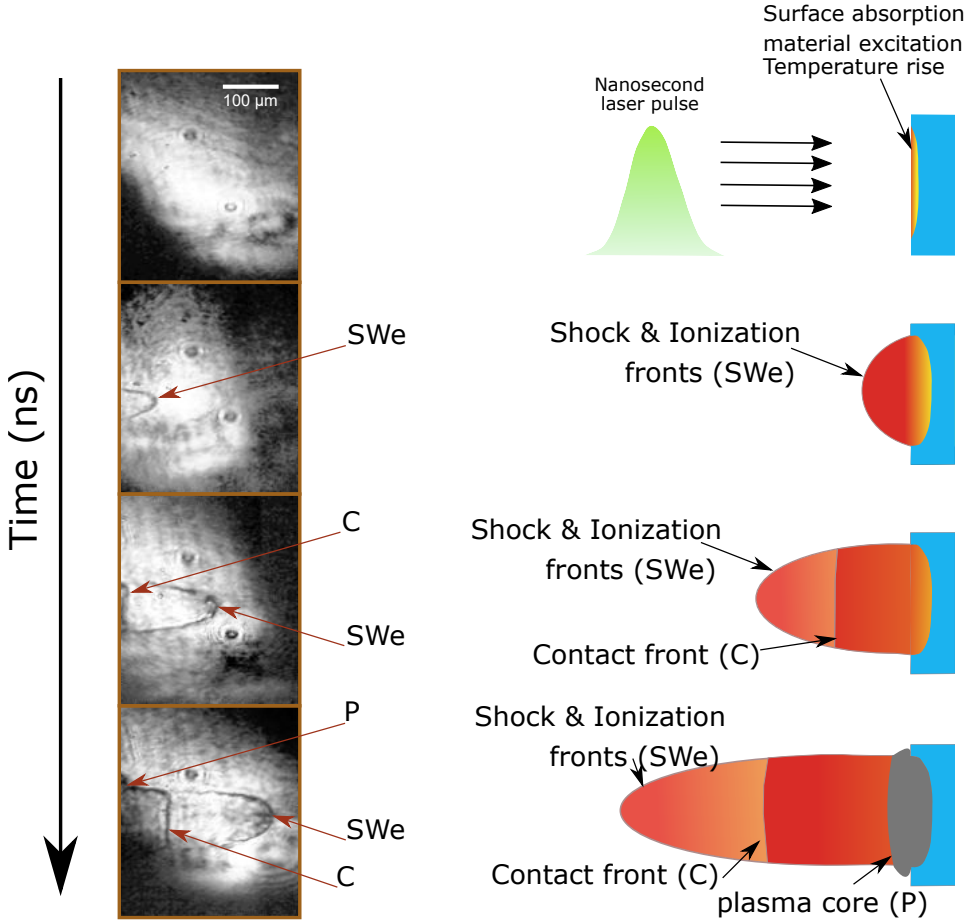

Figure 5.28: **Birth and evolution of laser-induced discontinuities.** Images obtained using our experimental technique and corresponding physical phenomena.

5.3.3.2 Laser-induced gas dynamics: parametric study

The dynamics of the discontinuities resulting from laser ablation are influenced by several parameters such as the laser energy, the irradiated area as well as the target material. We then a performed a parametric study where we study the individual influence of each of these parameters on the

laser-induced gas-dynamic processes. The aim of this study is to fully validate our method in order to eventually use it as an ultrafast tool for the plasma physics community.

Pulse energy

The incoming laser energy is known to influence the velocity of propagation of the laser induced discontinuities in the atmosphere surrounding the ablated area. Therefore, we performed 7 laser ablation experiments on glass where the laser energy is gradually increased. The results are shown in Fig. 5.29.

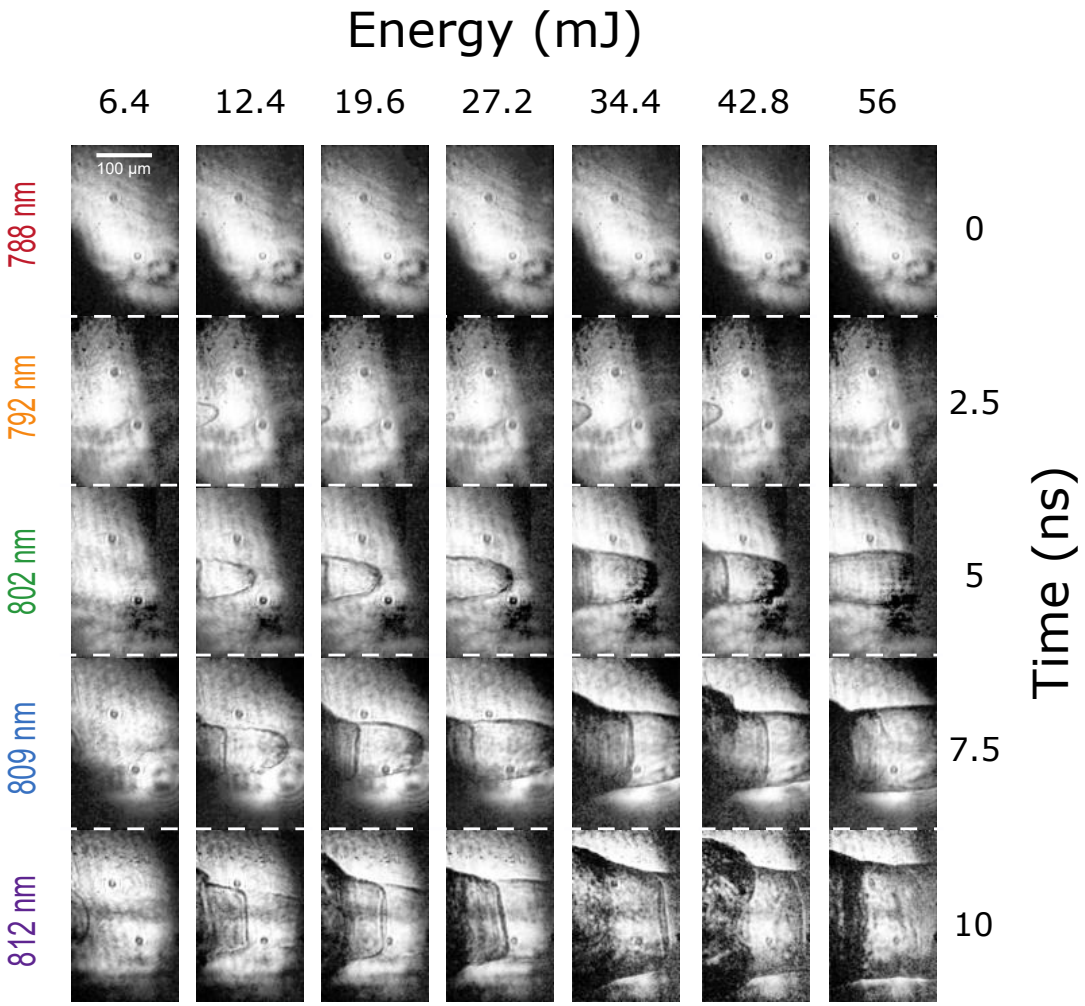

Figure 5.29: **Influence of pulse energy** on the laser-induced gas dynamics.

The pump laser was focused in air at a distance of 60 μm from the glass target. At a pulse energy of 6.4 mJ, we barely exceeded the ionization threshold and a relatively slow moving shock wave is created. As the pulse energy is increased, the birth of the discontinuities occurs faster after the illumination of the ablated area. The propagated distance of the discontinuities increases as well with the increase of the pulse energy. However, their shape remains relatively the same. At a pulse energy of 12.4 mJ, the five snapshots were sufficient to capture the creation and movement

of the shock, ionization and contact fronts as well as the plasma core. At higher pulse energies, we notice an increase in the contrast of the plasma core region. In addition, the tip of the shock and ionization fronts travel beyond the field of view of our imaging system after the third snapshot. This limits our capacity to measure the displacement of the shock and ionization fronts as a function of laser pulse energy to a time interval of 2.5 ns after their creation. The results are plotted in Fig. 5.30a while Fig. 5.30b shows the distance vs energy diagram of a similar study from [161]. In the latter, copper and aluminum were ablated using an excimer laser at different pulse energies while its influence on the radius of the shock front was measured on a time interval of 80 ns. Fig. 5.30b also compares the experimental results with a theoretical model that is used to predict the velocity, density and pressure distribution in the region that follows the shock front (Sedov theory). By comparing the measured displacements of the shock front in Fig. 5.30a with

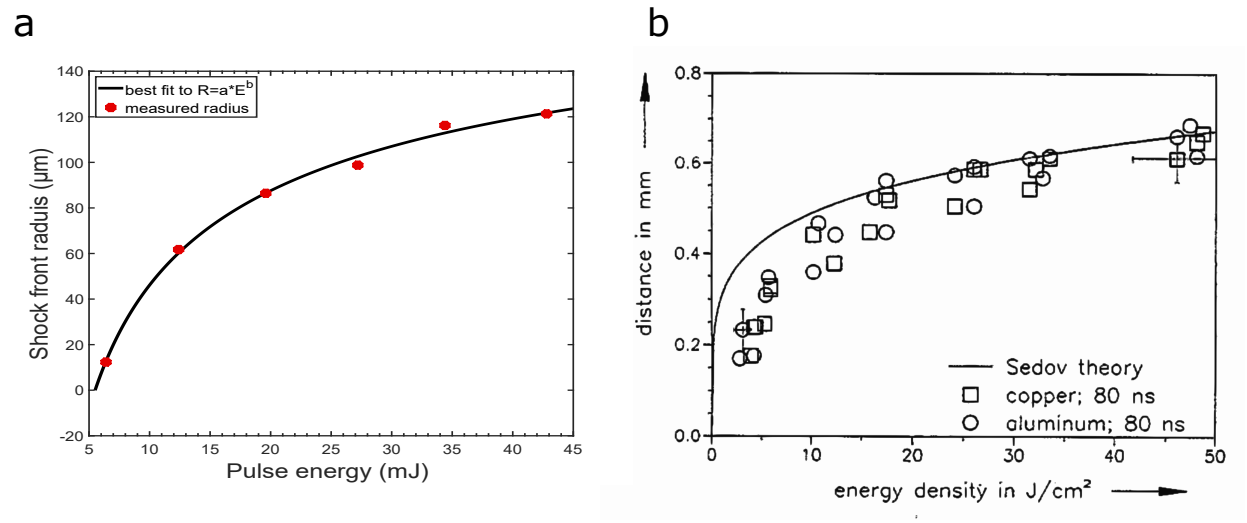

Figure 5.30: **Evolution of the laser-induced shock front as a function of energy.** a) Experimental results. b) Results reproduced from Ref. [161].

the trace of the theoretical model in Fig. 5.30b, we can clearly see that the influence of the pulse energy on the displacement of the shock front is in agreement with the theoretical predictions ($R \propto E^b$). As stated earlier, the pulse energy needs to exceed a threshold value to create the laser induced discontinuities in the atmosphere surrounding the irradiated area. Initially, the increase of the pulse energy beyond the threshold value increases the velocity of the shock front. A further increase in the pulse energy leads to a lesser increase in the velocity of the shock front, which indicates the decrease in the pulse energy influence on the propagation of the shock front.

Focusing conditions

Another parameter that influences the laser-induced discontinuities is the size of the irradiated area on the target material. To study this influence, the laser pulse energy is set to 28 mJ while the position at which the pump laser is focused relatively to the glass target surface is gradually changed. Initially, the focus was set 220 μm within the glass target. Afterwards, this distance

was gradually reduced by a 40 μm step until it reached a distance of 60 μm with respect to the target surface. At every position of the focus, single shot measurements of the laser induced discontinuities were taken and the resulting images are shown in Fig. 5.31.

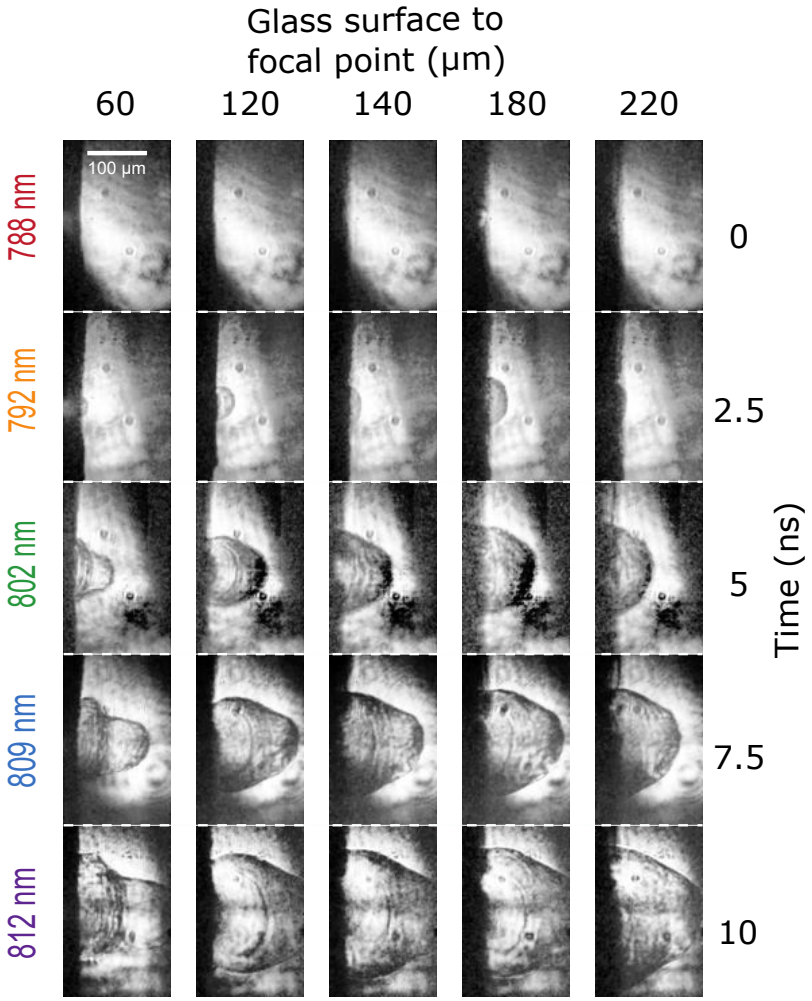

Figure 5.31: **Influence of the focusing conditions** on the laser-induced gas dynamics.

Fig. 5.31 shows that the velocity of the shock front does not evolve significantly with the change in the size of irradiated area. However, its geometrical shape tends to have a greater radius in the horizontal direction when reducing the size of illuminated area. This causes its shape to shift from an ideal hemisphere (focus at 220μm within the target) toward an ellipse (focus at 60μm within the target). This also leads the contact front and the plasma core to extend beyond the boundaries of the shock front.

Target material

We performed laser ablation on copper, aluminum and glass to attest of their influence of the laser-induced dynamics. The laser pulse was focused at a distance of 220 μm within the target materials while the pulse energy was set to 28 mJ. Fig. 5.32 shows that the influence of the target

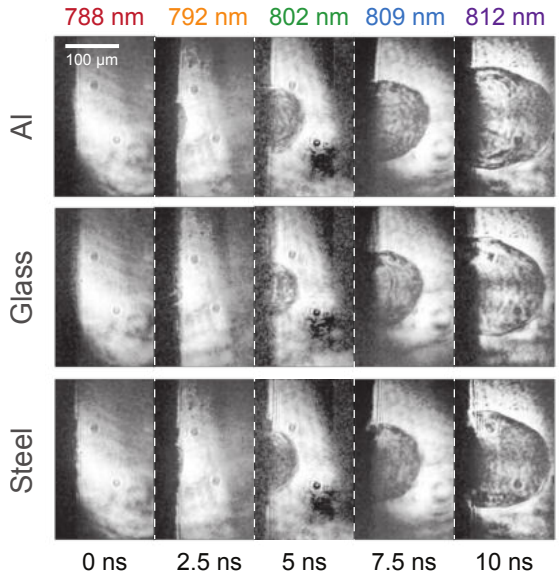

Figure 5.32: **Influence of the target material** on the laser-induced gas dynamics.

materials on the shape and velocity of the laser induced discontinuities is insignificant in this time frame (SW average velocity = 16.26 km/s). Fig. 5.30b also supports this result as the diameter of the shock front generated by ablating aluminum is quite similar to the one generated by ablating copper for the same pulse energy. However, when we compare the laser induced discontinuities created by ablating glass compared to the other targets, we can see in the last snapshots that the plasma core is smaller in size and less dark. This might be the consequence of the roughness of the ablated surface.

5.3.3.3 Laser-induced air breakdown

During the previous experiments, when the pump laser was focused in the air relatively far from the surface of the target, we occasionally observed shock waves that were created in the air in what is known as laser-induced air breakdown. We noticed that these shock waves propagate considerably faster than those created through laser ablation. An example of these shock waves is shown on Fig. 5.33. For this reason, we decided to image the laser-induced air breakdown phenomenon using the lensless SF-STAMP configuration in the hopes of capturing a dynamic scene of this rather random process. Such a physical phenomenon that can be explained as follows. When the pulses are focused within a small volume, it initiates laser-accelerated electrons through a multiphoton ionization process, leading to successive cascaded ionizations of the medium by inelastic collisions. This eventually results in the formation of a plasma expanding asymmetrically toward the pump laser [163]. Here, the laser source used for ablation resulted in air breakdown when the laser beam was focused in air. However, this phenomenon occurred in a random manner and required having the target at a given distance from the focal point of the pump beam. This indicates that the process necessitates the existence of a seed electron in the focal volume of the

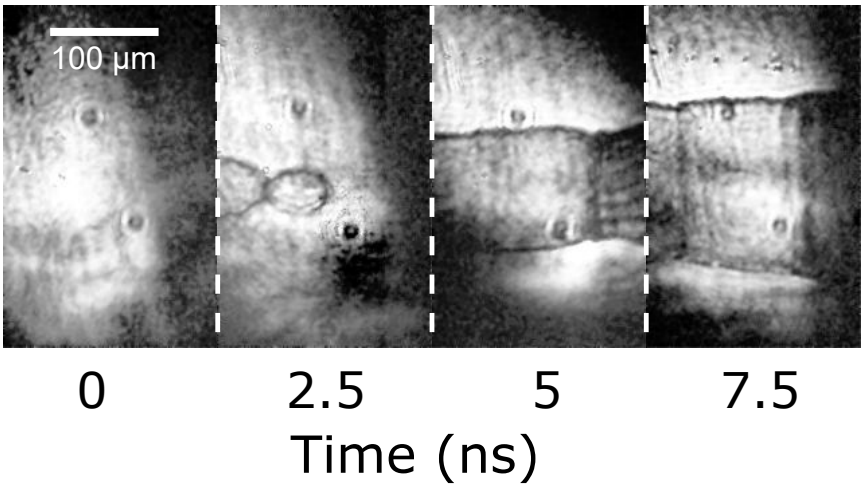

Figure 5.33: **Shock wave obtained by laser-induced air breakdown** and captured using of imaging system.

laser for it to occur. To eliminate this randomness, we decided to pump with a different laser source that can deliver pulses with higher energies so that it generates air breakdown with every pulse when focused and without having a target on its trajectory. We then used a 1064 nm Nd-YAG laser delivering 6 ns pulses with a pulse energy up to 850 mJ. Using our lensless SF-STAMP system, the CCD sensor captures the hologram shown in Fig. 5.34a. Note that this hologram was simply normalized by the background intensity distribution previously recorded without the plasma excitation beam. From this hologram, the complex amplitude can be reconstructed in any plane along the optical axis using the propagation model explained in section5.2.3, as shown in Fig. 5.34b, where the real and imaginary parts of the amplitude are displayed. In this experiment, the Nd-YAG laser was focused (using a lens with $f = 20$ cm) to generate laser-induced air breakdown, which manifests as the specific patterns shown in Fig. 5.34b. This type of pattern has been observed using classical burst imaging techniques in the ps regime [141], which only allows to visualize one state of this process (corresponding to the second snapshot in Fig. 5.34b). Here, the birth and growth of this pattern can clearly be seen in the consecutive snapshots in the reconstructed images obtained through the lensless AOPDF-based technique. From these real and imaginary part images, the phase can also easily be calculated using $\phi(x, y) = arctan(Im(x, y)/Re(x, y))$, as shown in Fig. 5.34b. Remarkably, calculating the phase is an efficient way to precisely determine the axial coordinate z at which the object of interest (here, the highest electron density region) is located using the following procedure. From the complex amplitude images, the phase images are calculated at every axial coordinate and stacked horizontally in order to plot an orthogonal view of the phase map such as the one shown in Fig. 5.34c. The phase profile along the optical axis (red solid line) exhibits a typical shape that has been observed previously [164], which is a clear signature of the object position and then gives a simple and efficient tool for an accurate focusing on the best-reconstructed image.

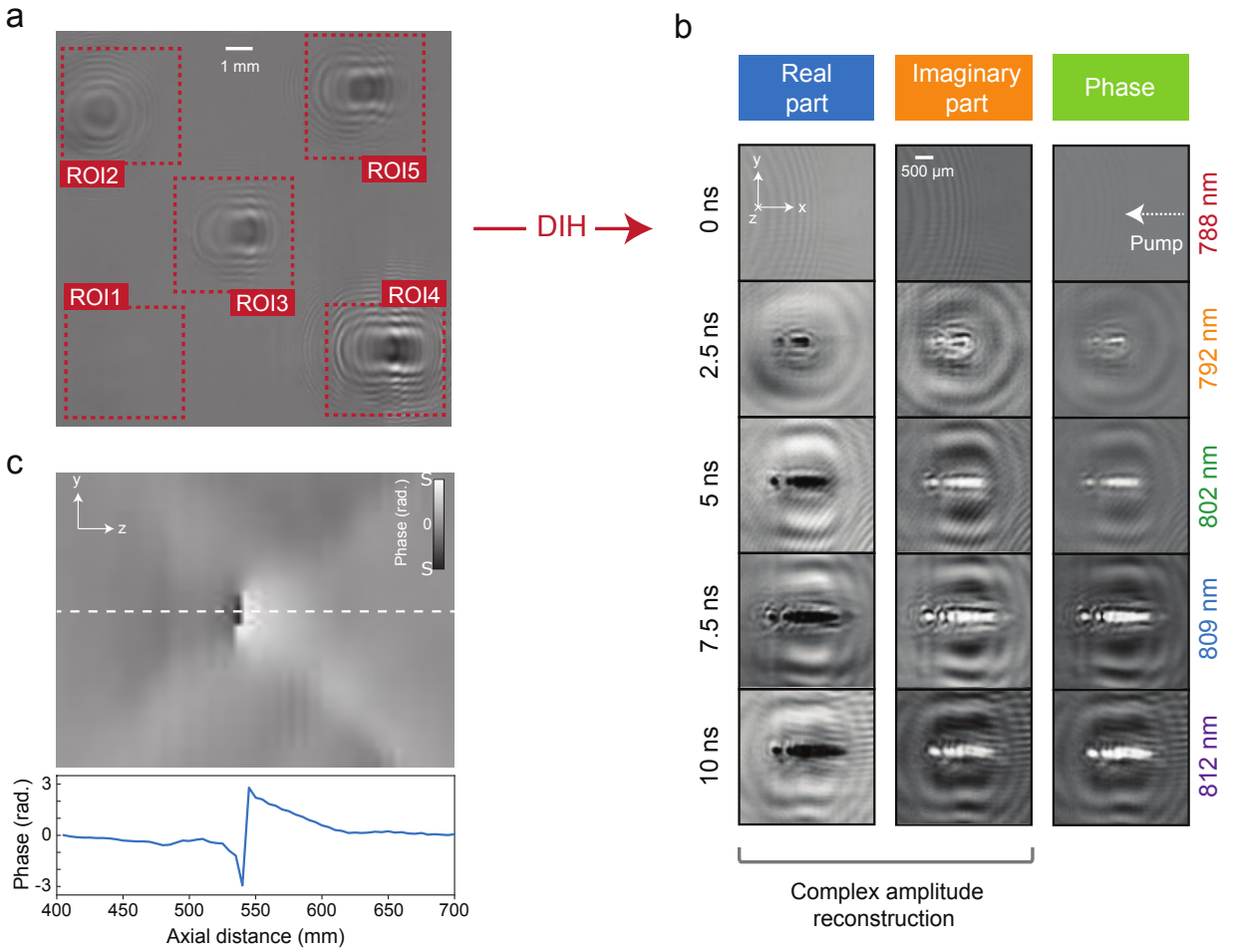

Figure 5.34: **Image reconstruction using digital in-line holography (DIH).** The concept of lensless AOPDF-based SF-STAMP based on DIH is demonstrated by imaging laser-induced air breakdown on the ns scale. **a** Hologram normalized by background subtraction. **b** Complex amplitude and phase reconstruction using DIH (based on the hologram of **a**). The image is reconstructed at an axial distance z_r = 550 mm and the asymmetrical plasma expansion is clearly seen. **c** Phase map along the longitudinal axis obtained by reconstructing the complex amplitude and calculating the phase at different longitudinal coordinates. The selected zone of interest is the leftmost spot in the air breakdown pattern in **b**. The phase variation along the optical axis (blue solid line) is a striking signature of the actual location of the intensity and phase object.

5.4 Conclusions

5.4.1 Limitations and potential enhancements

The AOPDF-based SF-STAMP technique on which relies our system has proven efficient for capturing ultrafast events in a simple and user-friendly manner. However, we have seen that its sequence depth (i.e. the number of images acquired in a single-shot) is intrinsically limited by two factors. On the one hand, as it exploits bandwidth-limited laser pulses together with a spectrum sampling process, having a larger number of images would necessitate the filtering and separation of very narrow adjacent spectral bands, which is feasible but could require a more complex setup. In that case, a specific attention should be paid to the potential temporal overlap between the extracted spectral bands. On the other hand, the number of images is also limited by the spatial separation of the sub-pulses (through the DOE and tilted spectral filter) prior to the acquisition on the CCD sensor. As a single CCD sensor is used, the larger the number of images, the lower the number of pixels per image and, consequently, a compromise between the sequence depth and the spatial resolution has to be found. With a view to provide a compact and simple system, the above-mentioned drawbacks could be easily suppressed using several technical solutions leveraging the AOPDF spectro-temporal tailoring capabilities, as it allows the generation of adjacent non-overlapping narrow (sub-nm) spectral bands. It would then be possible to use a broadband fiber laser as the illumination source to increase the number of shaped sub-pulses and an hyperspectral camera to replace the DOE, spectral filter and CCD sensor at once. The number of images would therefore be determined by the number of spectral bands and be independent of the spatial resolution. This would also allow to eliminate the path difference between the sub-pulses due to the DOE that results in a shift along the z-axis when reconstructing the images using DIH.

In this work, the AOPDF-based system exhibits a fixed maximum temporal window of 8.5 ps regardless of the number of images. It is worth noting that longer crystals than the one used in this feasibility demonstration could be used. This would enable larger temporal windows (through larger GDD values) in the picosecond regime. In the nanosecond regime, the temporal window is enlarged using a modified single grating compressor which is however bulky and necessitates a careful alignment. Still in the aim of building a compact alignment-free system, the generation of the additional delay between the pulses could be performed using custom-made fiber Bragg gratings (FBG) adapted to the desired imaging temporal window. Regarding holography, it is clear that a rigorous phase map over the whole field of view cannot be estimated - as in off-axis holography [165] - without a perfectly known reference [166]. It is also worth noting that the phase distortions in an in-line configuration could be reduced by a phase conjugation technique as shown in Ref. [167]. However, these two potential refinements would entail a much more complex setup, which is out the scope of this study aiming for a user-friendly technique. Here, as far as a small volume is studied around the considered object of interest, in-line holography is completely satisfactory provided that the local wave front variations remain acceptable for extracting an exploitable phase signature, as shown in Fig. 5.34.

5.4.2 Summary

By leveraging the AOPDF's pulse shaping capabilities within a burst imaging scheme, our single-shot technique stands out of the current state-of-the-art as its main features are easily controllable and adjustable through a simple electrical signal. The outcomes of this feasibility demonstration are manifold and could now help to bring such ultrafast techniques out of a laboratory environment.

(i) The AOPDF acts as an "all-in-one" compact and flexible device that can tailor the phase and/or the amplitude of the input signal on a wide range of pulse duration and chirp values. Unlike most of the existing techniques presented in the introduction of this chapter, the frame rate and exposure time can here then be independently adjusted without resorting to complex or bulky spectro-temporal shaping stages.

(ii) The technique can be easily switched between different timescales as demonstrated here by either recording the opening and closing of an optical Kerr gate in the ps regime or the dynamics of laser-induced shock waves in the ns regime.

(iii) The setup can be simplified even more by removing the lenses and efficiently using digital in-line holography (DIH) to reconstruct the object on a wide depth of field. In addition, we confirmed here that the axial phase profile of the reconstructed images is a striking signature of the object position on the longitudinal axis.

Extra refinements could now be added at different levels on the technique (shaping stage, sequence depth, detector) in order to provide a fully-integrated alignment-free system for real-world applications requiring Tfps imaging without using any advanced computational imaging method. Regarding the applications, the parametric study we performed on laser-induced plasma dynamics opens the way for the routine use of our system on LIBS experiments in order to better feed the current expansion models [168]. The latter are indeed incomplete as they are based on the data collected using experimental methods with temporal resolution in the range of 100 ns (Schlieren photography, shadowgraphy). Beyond the field of plasma physics, the technique could now be used to track many non-repetitive ultrafast dynamics such as those occurring in cavitation, liquid ligaments, two phase flows, electrical breakdown, or even in ultrafast nano-tip bursting in atom probe tomography. These particular applications are currently studied as actual perspectives to this PhD thesis.

CHAPTER 6

Conclusion

THE MAIN scope of this thesis was the development of single-shot measurement tools for tracking ultrafast phenomena. The underlying goal was to highlight the dynamics in laser oscillators, in the optical Kerr effect as well as light-matter interactions. These distinct phenomena required the design and implementation of different measurement tools tailored to extract information inaccessible using conventional methods. For this reason, this PhD thesis' work has been approached from different but complementary angles. We first introduced fiber optic parametric oscillators, their design and implementation for the purpose of generating high-energy tunable pulses, and then explored the ultrafast dynamics of such systems through DFT-based single-shot spectral measurements. Afterwards, the focus was shifted to the study of the Kerr effect resulting from the propagation of intense light pulses through a highly nonlinear material. An original single-shot Tfps optical imaging system has then been designed and implemented based on the sequentially timed all optical mapping photography technique, and then improved through the incorporation of digital in-line holography as well as acousto-optic programmable dispersive filtering. The implemented system has later been modified to adapt to the temporal and spatial resolutions required to capture the ultrafast dynamics resulting from the interaction of matter with light (laser ablation and laser induced air-breakdown). The single-shot feature of the implemented systems provides a powerful solution for capturing transient dynamics and rare events. In addition, their resolutions offer precise measurements for an accurate description of the evolution of the physical phenomena. In the following, we recall and highlight the key results and features demonstrated throughout this manuscript.

In the **second chapter**, we were mainly interested in the design and implementation of a fiber optical parametric chirped pulse oscillator pumped in the normal dispersion regime, which is an efficient FWM-based device for wavelength conversion. The implemented system exploits a PCF

as a gain medium to create a seed signal due to the parametric gain. Afterwards, the gain medium amplifies the created seed after synchronization and spectral filtering using the time-dispersion tuning technique. Our system offers tunable signal and idler wavelengths over a significant band of frequencies, from 870 nm to 905 nm for the signal and from 1210 to 1270 nm for the idler. The pumping of the implemented system with chirped pump pulses results in the generation of signal and idler pulses with energies as high as 50 nJ and 250 nJ, respectively. Moreover, the stretching of the pump has an apparent influence on the spectro-temporal characteristics of the generated signal and idler. For instance, the generated idler has a spectral width superior to that of the pump whilst the signal has an inferior spectral width. In addition, numerical simulations show that the chirp of the pump is transferred to the idler and signal through the parametric amplification process. At last, we numerically investigated the dynamics that could emerge in the parametric generation process as well the potential of pushing the idler pulse energy beyond the microJoule barrier through increasing the pump energy and chirp. In the latter, the obtained results show great promise as using 10 µJ / 700 ps chirped pump pulses could indeed lead to the generation of µJ-level idler pulses.

In the **third chapter**, the main goal was to extend our understanding of the parametric generation and amplification processes in fiber optic parametric oscillators. For this purpose, we took advantage of the DFT capacity of performing real-time single-shot spectral measurements to record large sets of single-shot spectra at the input and output of a synchronously pumped normal dispersion picosecond FOPO system. The recorded spectra served as a dataset for statistical analysis on which a combination of statistical tools - including mutual information analysis- were used to generate spectral maps capable of tracking the transfer of energy from pump to signal and idler, and thereby characterize the efficiency of the parametric energy conversion on a single wavelength basis. This approach proved to be efficient for unveiling specific transient and steady state dynamics of the FOPO. For instance, it allowed for the investigation of the pump induced noise and its relation to the spectral characteristics of the pump. Moreover, it allowed to visualize the tuning effect on the generated spectral maps and showed the potential for shaping spectral correlations through the manipulation of the phase matching conditions. These features strengthen our belief regarding the generalization of the proposed approach to be routinely used for the investigation and exploration of the dynamics of other optical systems.

In the **fourth chapter**, we shifted our focus from the study of the dynamics of laser oscillators to those of ultrafast light-induced phenomena, namely the Kerr effect, laser ablation and laser induced air breakdown. This chapter is almost self-sufficient as it includes the theoretical background of multiple fundamental concepts like digital in-line holography (DIH) as well as the acousto-optic effect in birefringent acousto-optic crystals. Along the chapter, our imaging system was detailed in a progressive manner by exposing its limitations and then proposing solutions to overcome them. At the end, we successfully improved the characteristics of the imaging system within the limits set by the SF-STAMP technique as it was then capable of taking five single-shot images featuring an

almost even time between frames and uniform illumination conditions by leveraging the AOPDF's pulse shaping capabilities. In the picosecond time scale, we reached an average exposure time of 700 fs while the time between frames was set to 2 ps between the first two frames and 1.33 ps between the rest. The temporal characteristics of our imaging system allowed for the experimental observation of the Kerr effect induced by a single pump pulse in an optical Kerr gate. This effect was numerically simulated and the theoretical model validated our experimental results. In the nanosecond time scale, the system was modified for the adaptation of its field of view as well as its temporal observation window to the phenomena under study. The latter was performed through imposing a group delay on different spectral components of the imaging pulse using a modified single grating compressor device. We successfully extended the observation window to 10 ns with a constant time between frames of 2.5 ns and an estimated exposure time of $\sim$2 ps. On the one hand, this system allowed for capturing the laser-induced gas-dynamics occurring due to laser ablation. In this context, we performed several parametric studies to study the impact of the pump energy, focusing conditions as well as the target material on the gas-dynamics. On the other hand, we could successfully capture the birth and evolution of the laser-induced air breakdown phenomenon with the aid of digital in-line holography. The latter does not only simplify the imaging system through the removal of all optical lenses, it also gives access to information about the object in longitudinal axis as it provides precise measurement of the objects position with respect to the image sensor. As a conclusion, we can say that our system represents a simple, flexible and user-friendly variant of burst imaging systems that can serve the research interests in several fields, especially within the CORIA's research activities.

Annexes

APPENDIX A

Theoretical model for the optical Kerr gate

In the simulation of the CS_2-based OKG, we considered the change of the refractive index in time and space due to the pump intensity as follows [160]:

$$\Delta n(\mathbf{r},t) = n_2 \frac{\tau_0+\tau_r}{\tau_0^2}\int_{-\infty}^{t} I_p(\mathbf{r},\tau) exp\left[-\frac{t-\tau}{\tau_0}\right]\left[1-exp\left[-\frac{t-\tau}{\tau_r}\right]\right]d\tau \tag{A.1}$$

with $t \geq 0$, where τ_0 is the rise time ($\tau_0 = 0.14$ ps), τ_r the relaxation time ($\tau_r = 1.0$ ps), n_2 the nonlinear refractive index of CS_2 ($n_2 = 3.0 \times 10^{-19} m^2/W$) [160] and $I_p(\mathbf{r},\tau)$ the intensity of the pump in time and space. The pump beam is given an elliptical spatial profile and a Gaussian temporal shape corresponding to an intensity distribution given by:

$$I_p(\mathbf{r},t) = I_{pmax} exp\left[-\frac{x^2}{x_p^2}-\frac{y^2}{y_p^2}-\left(\frac{t}{\tau_p}\right)^2\right] \tag{A.2}$$

with x_2 = 3.8 mm (corresponding to a FWHM = 5.3 mm), y_2 = 1.4 mm, $\tau_p = 60 fs$ (FWHM = 100 fs). The energy per pulse is E = 0.4 mJ and I_{pmax} (in W/m^2) is the maximum intensity of the pump. The image is composed of 5 pulses delayed in time, which all have the same Gaussian shape, in space and time. Nevertheless, as there is no overlap between the pulses on the detector, only one pulse propagation is simulated, and is delayed by a time τ_d to mimic the other pulses. The probe pulse is thus written as:

$$I_{im}(\mathbf{r},t) = I_{immax} exp\left[-\frac{x^2+y^2}{r_{im}^2}-\left(\frac{t-t_d}{\tau_{im}}\right)^2\right] \tag{A.3}$$

where r_{im} = 1.0 mm (FWHM = 1.6 mm), $\tau_{im} = 0.41$ ps (FWHM = 0.723 ps), $\tau_d = 0.0, 2.0, 3.3, 4.7, 6.0$ ps and I_{immax} is the maximum intensity of the image pulses. The CS_2 cell is rectangular and much larger than the overlap zone of pump and probe pulses. The length of the cell in the image beam propagation direction z is 10 mm. The angle between the two beams is $\Theta = 42^\circ$ in air, corresponding to 26° inside the cell according to the Snell-Descartes laws. The pump beam induces a birefringence at an angle of 45° relatively to the *x* and *y* axes. The phase change of the image pulse along a propagation distance δz, where image and pump pulses overlap, is given by:

$$\delta\varphi = \frac{2\pi\delta z}{\lambda}\Delta n \tag{A.4}$$

For each time interval, the overlap between the image and pump pulses is computed and the phase change $\delta\varphi$ is deduced. The overall transmitted intensity is finally given by Eq. A.5, where φ is the accumulation of all $\delta\varphi$.

$$I = sin^2\frac{\varphi}{2} \tag{A.5}$$

Publications in international peer-reviewed journals

- R. Becheker, M. Tang, M. Touil, T. Robin, B. Cadier, M. Laroche, T. Godin, and A. Hideur, "*Dissipative soliton resonance in a mode-locked Nd-fiber laser operating at 927 nm*", Opt. Lett. 44, 5497 (2019). https://doi.org/10.1364/OL.44.005497
- R. Becheker, M. Touil, S. Idlahcen, M. Tang, A. Haboucha, B. Barviau, F. Grisch, P. Camy, T. Godin, and A. Hideur, "*High-energy normal-dispersion fiber optical parametric chirped-pulse oscillator*", Opt. Lett. 45, 6398 (2020). https://doi.org/10.1364/OL.408367
- M. Touil, R. Becheker, T. Godin, and A. Hideur, "*Spectral correlations in a fiber-optical parametric oscillator*", Phys. Rev. A 103, 043503 (2021). https://doi.org/10.1103/PhysRevA.103.043503
- M. Touil, S. Idlahcen, R. Becheker, D. Lebrun, C. Rozé, A. Hideur, and T. Godin, "*Acousto-optically driven single-shot ultrafast optical imaging*", ArXiv 2110.07013. https://arxiv.org/abs/2110.07013 - submitted to Light Sci. Appl. (2021)

Communications in conferences : oral contributions

- **[Invited]** R. Becheker, M. Touil, S. Idlahcen, M. Tang, A. Haboucha, B. Barviau, F. Grisch, P. Camy, T. Godin, and A. Hideur, "*Experimental demonstration of fiber optical parametric chirped pulse oscillation at 1 μm*", OSA Advanced Photonics Congress, Nonlinear Photonics, Juillet 2020.
- R. Becheker, M. Touil, S. Idlahcen, M. Tang, A. Haboucha, B. Barviau, F. Grisch, P. Camy, T. Godin, and A. Hideur, "*Fiber optical parametric chirped-pulse oscillator at 1220 nm*", 9th EPS-QEOD Europhoton Conference, Septembre 2020.
- M. Touil, R. Becheker, T. Godin, and A. Hideur, "*Spectro-temporal dynamics in a fiber optical parametric oscillator*", 9th EPS-QEOD Europhoton Conference, Septembre 2020.
- R. Becheker, M. Touil, S. Idlahcen, M. Tang, A. Haboucha, B. Barviau, F. Grisch, P. Camy, T. Godin, and A. Hideur, "*High-energy fiber optical parametric chirped-pulse oscillator*", CLEO/EUROPE-EQEC 2021, Munich, Juin 2021.

Communications in conferences : poster contributions

- R. Becheker, M. Touil, K. Le Corre, T. Robin, B. Cadier, M. Laroche, T. Godin, and A. Hideur, "*Observation of dissipative soliton resonance mode-locking in an all-polarization-maintaining neodymium fiber laser*", OSA Laser Congress - Advanced Solid State Lasers (ASSL), Vienna, October 2019.
- M. Touil, R. Becheker, T. Godin, and A. Hideur, "*Wavelength correlations in a fiber optical parametric oscillator*", CLEO/EUROPE-EQEC 2021, Munich, Juin 2021.
- M. Touil, R. Becheker, T. Godin, and A. Hideur, "*Démonstration d'une technique d'imagerie ultra-rapide single-shot controlable à 1 Tfps*", Optique Dijon, Juillet 2021.

Communications in GdR ELIOS - https://www.gdr-elios.cnrs.fr/

- R. Becheker, M. Touil, S. Idlahcen, M. Tang, A. Haboucha, B. Barviau, F. Grisch, P. Camy, T. Godin, and A. Hideur, "*Experimental and numerical demonstration of fiber optical parametric chirped-pulse oscillator at 1220 nm*", 1ère réunion plénière du GdR ELIOS, 3 décembre 2020.
- M. Touil, R. Becheker, T. Godin, and A. Hideur, "*Investigation of the spectro-temporal dynamics in a fiber optical parametric oscillator*", 1ère réunion plénière du GdR ELIOS, 3 décembre 2020.
- M. Touil, S. Idlahcen, R. Becheker, D. Lebrun, C. Rozé, A. Hideur, and T. Godin, "*Flexible ultrafast burst imaging*", Journées du GdR ELIOS, 19-20 octobre 2021, Lille.

Bibliography

[1] John M. Dudley. Light, Lasers, and the Nobel Prize. *Advanced Photonics*, 2(5):1 – 3, 2020.

[2] International Year of Light. https://www.light2015.org/Home.html.

[3] International Day of Light. https://en.unesco.org/commemorations/dayoflight.

[4] Jim Al-Khalili. In retrospect: Book of optics. *Nature*, 518:164–165, 2015.

[5] Coria's website. https://www.coria.fr/.

[6] G. Agrawal. *Nonlinear Fiber Optics*. Academic Press, 5^{th} edition edition, 2013.

[7] R. W. Boyd. *Nonlinear Optics*. Academic Press, 4^{th} edition edition, 2020.

[8] Satish Addanki, I.S. Amiri, and P. Yupapin. Review of optical fibers-introduction and applications in fiber lasers. *Results in Physics*, 10:743–750, 2018.

[9] R.J. Mears, L. Reekie, I.M. Jauncey, and D.N. Payne. Low-noise erbium-doped fibre amplifier operating at 1.54µm. *Electronics Letters*, 23(19):1026–1028, 1987.

[10] R. Paschotta, J. Nilsson, A.C. Tropper, and D.C. Hanna. Ytterbium-doped fiber amplifiers. *IEEE Journal of Quantum Electronics*, 33(7):1049–1056, 1997.

[11] Darwin K. Serkland and Prem Kumar. Tunable fiber-optic parametric oscillator. *Opt. Lett.*, 24(2):92–94, Jan 1999.

[12] JC Knight, TA Birks, P St J Russell, and DM Atkin. All-silica single-mode optical fiber with photonic crystal cladding. *Optics letters*, 21(19):1547–1549, 1996.

[13] J. C. Knight. Photonic crystal fibres. *Nature*, 424:847–851, 2003.

[14] Philip Russell. Photonic crystal fibers. *Science*, 299(5605):358–362, 2003.

[15] Tim A Birks, Jonathan C Knight, and P St J Russell. Endlessly single-mode photonic crystal fiber. *Optics letters*, 22(13):961–963, 1997.

[16] Ryszard Buczynski. Photonic crystal fibers. *Acta Physica Polonica Series a*, 106, 08 2004.

[17] Robert W Boyd. *Nonlinear optics*. Academic press, 2020.

[18] Yuen-Ron Shen. The principles of nonlinear optics. *New York*, 1984.

[19] John M. Dudley, Goëry Genty, and Stéphane Coen. Supercontinuum generation in photonic crystal fiber. *Rev. Mod. Phys.*, 78:1135–1184, Oct 2006.

[20] J. G. Rarity, J. Fulconis, J. Duligall, W. J. Wadsworth, and P. St. J. Russell. Photonic crystal fiber source of correlated photon pairs. *Opt. Express*, 13(2):534–544, Jan 2005.

[21] Stéphane Coen, Marc Haelterman, Ph Emplit, Laurent Delage, Lotfy Mokhtar Simohamed, and François Reynaud. Experimental investigation of the dynamics of a stabilized nonlinear fiber ring resonator. *JOSA B*, 15(8):2283–2293, 1998.

[22] Kyozo Tsujikawa, Katsusuke Tajima, and Jian Zhou. Intrinsic loss of optical fibers. *Optical Fiber Technology*, 11(4):319–331, 2005.

[23] Rudiger Paschotta. *Field guide to optical fiber technology Rudiger Paschotta.* SPIE field guides ; FG16. SPIE Press, Bellingham, Wash., 2010.

[24] Léon Brillouin. *Wave propagation and group velocity*, volume 8. Academic press, 2013.

[25] Paul Diament. *Wave transmission and fiber optics*. Macmillan, 1990.

[26] Vladimir E Zakharov and Lev A Ostrovsky. Modulation instability: the beginning. *Physica D: Nonlinear Phenomena*, 238(5):540–548, 2009.

[27] K Mynbaev Djafar and L Scheiner Lowell. Fiber-optic communications technology, 2002.

[28] D Nodop, C Jauregui, D Schimpf, J Limpert, and A Tünnermann. Efficient high-power generation of visible and mid-infrared light by degenerate four-wave-mixing in a large-mode-area photonic-crystal fiber. *Optics letters*, 34(22):3499–3501, 2009.

[29] Alexander M Heidt. Pulse preserving flat-top supercontinuum generation in all-normal dispersion photonic crystal fibers. *JOSA B*, 27(3):550–559, 2010.

[30] Per Olof Hedekvist, Magnus Karlsson, and Peter A Andrekson. Fiber four-wave mixing demultiplexing with inherent parametric amplification. *Journal of lightwave technology*, 15(11):2051–2058, 1997.

[31] E. A. Golovchenko and A. N. Pilipetskii. Unified analysis of four-photon mixing, modulational instability, and stimulated raman scattering under various polarization conditions in fibers. *J. Opt. Soc. Am. B*, 11(1):92–101, Jan 1994.

[32] Thibaut Sylvestre, Hervé Maillotte, Eric Lantz, and Fabrice Devaux. Pump-power-dependent gain for small-signal parametric amplification in birefringent fibres. *Opt. Commun.*, 191:245–251, 2001.

[33] Min Won Lee, Thibaut Sylvestre, Michaël Delque, Alexandre Kudlinski, Arnaud Mussot, J.-F. Gleyze, Alain Jolly, and Hervé Maillotte. Demonstration of an all-fiber broadband optical parametric amplifier at 1 µm. *Journal of Lightwave Technology*, 28(15):2173–2178, 2010.

[34] JP Pocholle, J Raffy, M Papuchon, and E Desurvire. Raman and four photon mixing amplification in single mode fibers. *Optical engineering*, 24(4):244600, 1985.

[35] Karsten Rottwitt, Jorn Hedegaard Povlsen, and Andros Bjarklev. Long distance transmission through distributed erbium-doped fibers. *Journal of lightwave technology*, 11(12):2105–2115, 1993.

[36] Hiro Suzuki, J-I Kani, Hiroji Masuda, Noboru Takachio, Katsumi Iwatsuki, Yasuhiko Tada, and Masatoyo Sumida. 1-tb/s (100 x 10 gb/s) super-dense wdm transmission with 25-ghz channel spacing in the zero-dispersion region employing distributed raman amplification technology. *IEEE Photonics Technology Letters*, 12(7):903–905, 2000.

[37] Michel E. Marhic. *Fiber Optical Parametric Amplifiers, Oscillators and Related Devices*. Cambridge University Press, 2007.

[38] Roger H Stolen, James P Gordon, WJ Tomlinson, and Hermann A Haus. Raman response function of silica-core fibers. *JOSA B*, 6(6):1159–1166, 1989.

[39] Mihaela Balu, Tommaso Baldacchini, John L Carter, Tatiana B Krasieva, Ruben Zadoyan, and Bruce Jason Tromberg. Effect of excitation wavelength on penetration depth in nonlinear optical microscopy of turbid media. *J. Biomed. Opt.*, 14(1):010508, 2009.

[40] C Xu and FW Wise. Recent advances in fibre lasers for nonlinear microscopy. *Nat. Photon.*, 7(11):875, 2013.

[41] Erin S Lamb, Simon Lefrancois, Minbiao Ji, William J Wadsworth, X Sunney Xie, and Frank W Wise. Fiber optical parametric oscillator for coherent anti-stokes Raman scattering microscopy. *Opt. Lett.*, 38(20):4154–4157, 2013.

[42] Thomas Gottschall, Tobias Meyer, Martin Baumgartl, Benjamin Dietzek, Jürgen Popp, Jens Limpert, and Andreas Tünnermann. Fiber-based optical parametric oscillator for high resolution coherent anti-Stokes Raman scattering (CARS) microscopy. *Opt. Express*, 22(18):21921–21928, 2014.

[43] Cihang Kong, Christian Pilger, Henning Hachmeister, Xiaoming Wei, Tom H. Cheung, Cora S. W. Lai, Nikki P. Lee, Kevin. K. Tsia, Kenneth K. Y. Wong, and Thomas Huser. High-contrast, fast chemical imaging by coherent Raman scattering using a self-synchronized two-colour fibre laser. *Light Sci. Appl.*, 9:25, 2020.

[44] M. Drobizhev, N. S. Makarov, S. E. Tillo, T. E. Hughes, and A. Rebane. Effect of excitation wavelength on penetration depth in nonlinear optical microscopy of turbid media. *Nat. Methods*, 8:393, 2011.

[45] R.Hofer, M.Hofer, G.A.Reider, M.Cernusca, and M.H.Ober. Modelocking of a Nd-fiber laser at 920 nm. *Opt. Commun.*, 142:242–244, 1997.

[46] Regina Gumenyuk, Janne Puustinen, Alexey V. Shubin, Igor A. Bufetov, Evgueny M. Dianov, and Oleg G. Okhotnikov. 1.32 μm mode-locked bismuth-doped fiber laser operating in anomalous and normal dispersion regimes. *Opt. Lett.*, 38(20):4005–4007, Oct 2013.

[47] J. M. O. Daniel, N. Simakov, M. Tokurakawa, M. Ibsen, and W. A. Clarkson. Ultra-short wavelength operation of a thulium fibre laser in the 1660-1750 nm wavelength band. *Opt. Express*, 23(14):18269–18276, Jul 2015.

[48] Teppo Noronen, Oleg Okhotnikov, and Regina Gumenyuk. Electronically tunable thulium-holmium mode-locked fiber laser for the 1700-1800 nm wavelength band. *Opt. Express*, 24(13):14703–14708, Jun 2016.

[49] T. Noronen, S. Firstov, E. Dianov, and Oleg Okhotnikov. 1700 nm dispersion managed mode-locked bismuth fiber laser. *Sci. Rep.*, 6:24876, 2016.

[50] F. M. Mitschke and L. F. Mollenauer. Discovery of the soliton self-frequency shift. *Opt. Lett.*, 11(10):659–661, Oct 1986.

[51] N. G. Horton, K. Wang, D. Kobat, C. G. Clark, F. W. Wise, C. B. Schaffer, and C. Xu. In vivo three-photon microscopy of subcortical structures within an intact mouse brain. *Nat. Photon.*, 7:205–209, 2013.

[52] H. Delahaye, G. Granger, D. Gaponov, L. Lavoute, S. Aleshkina, M. Salganskii, A. Hideur, M. Likhachev, and S. Février. Megawatt solitons generated above 2000 nm in bragg fibers. *Opt. Lett.*, 44(11):2713–2715, Jun 2019.

[53] Alexander M. Heidt, Jan Rothhardt, Alexander Hartung, Hartmut Bartelt, Erich G. Rohwer, Jens Limpert, and Andreas Tünnermann. High quality sub-two cycle pulses from compression of supercontinuum generated in all-normal dispersion photonic crystal fiber. *Opt. Express*, 19(15):13873–13879, Jul 2011.

[54] Wei Liu, Chen Li, Zhigang Zhang, Franz X Kärtner, and Guoqing Chang. Self-phase modulation enabled, wavelength-tunable ultrafast fiber laser sources: an energy scalable approach. *Opt. Express*, 24(14):15328–15340, 2016.

[55] Hsiang-Yu Chung, Wei Liu, Qian Cao, Franz X Kärtner, and Guoqing Chang. Er-fiber laser enabled, energy scalable femtosecond source tunable from 1.3 to 1.7 μm. *Opt. Express*, 25(14):15760–15771, 2017.

[56] L. Rishøj, B. Tai, P. Kristensen, and S. Ramachandran. Soliton self-mode conversion: revisiting Raman scattering of ultrashort pulses. *Optica*, 6(3):304–308, Mar 2019.

[57] Khmaies Guesmi, Lamiae Abdeladim, Samuel Tozer, Pierre Mahou, Takuma Kumamoto, Karolis Jurkus, Philippe Rigaud, Karine Loulier, Nicolas Dray, Patrick Georges, et al. Dual-color deep-tissue three-photon microscopy with a multiband infrared laser. *Light Sci. Appl.*, 7(1):1–9, 2018.

[58] S. Pitois and G. Millot. Experimental observation of a new modulational instability spectral window induced by fourth-order dispersion in a normally dispersive single-mode optical fiber. *Opt. Commun.*, 226:415–422, 2003.

[59] Marc Hanna, Frédéric Druon, and Patrick Georges. Fiber optical parametric chirped-pulse amplification in the femtosecond regime. *Opt. Express*, 14(7):2783–2790, 2006.

[60] Damien Bigourd, Laure Lago, Arnaud Mussot, Alexandre Kudlinski, Jean-François Gleyze, and Emmanuel Hugonnot. High-gain fiber, optical-parametric, chirped-pulse amplification of femtosecond pulses at 1 μm. *Opt. Lett.*, 35(20):3480–3482, Oct 2010.

[61] Y. Zhou, Q. Li, K. K. Y. Cheung, S. Yang, P. C. Chui, and K. K. Y. Wong. All-fiber-based ultrashort pulse generation and chirped pulse amplification through parametric processes. *IEEE Photon. Technol. Lett.*, 22:1330–1332, 2010.

[62] Damien Bigourd, Patrick Beaure d'Augerès, Jérôme Dubertrand, Emmanuel Hugonnot, and Arnaud Mussot. Ultra-broadband fiber optical parametric amplifier pumped by chirped pulses. *Opt. Lett.*, 39(13):3782–3785, Jul 2014.

[63] Valentina Cristofori, Zohreh Lali-Dastjerdi, Lars Søgaard Rishøj, Michael Galili, Christophe Peucheret, and Karsten Rottwitt. Dynamic characterization and amplification of sub-picosecond pulses in fiber optical parametric chirped pulse amplifiers. *Opt. Express*, 21(22):26044–26051, 2013.

[64] Philippe Morin, Jerome Dubertrand, Patrick Beaure d'Augeres, Yves Quiquempois, Geraud Bouwmans, Arnaud Mussot, and Emmanuel Hugonnot. μj-level raman-assisted fiber optical parametric chirped-pulse amplification. *Opt. Lett.*, 43(19):4683–4686, Oct 2018.

[65] Walter Fu and Frank W Wise. Normal-dispersion fiber optical parametric chirped-pulse amplification. *Opt. Lett.*, 43(21):5331–5334, 2018.

[66] Yukun Qin, Yi-Hsin Ou, Benjamin Cromey, Orkhongua Batjargal, Jennifer K Barton, and Khanh Kieu. Watt-level all-fiber optical parametric chirped-pulse amplifier working at 1300 nm. *Opt. Lett.*, 44(14):3422–3425, 2019.

[67] Yukun Qin, Orkhongua Batjargal, Benjamin Cromey, and Khanh Kieu. All-fiber high-power 1700 nm femtosecond laser based on optical parametric chirped-pulse amplification. *Opt. Express*, 28(2):2317–2325, Jan 2020.

[68] Walter Fu, Robert Herda, and Frank W. Wise. Design guidelines for normal-dispersion fiber optical parametric chirped-pulse amplifiers. *J. Opt. Soc. Am. B*, 37(6):1790–1805, Jun 2020.

[69] T. N. Nguyen, K. Kieu, A. V. Maslov, M. Miyawaki, and N. Peyghambarian. Normal dispersion femtosecond fiber optical parametric oscillator. *Opt. Lett.*, 38:3616–3619, 2013.

[70] R. Becheker, M. Tang, P.-H. Hanzard, A. Tyazhev, A. Mussot, A. Kudlinski, A. Kellou, J.-L. Oudar, T. Godin, and A Hideur. High-energy dissipative soliton-driven fiber optical parametric oscillator emitting at 1.7 μm. *Laser Phys. Lett.*, 15:115103, 2018.

[71] Thomas Gottschall, Tobias Meyer, Michael Schmitt, Jürgen Popp, Jens Limpert, and Andreas Tünnermann. Four-wave-mixing-based optical parametric oscillator delivering energetic, tunable, chirped femtosecond pulses for non-linear biomedical applications. *Opt. Express*, 23(18):23968–23977, Sep 2015.

[72] Thomas Gottschall, Jens Limpert, and Andreas Tünnermann. Ultra-short pulse fiber optical parametric oscillator. *Opt. Lett.*, 42(17):3423–3426, Sep 2017.

[73] Maximilian Brinkmann, Tim Hellwig, and Carsten Fallnich. Optical parametric chirped pulse oscillation. *Opt. Express*, 25(11):12884–12895, 2017.

[74] Y. Q. Xu and S. G. Murdoch. High conversion efficiency fiber optical parametric oscillator. *Opt. Lett.*, 36(21):4266–4268, Nov 2011.

[75] Maximilian Brinkmann, Tim Hellwig, and Carsten Fallnich. Optical parametric chirped pulse oscillation. *Opt. Express*, 25(11):12884–12895, 2017.

[76] Alexey Tikan, Serge Bielawski, Christophe Szwaj, Stéphane Randoux, and Pierre Suret. Single-shot measurement of phase and amplitude by using a heterodyne time-lens system and ultrafast digital time-holography. *Nat. Photon.*, 12:228–234, 2018.

[77] P. Ryczkowski, M. Närhi, C. Billet, J.-M. Merolla, G. Genty, and J. M. Dudley. Real-time full-field characterization of transient dissipative soliton dynamics in a mode-locked laser. *Nat. Photon.*, 12:221–227, 2018.

[78] Ata Mahjoubfar, Dmitry V. Churkin, Stéphane Barland, Neil Broderick, Sergei K. Turitsyn, and Bahram Jalali. Time stretch and its applications. *Nat. Photon.*, 11:341–351, 2017.

[79] K. Goda and B. Jalali. Dispersive Fourier transformation for fast continuous single-shot measurements. *Nat. Photon.*, 7:102–112, 2013.

[80] G. Herink, B. Jalali, C. Ropers, and D. R. Solli. Resolving the build-up of femtosecond mode-locking with single-shot spectroscopy at 90 MHz frame rate. *Nat. Photon.*, 10:321–326, 2016.

[81] G. Herink, F. Kurtz, B. Jalali, D. R. Solli, and C. Ropers. Real-time spectral interferometry probes the internal dynamics of femtosecond soliton molecules. *Science*, 356:50–54, 2017.

[82] Katarzyna Krupa, K. Nithyanandan, Ugo Andral, Patrice Tchofo-Dinda, and Philippe Grelu. Real-time observation of internal motion within ultrafast dissipative optical soliton molecules. *Phys. Rev. Lett.*, 118:243901, 2017.

[83] B. Wetzel, A. Stefani, L. Larger, P. A. Lacourt, J. M. Merolla, T. Sylvestre, A. Kudlinski, A. Mussot, G. Genty, F. Dias, and J. M. Dudley. Real-time full bandwidth measurement of spectral noise in supercontinuum generation. *Sci. Rep.*, 2:882, 2012.

[84] T. Godin, B. Wetzel, T. Sylvestre, L. Larger, A. Kudlinski, A. Mussot, A. Ben Salem, M. Zghal, G. Genty, F. Dias, and J. M. Dudley. Real time noise and wavelength correlations in octave-spanning supercontinuum generation. *Opt. Express*, 21:18452–18460, 2013.

[85] D. R. Solli, G. Herink, B. Jalali, and C. Ropers. Fluctuations and correlations in modulation instability. *Nat. Photon.*, 6:463–468, 2012.

[86] Xie Wang, Damien Bigourd, Alexandre Kudlinski, Kenneth K. Y. Wong, Marc Douay, Laurent Bigot, Antoine Lerouge, Yves Quiquempois, and Arnaud Mussot. Correlation between multiple modulation instability side lobes in dispersion oscillating fiber. *Opt. Lett.*, 39:1881–1884, 2014.

[87] Srikanth Sugavanam, Mariia Sorokina, and Dmitry V. Churkin. Spectral correlations in a random distributed feedback fibre laser. *Nat. Commun.*, 8:15514, 2017.

[88] Paul Robert, Coralie Fourcade-Dutin, Romain Dauliat, Raphael Jamier, Hector Muñoz-Marco, Pere Pérez-Millán, John M. Dudley, Philippe Roy, Hervé Maillotte, and Damien Bigourd. Spectral correlation of four-wave mixing generated in a photonic crystal fiber pumped by a chirped pulse. *Opt. Lett.*, 45(15):4148–4151, Aug 2020.

[89] M Barbier, I Zaquine, and P Delaye. Spontaneous four-wave mixing in liquid-core fibers: towards fibered Raman-free correlated photon sources. *New Journal of Physics*, 17(5):053031, may 2015.

[90] M. A. Finger, N. Y. Joly, P. St. J. Russell, and M. V. Chekhova. Characterization and shaping of the time-frequency Schmidt mode spectrum of bright twin beams generated in gas-filled hollow-core photonic crystal fibers. *Phys. Rev. A*, 95:053814, 2017.

[91] M. Cordier, A. Orieux, B. Debord, F. Gérome, A. Gorse, M. Chafer, E. Diamanti, P. Delaye, F. Benabid, and I. Zaquine. Active engineering of four-wave mixing spectral correlations in multiband hollow-core fibers. *Opt. Express*, 27:9803–9814, 2019.

[92] Jonathan Roslund, Renné Medeiros de Araújo, Shifeng Jiang, Claude Fabre, and Nicolas Treps. Wavelength-multiplexed quantum networks with ultrafast frequency combs. *Nat. Photon.*, 8:109–112, 2014.

[93] Julien Laurat, Laurent Longchambon, Claude Fabre, and Thomas Coudreau. Experimental investigation of amplitude and phase quantum correlations in a type ii optical parametric oscillator above threshold: from nondegenerate to degenerate operation. *Opt. Lett.*, 30(10):1177–1179, May 2005.

[94] D. Descloux, C. Laporte, J.-B. Dherbecourt, J.-M. Melkonian, M. Raybaut, C. Drag, and A. Godard. Spectrotemporal dynamics of a picosecond OPO based on chirped quasi-phase-matching. *Opt. Lett.*, 40:280–283, 2015.

[95] Karolina Ivanauskienė, Ignas Stasevičius, Mikas Vengris, and Valdas Sirutkaitis. Pulse-to-pulse instabilities in synchronously pumped femtosecond optical parametric oscillator. *J. Opt. Soc. Am. B*, 36:131–139, 2019.

[96] Gian-Luca Oppo, Alison M. Yao, and Domenico Cuo. Self-organization, pattern formation, cavity solitons, and rogue waves in singly resonant optical parametric oscillators. *Phys. Rev. A*, 88:043813, 2013.

[97] Thomas Gottschall, Tobias Meyer, Michael Schmitt, Jürgen Popp, Jens Limpert, and Andreas Tünnermann. Four-wave-mixing-based optical parametric oscillator delivering energetic, tunable, chirped femtosecond pulses for non-linear biomedical applications. *Opt. Express*, 23:23968–23977, 2015.

[98] C. Xu and F. W. Wise. Recent advances in fibre lasers for nonlinear microscopy. *Nat. Photon.*, 7:875, 2013.

[99] Erin S. Lamb, Simon Lefrancois, Minbiao Ji, William J. Wadsworth, X. Sunney Xie, and Frank W. Wise. Fiber optical parametric oscillator for coherent anti-Stokes Raman scattering microscopy. *Opt. Lett.*, 38:4154–4157, 2013.

[100] X. Chen, S. Yang, S. Ding, M. Chen, and H. Chen. Instantaneous dynamics of a fiber optical parametric oscillator within its initiating process. *IEEE Photonics Technology Letters*, 31(13):1088–1091, 2019.

[101] M. C. Soriano, L. Zunino, O. A. Rosso, I. Fischer, and C. R. Mirasso. Spectral correlations in a random distributed feedback fibre laser. *IEEE J. Quantum Electron.*, 47:252–261, 2011.

[102] R. Becheker, M. Tang, P.-H. Hanzard, A. Tyazhev, A. Mussot, A. Kudlinski, A. Kellou, J.-L. Oudar, T. Godin, and A. Hideur. High-energy dissipative soliton-driven fiber optical parametric oscillator emitting at 1.7 μm. *Las. Phys. Lett.*, 15:115103, 2018.

[103] M. Tang, H. Wang, R. Becheker, J.-L. Oudar, D. Gaponov, T. Godin, and A. Hideur. High-energy dissipative solitons generation from a large normal dispersion Er-fiber laser. *Opt. Lett.*, 40:1414–1417, 2015.

[104] P.Tournois. Analogie optique de la compression d'impulsion. *Acad. Sci. (Paris)*, 258:3839–3842, 1964.

[105] S. A. Chirkin S.A Akhmanov, A. P. Sukhorukov. Stationary phenomena and space-time analogy in non-linear optics. *sov. Phys*, Jetp 28:748–757, 1969.

[106] Chao Wang. Dispersive fourier transformation for versatile microwave photonics applications. *Photonics*, 1(4):586–612, 2014.

[107] Evarist Palushani, Leif Katsuo Oxenløwe, Michael Galili, Hans Christian Hansen Mulvad, Anders Clausen, and Palle Jeppesen. Flat-top pulse generation by the optical fourier transform technique for ultrahigh speed signal processing. *I E E E Journal of Quantum Electronics*, 45(11):1317–1324, 2009.

[108] Haiyun Xia, Chao Wang, Sébastien Blais, and Jianping Yao. Ultrafast and precise interrogation of fiber bragg grating sensor based on wavelength-to-time mapping incorporating higher order dispersion. *J. Lightwave Technol.*, 28(3):254–261, Feb 2010.

[109] K. Goda, K. K. Tsia, and B. Jalali. Serial time-encoded amplified imaging for real-time observation of fast dynamic phenomena. *Nature*, 458:1145–1149, 2009.

[110] Thomas M. Cover and Joy A. Thomas. *Elements of information theory*. Wiley, 2006.

[111] J. Peng, M. Sorokina, S. Sugavanam, N. Tarasov, D. V. Churkin, S. K. Turitsyn, and H. Zeng. Real-time observation of dissipative soliton formation in nonlinear polarization rotation mode-locked fibre lasers. *Commun. Phys.*, 1:20, 2018.

[112] Junhee Seok and Yeong Seon Kang. Mutual information between discrete variables with many categories using recursive adaptive partitioning. *Sci. Rep.*, 5:2045–2322, 2015.

[113] Thomas Gottschall, Jens Limpert, and Andreas Tünnermann. Ultra-short pulse fiber optical parametric oscillator. *Opt. Lett.*, 42(17):3423–3426, Sep 2017.

[114] Keisuke Nagashima, Yoshihiro Ochi, and Ryuji Itakura. Statistical effects of optical parametric noise on signal pulses in a synchronously pumped optical parametric oscillator. *J. Opt. Soc. Am. B*, 36(12):3389–3394, Dec 2019.

[115] Pierre-Henry Hanzard, Thomas Godin, Saïd Idlahcen, Claude Rozé, and Ammar Hideur. Real-time tracking of single shockwaves via amplified time-stretch imaging. *Appl. Phys. Lett.*, 112(16):161106, 2018.

[116] Pierre-Henry Hanzard. *Métrologie ultrarapide : application aux dynamiques laser et à l'imagerie*. Theses, Normandie Université, October 2018.

[117] S. X. Hu and L. A. Collins. Attosecond pump probe: Exploring ultrafast electron motion inside an atom. *Phys. Rev. Lett.*, 96:073004, Feb 2006.

[118] Eric D. Diebold, Brandon W. Buckley, Daniel R. Gossett, and Bahram Jalali. Digitally synthesized beat frequency multiplexing for sub-millisecond fluorescence microscopy. *Nature Photon.*, 7:806–810, 2013.

[119] Cheng Lei, Hirofumi Kobayashi, Yi Wu, Ming Li, Akihiro Isozaki, Atsushi Yasumoto, Hideharu Mikami, Takuro Ito, Nao Nitta, Takeaki Sugimura, Makoto Yamada, Yutaka Yatomi, Dino Di Carlo, Yasuyuki Ozeki, and Keisuke Goda. High-throughput imaging flow cytometry by optofluidic time-stretch microscopy. *Nature Protocols*, 13:1603–1631, 2018.

[120] Jie Yang, Xiaolei Zhu, Thomas J. A. Wolf, Zheng Li, J. Pedro F. Nunes, Ryan Coffee, James P. Cryan, Markus Gühr, Kareem Hegazy, Tony F. Heinz, Keith Jobe, Renkai Li, Xiaozhe Shen, Theodore Veccione, Stephen Weathersby, Kyle J. Wilkin, Charles Yoneda, Qiang Zheng, Todd J. Martinez, Martin Centurion, and Xijie Wang. Imaging cf3i conical intersection and photodissociation dynamics with ultrafast electron diffraction. *Science*, 361(6397):64–67, 2018.

[121] Hideharu Mikami, Liang Gao, and Keisuke Goda. Ultrafast optical imaging technology: principles and applications of emerging methods. *Nanophotonics*, 5(4):497–509, 2016.

[122] Jinyang Liang and Lihong V. Wang. Single-shot ultrafast optical imaging. *Optica*, 5(9):1113–1127, Sep 2018.

[123] Jinyang Liang. Punching holes in light: recent progress in single-shot coded-aperture optical imaging. *Reports on Progress in Physics*, 83(11):116101, oct 2020.

[124] Jiang-Lai Wu, Yi-Qing Xu, Jing-Jiang Xu, Xiao-Ming Wei, Antony CS Chan, Anson HL Tang, Andy KS Lau, Bob MF Chung, Ho Cheung Shum, Edmund Y Lam, Kenneth KY Wong, and Kevin K Tsia. Ultrafast laser-scanning time-stretch imaging at visible wavelengths. *Light Sci. Appl*, 6:e16196, 2017.

[125] Jinyang Liang, Cheng Ma, Liren Zhu, Yujia Chen, Liang Gao, and Lihong V. Wang. Single-shot real-time video recording of a photonic mach cone induced by a scattered light pulse. *Science Advances*, 3(1), 2017.

[126] Yunhua Yao, Yilin He, Dalong Qi, Fengyan Cao, Jiali Yao, Pengpeng Ding, Chengzhi Jin, Xianyu Wu, Lianzhong Deng, Tianqing Jia, Feng Huang, Jinyang Liang, Zhenrong Sun, and Shian Zhang. Single-shot real-time ultrafast imaging of femtosecond laser fabrication. *ACS Photonics*, 8(3):738–744, 2021.

[127] Jinyang Liang, Liren Zhu, and Lihong V. Wang. Single-shot real-time femtosecond imaging of temporal focusing. *Light Sci. Appl*, 7:42, 2018.

[128] A. Ehn, J. Bood, Z. Li, E. Berrocal, M. Aldén, and E. Kristensson. FRAME: femtosecond videography for atomic and molecular dynamics. *Light Sci. Appl*, 6:e17045, 2017.

[129] Dalong Qi, Shian Zhang, Chengshuai Yang, Yilin He, Fengyan Cao, Jiali Yao, Pengpeng Ding, Liang Gao, Tianqing Jia, Jinyang Liang, Zhenrong Sun, and Lihong V. Wang. Single-shot compressed ultrafast photography: a review. *Advanced Photonics*, 2(1):1 – 16, 2020.

[130] L. Gao, J. Y. Liang, C. Y. Li, and L. V. Wang. Single-shot compressed ultrafast photography at one hundred billion frames per second. *Nature*, 516:74–77, 2014.

[131] Yu Lu, Terence T. W. Wong, Feng Chen, and Lidai Wang. Compressed ultrafast spectral-temporal photography. *Phys. Rev. Lett.*, 122:193904, May 2019.

[132] Jinyang Liang, Peng Wang, Liren Zhu, and Lihong V. Wang. Single-shot stereo-polarimetric compressed ultrafast photography for light-speed observation of high-dimensional optical transients with picosecond resolution. *Nature Commun.*, 11:5252, 2020.

[133] Chengshuai Yang, Fengyan Cao, Dalong Qi, Yilin He, Pengpeng Ding, Jiali Yao, Tianqing Jia, Zhenrong Sun, and Shian Zhang. Hyperspectrally compressed ultrafast photography. *Phys. Rev. Lett.*, 124:023902, Jan 2020.

[134] Taewoo Kim, Jinyang Liang, Liren Zhu, and Lihong V. Wang. Picosecond-resolution phase-sensitive imaging of transparent objects in a single shot. *Science Advances*, 6(3), 2020.

[135] Peng Wang, Jinyang Liang, and Lihong V. Wang. Single-shot ultrafast imaging attaining 70 trillion frames per second. *Nature Commun.*, 11:2091, 2020.

[136] Dalong Qi, Fengyan Cao, Shuwu Xu, Yunhua Yao, Yilin He, Jiali Yao, Pengpeng Ding, Chengzhi Jin, Lianzhong Deng, Tianqing Jia, Jinyang Liang, Zhenrong Sun, and Shian Zhang. 100-trillion-frame-per-second single-shot compressed ultrafast photography via molecular alignment. *Phys. Rev. Applied*, 15:024051, Feb 2021.

[137] T. Kakue, K. Tosa, J. Yuasa, T. Tahara, Y. Awatsuji, K. Nishio, S. Ura, and T. Kubota. Digital light-in-flight recording by holography by use of a femtosecond pulsed laser. *IEEE Journal of Selected Topics in Quantum Electronics*, 18(1):479–485, 2012.

[138] Zhengyan Li, Rafal Zgadzaj, Xiaoming Wang, Yen-Yu Chang, and Michael C. Downer. Single-shot tomographic movies of evolving light-velocity objects. *Nature Commun.*, 5:3085, 2014.

[139] Qing-Yang Yue, Zhen-Jia Cheng, Lu Han, Yang Yang, and Cheng-Shan Guo. One-shot time-resolved holographic polarization microscopy for imaging laser-induced ultrafast phenomena. *Opt. Express*, 25(13):14182–14191, Jun 2017.

[140] K. Nakagawa, A. Iwasaki, Y. Oishi, R. Horisaki, A. Tsukamoto, A. Nakamura, K. Hirosawa, H. Liao, T. Ushida, K. Goda, F. Kannari, and I. Sakuma. Sequentially timed all-optical mapping photography (STAMP). *Nature Photon.*, 8:695–700, 2014.

[141] Takakazu Suzuki, Fumihiro Isa, Leo Fujii, Kenichi Hirosawa, Keiichi Nakagawa, Keisuke Goda, Ichiro Sakuma, and Fumihiko Kannari. Sequentially timed all-optical mapping photography (stamp) utilizing spectral filtering. *Opt. Express*, 23(23):30512–30522, Nov 2015.

[142] Takakazu Suzuki, Ryohei Hida, Yuki Yamaguchi, Keiichi Nakagawa, Toshiharu Saiki, and Fumihiko Kannari. Single-shot 25-frame burst imaging of ultrafast phase transition of ge2sb2te5 with a sub-picosecond resolution. *Applied Physics Express*, 10(9):092502, aug 2017.

[143] Takakazu Suzuki, Hirofumi Nemoto, Kazuki Takasawa, and Fumihiko Kannari. 1000-fps consecutive ultrafast 2d-burst imaging with a sub-nanosecond temporal resolution by a frequency-time encoding of sf-stamp. *Appl. Phys. A*, 126:135, 2020.

[144] Levent Onural. Diffraction from a wavelet point of view. *Opt. Lett.*, 18(11):846–848, Jun 1993.

[145] Cristina Buraga-Lefebvre, Sébastien Coëtmellec, Denis Lebrun, and Cafer Özkul. Application of wavelet transform to hologram analysis: three-dimensional location of particles. *Optics and Lasers in Engineering*, 33(6):409–421, 2000.

[146] Pierre Tournois. Acousto-optic programmable dispersive filter for adaptive compensation of group delay time dispersion in laser systems. *Optics Communications*, 140(4):245–249, 1997.

[147] Lorenzo Canova, Xiaowei Chen, Alexandre Trisorio, Aurélie Jullien, Andreas Assion, Gabriel Tempea, Nicolas Forget, Thomas Oksenhendler, and Rodrigo Lopez-Martens. Carrier-envelope phase stabilization and control using a transmission grating compressor and an AOPDF. *Opt. Lett.*, 34(9):1333–1335, May 2009.

[148] N. Forget, L. Canova, X. Chen, A. Jullien, and R. Lopez-Martens. Closed-loop carrier-envelope phase stabilization with an acousto-optic programmable dispersive filter. *Opt. Lett.*, 34(23):3647–3649, Dec 2009.

[149] Raman Maksimenka, Patrick Nuernberger, Kevin F. Lee, Adeline Bonvalet, Jadwiga Milkiewicz, Cestmir Barta, Miloš Klima, Thomas Oksenhendler, Pierre Tournois, Daniel Kaplan, and Manuel Joffre. Direct mid-infrared femtosecond pulse shaping with a calomel acousto-optic programmable dispersive filter. *Opt. Lett.*, 35(21):3565–3567, Nov 2010.

[150] Hélène Seiler, Brenna Walsh, Samuel Palato, Alexandre Thai, Vincent Crozatier, Nicolas Forget, and Patanjali Kambhampati. Kilohertz generation of high contrast polarization states for visible femtosecond pulses via phase-locked acousto-optic pulse shapers. *Journal of Applied Physics*, 118(10):103110, 2015.

[151] J. A. de la Paz, A. Bonvalet, and M. Joffre. Frequency-domain two-dimensional infrared spectroscopy using an acousto-optic programmable dispersive filter. *Opt. Express*, 27(4):4140–4146, Feb 2019.

[152] B. Urbanek, M. Möller, M. Eisele, S. Baierl, D. Kaplan, C. Lange, , and R. Huber. Femtosecond terahertz time-domain spectroscopy at 36 kHz scan rate using an acousto-optic delay. *Appl. Phys. Lett.*, 108:121101, 2016.

[153] Xavier Audier, Naveen Balla, and Hervé Rigneault. Pump-probe micro-spectroscopy by means of an ultra-fast acousto-optics delay line. *Opt. Lett.*, 42(2):294–297, Jan 2017.

[154] Mohammed S. Alshaykh, Chien-Sheng Liao, Oscar E. Sandoval, Gregory Gitzinger, Nicolas Forget, Daniel E. Leaird, Ji-Xin Cheng, and Andrew M. Weiner. High-speed stimulated hyperspectral Raman imaging using rapid acousto-optic delay lines. *Opt. Lett.*, 42(8):1548–1551, Apr 2017.

[155] Xavier Audier, Nicolas Forget, and Hervé Rigneault. High-speed chemical imaging of dynamic and histological samples with stimulated Raman micro-spectroscopy. *Opt. Express*, 28(10):15505–15514, May 2020.

[156] Sébastien J. Weber. *Façonnage d'impulsions femtosecondes dans l'ultraviolet. Factorisation de grands nombres. Contrôle cohérent de systèmes atomiques et moléculaires.* Theses, Université de Toulouse, July 2010.

[157] Antoine Monmayrant, Sébastien Weber, and Béatrice Chatel. A newcomer's guide to ultrashort pulse shaping and characterization. 43(10):103001, may 2010.

[158] Ming Lai, Shui T. Lai, and Casimir Swinger. Single-grating laser pulse stretcher and compressor. *Appl. Opt.*, 33(30):6985–6987, Oct 1994.

[159] P. P. Ho and R. R. Alfano. Optical kerr effect in liquids. *Phys. Rev. A*, 20:2170–2187, Nov 1979.

[160] Saïd Idlahcen, Loïc Méès, Claude Rozé, Thierry Girasole, and Jean-Bernard Blaisot. Time gate, optical layout, and wavelength effects on ballistic imaging. *J. Opt. Soc. Am. A*, 26(9):1995–2004, Sep 2009.

[161] G Callies, P Berger, and H Hugel. Time-resolved observation of gas-dynamic discontinuities arising during excimer laser ablation and their interpretation. 28(4):794–806, apr 1995.

[162] Thomas A. Schmitz, Joachim Koch, Detlef Günther, and Renato Zenobi. Early plume and shock wave dynamics in atmospheric-pressure ultraviolet-laser ablation of different matrix-assisted laser ablation matrices. *Journal of Applied Physics*, 109(12):123106, 2011.

[163] B. Pokrzywka, A. Mendys, K. Dzierżęga, M. Grabiec, and S. Pellerin. Laser light scattering in a laser-induced argon plasma: Investigations of the shock wave. *Spectrochimica Acta Part B: Atomic Spectroscopy*, 74-75:24–30, 2012. 6th Euro-Mediterranean Symposium on Laser Induced Breakdown Spectroscopy (EMSLIBS 2011).

[164] Weidong Yang, Alexander B. Kostinski, and Raymond A. Shaw. Phase signature for particle detection with digital in-line holography. *Opt. Lett.*, 31(10):1399–1401, May 2006.

[165] Bahram Javidi, Artur Carnicer, Arun Anand, George Barbastathis, Wen Chen, Pietro Ferraro, J. W. Goodman, Ryoichi Horisaki, Kedar Khare, Malgorzata Kujawinska, Rainer A. Leitgeb, Pierre Marquet, Takanori Nomura, Aydogan Ozcan, YongKeun Park, Giancarlo Pedrini, Pascal Picart, Joseph Rosen, Genaro Saavedra, Natan T. Shaked, Adrian Stern, Enrique Tajahuerce, Lei Tian, Gordon Wetzstein, and Masahiro Yamaguchi. Roadmap on digital holography. *Opt. Express*, 29(22):35078–35118, Oct 2021.

[166] Pascal Picart. *New techniques in digital holography*. John Wiley & Sons, 2015.

[167] Yi Chen Mazumdar, Michael E Smyser, Jeffery D Heyborne, Mikhail N Slipchenko, and Daniel R Guildenbecher. Megahertz-rate shock-wave distortion cancellation via phase conjugate digital in-line holography. *Nature communications*, 11(1):1–10, 2020.

[168] Vincent Morel and Arnaud Bultel. Theoretical study of the formation mechanism of laser-induced aluminum plasmas using nd:yag fundamental, second or third harmonics. *Spectrochimica Acta Part B: Atomic Spectroscopy*, 94-95:63–70, 2014.

Abstract

Real time measurements of ultrafast phenomena: applications to laser oscillators and optical metrology.

This PhD work is mainly focused on the development of efficient measurement tools for the study of the ultrafast dynamics of various physical phenomena, from those occurring within laser oscillators to laser-matter interactions. The manuscript is separated between interrelated studies dealing with laser physics, ablation dynamics and ultrafast metrology. This work is then partially devoted to the design and implementation of an efficient fiber optical parametric chirped pulse oscillator, where the well-known concept of fiber optical parametric oscillation (FOPO) is combined with the principle of chirped pulse amplification. This led to the efficient generation of high-energy, tunable, synchronized picosecond pulses in specific spectral regions. Simulations of this system has shown great potential in energy scaling and unveiled interesting dynamics. Such dynamics were then investigated using the dispersive Fourier transform technique, which enables the recording of shot-to-shot spectra and provides a large data sets for statistical analysis. This allowed for the energy tracking during the wavelength conversion process and resulted in a better comprehension of its dynamic behaviors. This work was then focused towards the development of a novel ultrafast imaging technique for studying the dynamics of several laser matter interaction processes including the optical Kerr effect, laser ablation and laser-induced air breakdown. An imaging system based on spectrally filtered sequentially timed all-optical mapping photography (SF-STAMP) together with acousto-optics filtering was developed and allowed to capture physical phenomena either in the picosecond or nanosecond time scale with a full control over the illumination conditions, exposure time and time between frames. The outcomes of this feasibility demonstration are manifold and could help to bring such ultrafast techniques out of a laboratory environment.

Keywords: Ultrafast imaging- fiber optical parametric oscillator- dispersive Fourier transform- optical Kerr gate- shockwaves- laser induced air breakdown.

Résumé

Mesures en temps réel de phénomènes ultra-rapides : applications aux oscillateurs laser et à la métrologie optique.

Ce travail de doctorat est principalement axé sur le développement d'outils de mesure efficaces dédiés à l'étude des dynamiques ultrarapides de divers phénomènes physiques, des oscillateurs laser jusqu'aux interactions laser-matière. Le manuscrit est ainsi séparé en plusieurs études connexes traitant de la physique des lasers, des dynamiques mises en jeu lors de l'ablation laser et plus généralement de la métrologie ultrarapide. Ce travail est ensuite dans un premier temps consacré à la conception et à la mise en œuvre d'un oscillateur paramétrique fibré à impulsions chirpées innovant, où le concept bien connu d'oscillateur paramétrique à fibre optique (FOPO) est combiné au principe d'amplification à dérive de fréquence. Ce nouveau concept a permis de générer efficacement des impulsions picosecondes synchronisées, accordables et à haute énergie dans des régions spectrales d'intérêt. Les simulations numériques de ce système ont démontré un fort potentiel pour la montée en énergie mais aussi dévoilé des dynamiques intéressantes. Ces dynamiques ont ensuite été étudiées à l'aide de la technique de transformée de Fourier dispersive, qui permet d'enregistrer des spectres tir-à-tir et de fournir efficacement un grand nombre de données pour l'analyse statistique. Cela a permis de suivre les transferts d'énergie pendant les processus de conversion paramétriques et de mieux comprendre leurs dynamiques. Ce travail s'est ensuite orienté vers le développement d'une nouvelle technique d'imagerie ultrarapide pour étudier les dynamiques de plusieurs processus d'interaction laser-matière, notamment l'effet Kerr optique, l'ablation laser et le claquage dans l'air induit par laser. Un système d'imagerie basé sur la technique STAMP (sequentially timed all-optical mapping photography) combinée à une étape de filtrage acousto-optique a été développé et a permis de capturer des phénomènes physiques à l'échelle de la picoseconde ou de la nanoseconde avec un contrôle total des conditions d'illumination, du temps d'exposition et du temps entre les images. Les résultats de cette démonstration de faisabilité sont ainsi multiples et pourraient permettre l'utilisation de techniques d'imagerie ultra-rapide hors d'un environnement de laboratoire.

Mots-clés: Imagerie ultrarapide - oscillateur paramétrique fibré - transformée de Fourier dispersive - porte Kerr optique - ondes de choc – interaction lumière-matière.